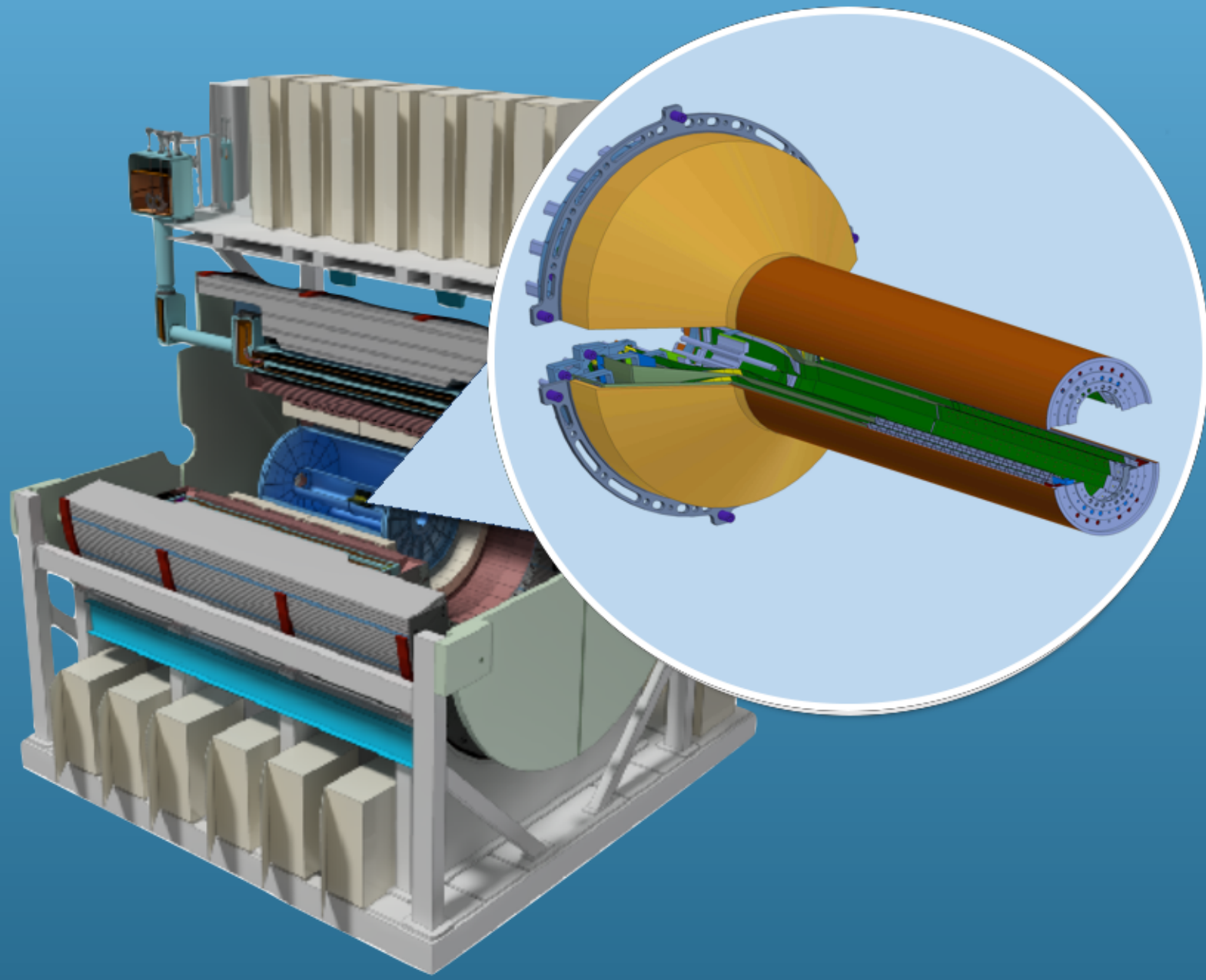

A Monolithic Active Pixel Sensor Detector for the sPHENIX Experiment

A Monolithic-Active-Pixel-Sensor-based Vertex Detector (MVTX) for the sPHENIX Experiment at RHIC

A proposal submitted to the DOE Office of Science
February 14, 2018

DOE Office of Science Program Manager: Dr. Jehanne Gillo

Proposing Organization: Los Alamos National Laboratory

Collaborating Institutions:
Brookhaven National Laboratory
Lawrence Berkeley National Laboratory
Massachusetts Institute of Technology
Univ. of California at Berkeley
Univ. of California at Los Angeles
Univ. of California at Riverside
Central China Normal University (China)
Charles University (Czech)
Univ. of Colorado
Czech Technical University (Czech)
Florida State University
Georgia State University
Iowa State University
National Central University (Taiwan)*
Univ. of New Mexico
New Mexico State University
Purdue University
Univ. of Science and Technology of China (China)
Sun Yat-Sen University (China)
Univ. of Texas at Austin
Yonsei University (Korea)
RIKEN/RBRC (Japan)

Principal Investigator: Ming X. Liu
Phone: 505-412-7396
Email: mliu@lanl.gov

Co-Investigators: Grazyna Odyniec (LBNL) and Robert Redwine (MIT)

Lead Project Coordinator: Maria Chamizo Llatas (BNL)

Requested Funding: $6.6M, FY18-FY22

*** Note:** Expressed interest to join the sPHENIX Collaboration.

Table of Contents

1 Executive Summary

The sPHENIX experiment, currently under development, is a next-generation high energy nuclear physics experiment providing world-class capabilities for multi-scale studies of the strongly coupled Quark Gluon Plasma (QGP), planned for the Relativistic Heavy Ion Collider (RHIC) at Brookhaven National Laboratory (BNL) in 2023 and beyond. It is designed to study the microscopic nature of the QGP by measuring fully reconstructed jets and high precision Upsilon spectroscopy at ultra-high beam collision rates. The need for these capabilities to advance our understanding of the origins of novel QGP properties are detailed in the 2015 NSAC Long Range Plan (LRP).

The nuclear modification and flow of heavy flavor tagged jets and heavy flavor hadrons in heavy ion collisions are key scale-dependent observables. Bottom quark jets (b-jets) and B-hadrons produced at RHIC, in comparison with the light flavor and charm quark production, offer unique capabilities for understanding the properties of the QGP by studying the mass dependence of parton energy loss in the medium and the temperature dependence of QGP transport parameters. Measuring these rare observables demands high precision and high efficiency tracking close to the interaction point with excellent displaced secondary vertex reconstruction capabilities. Given the projected RHIC luminosity and available running time, a high-speed and large acceptance precision vertex detector is highly desirable to fully explore these heavy flavor QGP signatures.

We propose to build a 50 μm thick silicon pixel vertex detector for sPHENIX. The sensor uses the latest Monolithic Active Pixel Sensor (MAPS) technology developed for the Heavy Flavor Tracker (HFT) in STAR and ALICE ITS upgrade at CERN. The proposed MAPS-based Vertex Detector (MVTX) upgrade will use the 2nd generation MAPS from ALICE to ensure that sPHENIX is capable of performing key measurements at high collision rates at mid-rapidity over a broad momentum range around the b-quark mass where mass effects are expected to play the most significant roles. The MVTX detector will provide capabilities for other heavy flavor physics studies, such as charm baryon and heavy-flavor correlation measurements at RHIC. These studies are beyond the reach of current RHIC experiments (STAR and PHENIX) and complementary to the heavy flavor program at the Large Hadron Collider (LHC). They are of central importance for achieving the science goals highlighted in the 2015 NSAC LRP - "Probe the inner workings of QGP by resolving its properties at shorter and shorter length scales."

Figures 1 and 2 show the projections for the key physics that will become accessible through the addition of the MVTX. Figure 1 shows the projected uncertainties for measurements of the nuclear modification factors of heavy flavor mesons and b-jets. Figure 2 shows the projected uncertainties for measurements of the azimuthal anisotropy, v_2, for heavy flavor mesons and b-jets. Both sets of projections show high statistical precision in the momentum ranges of interest, and once realized, will shed new light on our understanding of the novel properties of QGP.

The sPHENIX MVTX detector will provide a fast integration time ($\sim 5\ \mu s$) and very low material budget (less than 0.5% radiation length per layer) with fine pixel segmentation ($\sim 30\ \mu m$). This detector will enable a high tracking efficiency (detector hit efficiency $> 99\%$) and excellent impact parameter resolution ($< 50\ \mu m$ at $p_T = 1$ GeV/c), ideal for heavy flavor hadron identification and reconstruction at the very high beam collision rates provided by RHIC.

The Los Alamos National Laboratory (LANL) High-Energy Nuclear Physics Group has been awarded an internal LDRD grant ($5M over 3 years, FY17–19) to develop a state of the art MAPS-based telescope to demonstrate the tracking capability of such a device for the sPHENIX experiment. The LANL LDRD allows us to carry out the much needed early R&D for the MAPS readout electronics, produce the initial conceptual design of mechanical system integration into the sPHENIX detectors, and also develop the theoretical calculations, modeling and full physics simulations and analyses with a realistic detector configuration. The

LANL LDRD effort has already provided a proof of principle readout design, which will be finalized in 2018.

The main technical challenges are the development of the ALice PIxel DEtector (ALPIDE) readout systems to meet the sPHENIX data acquisition (DAQ) requirements, and the global mechanical system integration of the MVTX with the overall sPHENIX tracking systems. The design of the final MVTX readout and the conceptual mechanical systems will be completed through the LANLs LDRD effort, and this is not part of the requested project funds, but it is crucial to bring the project to a high level of maturity and to reduce the risks. The total project cost of the final design effort, procurement, assembly and installation into the sPHENIX experiment is estimated to be $6.6M. The cost includes 35% contingency and assumes production of the staves using the ALICE facility at CERN immediately following the ALICE production, which significantly reduces the cost and technical risks of the MVTX detector.

A list of the main institutions and expected contributions are summarized in Sec. 7 of this proposal. The LANL group will lead the electronics and readout effort. MIT will be leading the mechanical engineering design to fulfill the sPHENIX requirements, and the production of the support carbon structures will be performed by LBNL.

The MVTX upgrade is proposed to be ready for Day-1 sPHENIX data taking. This detector will provide world-class scientific results in key areas encompassed by the DOE Nuclear Physics mission. It will allow scientists to make fundamental inquiries into the nature of the QGP in the U.S. that cannot be probed with other existing facilities worldwide. In particular, the sPHENIX experiment, which was granted DOE CD-0 in September 2016, will complement and extend the ongoing and future QGP studies at RHIC and LHC, and will become the next generation U.S. flagship high energy nuclear physics program at the DOE's key facility in this field.

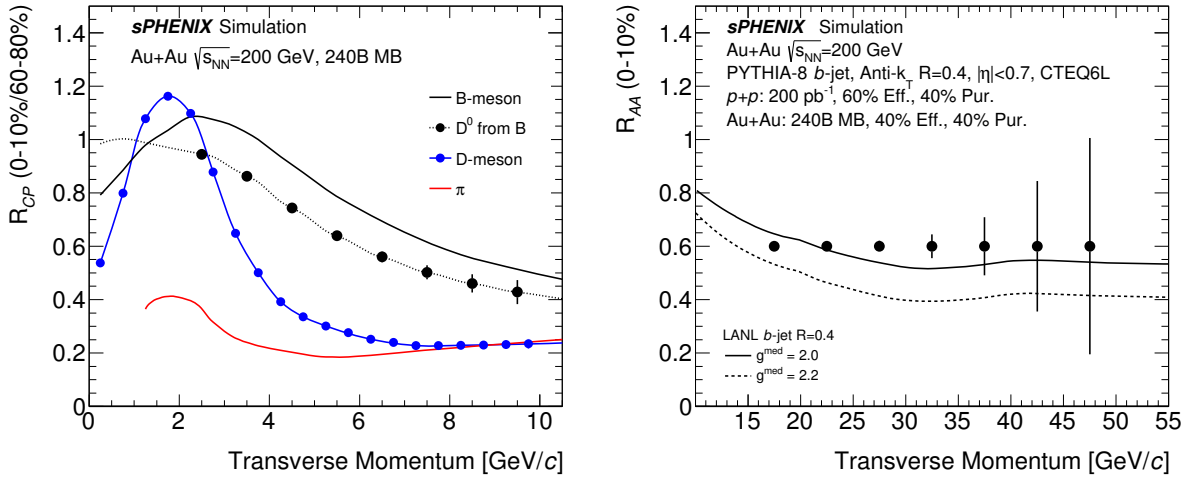

Figure 1: Projected statistical uncertainties of nuclear modification factor $R_{\rm CP}$ and $R_{\rm AA}$ measurements of non-prompt/prompt D^0 mesons (left) and b-jets (right) as a function of p_T in 0–10% central Au+Au collisions at $\sqrt{s_{NN}}$ = 200 GeV from a dataset of 240 billion minimum bias Au+Au collisions expected from the multi-year sPHENIX operation. The purity and efficiency used in these projections are based on full event simulation and reconstruction using MVTX in sPHENIX. Left: the solid blue and red lines are best fit to the RHIC data, the solid black line is from a model calculation for B mesons and the dotted line is the theory calculation for D-mesons coming from B-meson decays. Right: the solid and dashed lines are from model calculations with two different coupling parameters to the QGP medium, $g^{\rm med}$, and the statistical projection is based on the assumption of $R_{\rm AA} = 0.6$. The MVTX will enable these highest precision B-meson measurement and the first heavy flavor jet measurement at RHIC, which will place stringent tests on models describing the coupling between heavy quarks and the QGP. [1, 2, 3, 4, 5]

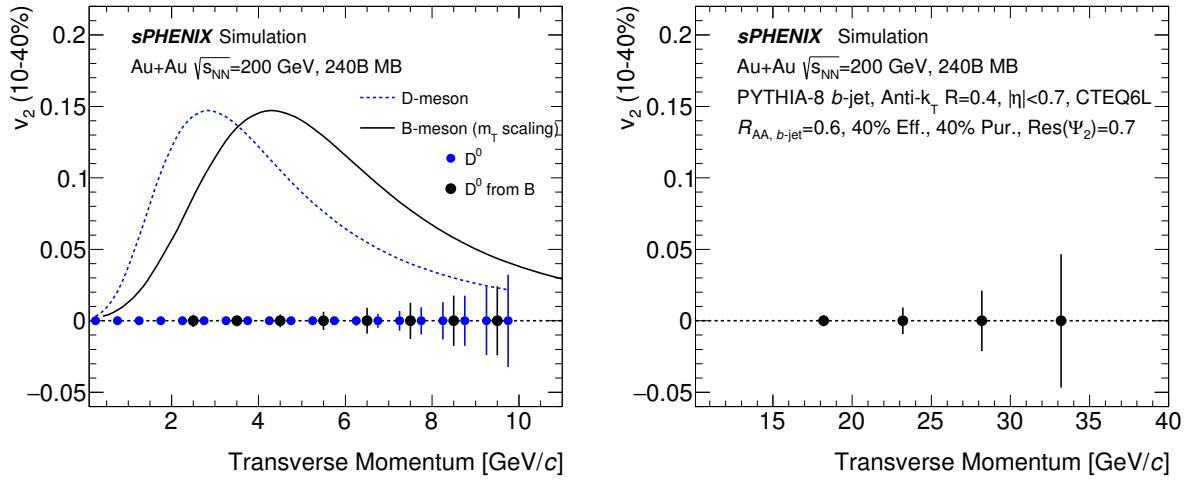

Figure 2: Projected statistical uncertainties of v_2 measurements of non-prompt/prompt D^0 mesons (left) and b-jets (right) as a function of p_T in 10–40% central Au+Au collisions at $\sqrt{s_{NN}}$ = 200 GeV from a dataset of 240 billion minimum bias Au+Au events expected from the multi-year sPHENIX operation. The purity and efficiency used in these projections are based on full event simulation and reconstruction using MVTX in sPHENIX. Left: the blue dotted line is from best fit of RHIC data, and the black line is for B-meson assuming m_T scaling in v_2. [2, 3, 4, 6]

2 Physics Motivations

2.1 Introduction

The physics goals of the proposed vertex detector project are aligned with the key challenges and physics opportunities outlined in the 2015 NSAC Long-Range Plan: "There are two central goals of measurements planned at RHIC, as it completes its scientific mission, and at the LHC: (1) Probe the inner workings of QGP by resolving its properties at shorter length scales. The complementarity of the two facilities is essential to this goal, as is a state-of-the-art jet detector at RHIC, called sPHENIX. (2) Map the phase diagram of QCD with experiments planned at RHIC."

The key approach for goal (1) is the microscopy of the QGP through probes that are sensitive to characteristic scales in the plasma. Compared with other RHIC experiments (PHENIX and STAR), the baseline sPHENIX detector is designed for high collision rate and optimized to employ light quark and gluon jets over a wide kinematic range and Υ mesons as such scale-sensitive probes. The sPHENIX will be able to collect an incredible large amount of unbiased Au+Au collision data (as ALICE Run3). The vertex detector described in this proposal will greatly expand the sPHENIX capabilities in an additional dimension related to scales in the QGP, by allowing a range of precision studies as a function of parton mass. Studies of heavy-flavor hadrons have been a focus of recent upgrades in PHENIX and STAR at RHIC. These studies, as well as new measurements by the current LHC experiments form the key motivation for the ALICE Phase-I upgrades for the early 2020's. In combination with the large acceptance and high rate capability of sPHENIX, the vertex detector upgrade provides access to observables that are not accessible with the present RHIC detectors and are complementary to those at the LHC.

Heavy flavor quarks (c, b) play a unique role in studying QCD in the vacuum as well as in the nuclear medium at finite temperature or density. Their masses are much larger than the QCD scale ($\Lambda_{\rm QCD}$), the additional QCD masses due to chiral symmetry breaking, and the typical medium temperature created at RHIC and LHC ($T \sim 300 - 500$) MeV). Therefore, they are created predominantly from initial hard scatterings and their production rates are calculable in perturbative QCD. Compared with light sector measurements, such as the jet and photon-jet measurements, the large heavy quark mass scale introduces additional experimental and theoretical handles allowing one to study quark-QGP interactions in more details and test our understanding of the underlying physics, including mass-dependent energy loss and collectivity in QGP. They thus can be used to study the QGP in a controlled manner.

The MVTX detector will enable a wide range of heavy-flavor studies, extending present RHIC measurements to significantly larger transverse momenta, providing the first precision measurements of the b-quark observables, and therefore, providing access to qualitatively new QGP signatures. A particular new capability, in combination with the sPHENIX calorimetric jet reconstruction, is the identification of jets originating from heavy quarks, in particular jets from b-quarks (b-jets). Another is to reconstruct the B-meson via its displaced decay daughter D^0 particles. Simultaneous precision measurements of B-mesons and b-jets could provide additional insights about heavy quark hadronization in heavy-ion collisions.

In this proposal, we will use the measurements of b-jets and B-mesons as case studies to illustrate the new capabilities the MVTX upgrade brings to RHIC and the overall field. Two scopes of the sPHENIX baseline detector will be assumed in these studied: (1) In Section 5 we will discuss the MVTX projection with the full scope sPHENIX baseline detectors as described in the sPHENIX scientific proposal [7], which is the detector scope that the sPHENIX scientific collaboration intends to build. (2) In Appendix B, we will also describe the projection given a possible reduced sPHENIX baseline detector scope as described in the sPHENIX Conceptual Design Report [8]. In both instances, the physics case for the MVTX physics program is highly compelling.

These measurements, as an example of the physics reach provided by the MVTX, represent both a new

opportunity at RHIC and examples of complementarity to the LHC: the projected sPHENIX measurement both extends the existing LHC measurement to lower transverse momenta and provides a kinematic overlap, where jets in similar kinematic regions can be studied in the different QGP conditions at RHIC and the LHC.

2.2 Recent achievements on heavy quark measurements at RHIC and the LHC

Significant efforts have been made over the last decade to measure the modification of heavy quark yields in the QGP medium, including recent upgrades by both PHENIX and STAR focused on measurements of charm and bottom hadrons. Figure 3 left panel shows the D^0 meson nuclear modification factor, $R_{\rm AA}$, measurement in 0–10% central Au+Au compared to charged pions at $\sqrt{s_{NN}}$ = 200 GeV by the STAR experiment [9]. The measured D^0 $R_{\rm AA}$ is significantly suppressed at high p_T suggesting that charm quarks lose significant energy when traversing through the QGP. The suppression level is comparable to that of light hadrons at $p_T > 3$ GeV/c. The right panel of Fig. 3 shows the second order azimuthal anisotropy parameter, v_2, for D^0 mesons normalized by the number-of-constituent-quarks (n_q) as a function of the particle transverse kinetic energy, $(m_{\rm T} - m_0)/n_q$, and compared to other light and strange hadrons in 10–40% centrality Au+Au collisions at $\sqrt{s_{NN}}$ = 200 GeV [6]. One can observe that the D^0 v_2 follows the same universal trend as other light hadrons down to very low transverse kinetic energy, suggesting that charm quarks have gained similar anisotropic collective flow through the strong interactions with the QGP.

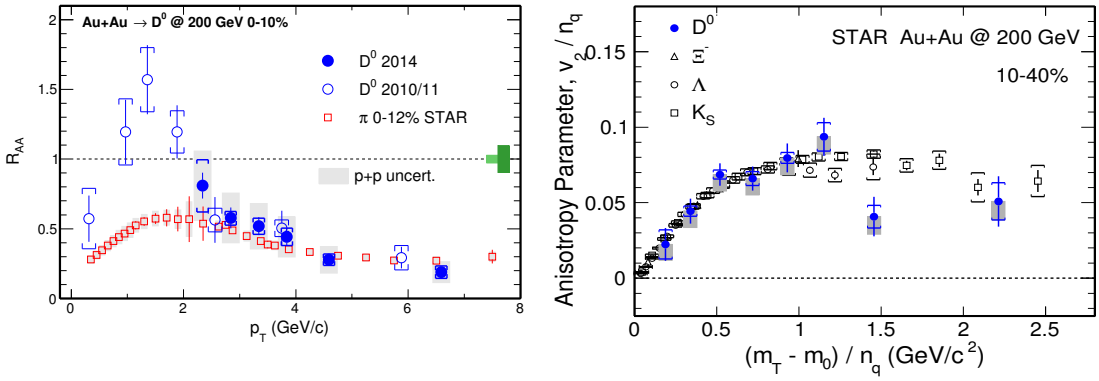

Figure 3: STAR measurements of the D^0 meson nuclear modification factor $R_{\rm AA}$ in 0–10% central Au+Au (left) [9] and elliptic flow v_2 in 10–40% centrality Au+Au (right) collisions compared to light and strange hadrons at $\sqrt{s_{NN}}$ = 200 GeV [6].

Similar measurements have been conducted by the LHC experiments. Figure 4 left panel shows the CMS measurement of $R_{\rm AA}$ for D^0 meson compared to charged hadrons in 0–10% central Pb+Pb collisions at $\sqrt{s_{NN}}$ = 5.02 TeV [10]. The right panel of Fig. 4 shows ALICE and CMS measurements of D^0 v_2 in 30–50% centrality Pb+Pb collisions at $\sqrt{s_{NN}}$ = 5.02 TeV as a function of transverse kinetic energy [11]. The CMS measurement shows v_2 of D-mesons is smaller than that of charged hadrons in the intermediate $p_{\rm T}$ region. When comparing to the v_2 measurements of light and strange hadrons at $\sqrt{s_{NN}}$ = 2.76 TeV, shown in the right figure of Fig. 4, the D^0 meson v_2 seems to approximately follow the same trend as others as well.

The large $R_{\rm AA}$ suppression and significant v_2 flow observed for D^0 mesons at both RHIC and the LHC indicate that charm quarks interact with the QGP medium very strongly and there is no apparent mass effect when compared to other light and strange hadrons despite different quark spectra and different fragmentation functions between charm and light quarks. These measurements indicate the strong coupling of charm quarks with the QGP medium. The next natural step is to go heavier and measure open bottom production in heavy-ion collisions.

The left panel of Fig. 5 shows CMS measurements of $R_{\rm AA}$ for various hadrons including charged hadrons (black circles), D^0 mesons (green squares), non-prompt J/ψ from B-hadron decays (black squares and

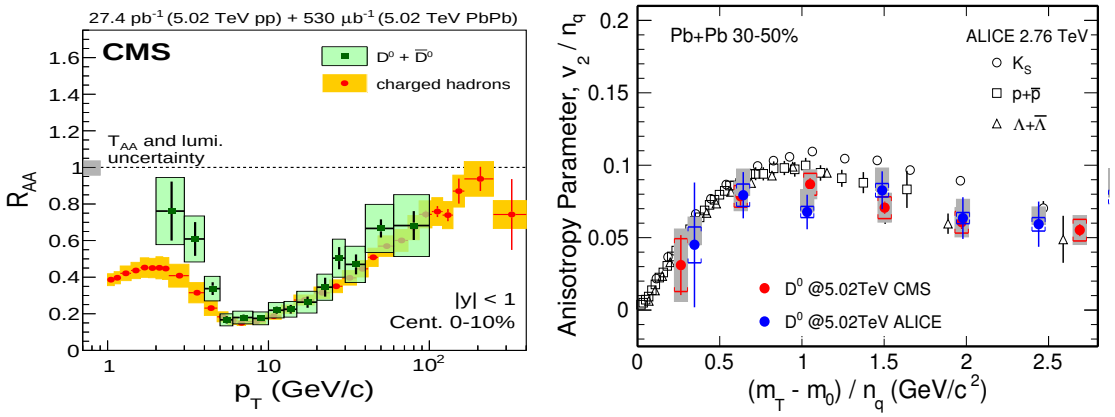

Figure 4: (Left) CMS measurement of the D^0 meson nuclear modification factor $R_{\rm AA}$ compared to charged hadrons in 0–10% central Pb+Pb collisions at $\sqrt{s_{NN}}$ = 5.02 TeV [10]. (Right) ALICE and CMS measurements of D^0 elliptic flow v_2 in 30–50% Pb+Pb collisions at $\sqrt{s_{NN}}$ = 5.02 TeV as a function of transverse kinetic energy ($(m_{\rm T} - m0)/n_q$) [11]. Also shown in the plot are ALICE measurements of the v_2 of light and strange hadrons at $\sqrt{s_{NN}}$ = 2.76 TeV.

crosses) and fully reconstructed B^+ hadrons (blue squares) in 0–100% minimum bias Pb+Pb collisions at $\sqrt{s_{NN}}$ = 2.76 TeV [10]. The B^+ meson $R_{\rm AA}$ from 9–40 GeV/c in p_T is comparable to that of charged hadrons as well as D^0 mesons within the relatively large uncertainties. However, when moving towards lower p_T, the $R_{\rm AA}$ of non-prompt J/ψ starts to show a deviation from those of charged and charm hadrons at $3 < p_T < 10$ GeV/c. The splitting shows an evidence of the mass hierarchy of $R_{\rm AA}$ suppression predicted by theoretical models and likely indicates that bottom quarks lose less energy when traversing through the QGP medium.

At the top RHIC energy, both PHENIX and STAR have reported measurements of B-hadron decay daughters in Au+Au collisions. A first indication of binary scaling of momentum integrated B-meson in Cu+Cu collisions was observed by the PHENIX collaboration [12]. The right panel of Fig. 5 shows the PHENIX measurement of the $R_{\rm AA}$ of electrons from heavy flavor decays in 0–10% central Au+Au collisions [13]. The colored bands indicate measurements of the charm and bottom decay electrons separately with decay topology selections. A hint of less suppression of bottom decay electrons compared to charm decay electrons in the region $3 < p_T < 5$ GeV/c can be seen. Similar preliminary measurements including bottom decays in J/ψ, D^0 and single electrons have been reported by the STAR collaboration [14]. Such a suppression hierarchy is consistent with the expectation that bottom quarks lose less energy in heavy-ion collisions, as predicted by several QCD models and explained in [15].

Recent achievements at both RHIC and the LHC offer us significant insights on the charm quark dynamics inside the QGP medium and also show hints of different behaviors for bottom quarks compared to light and charm quarks. One of the main goals of measuring heavy quark production in heavy-ion collisions is to characterize the QGP medium transport parameter: the heavy quark spacial diffusion coefficient and its temperature dependence. To obtain this transport parameter with constrained precision, there are still a few open questions which need detail understandings:

1. *parton energy loss: collisional vs. radiative.* The expectation should be the collisional energy loss dominates at low p_T while the radiative energy loss becomes important at high p_T. It is of particular interest how different parton energy loss mechanisms play their role from low to high p_T. Single charm hadron data have limited constraints so it is highly desired to measure different heavy quark hadrons and go beyond single observable measurements.

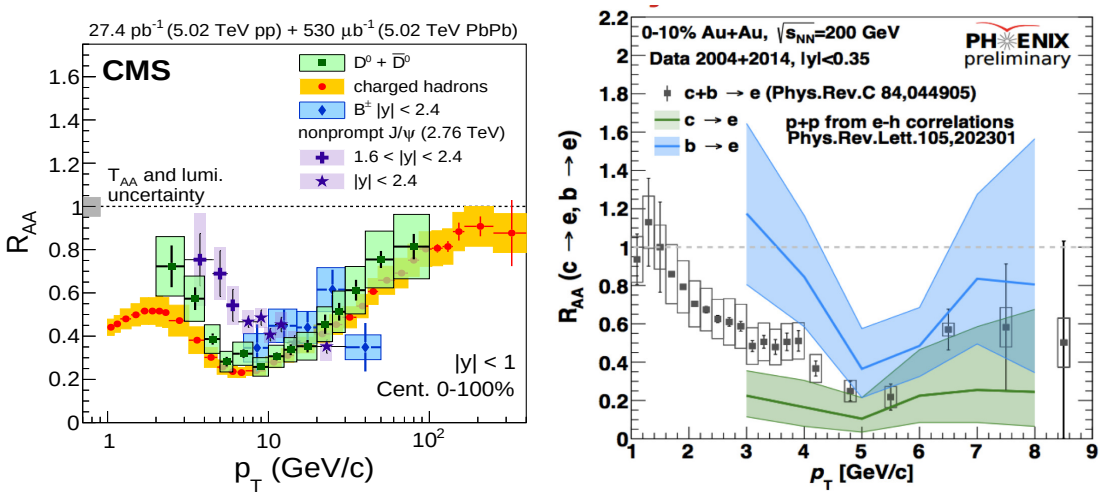

Figure 5: (Left) The $R_{\rm AA}$ of charged hadrons (black circles), D^0 mesons (green squares), non-prompt J/ψ from B-hadron decays (black squares and crosses) and B^+ hadrons (blue squares) in 0–100% minimum bias Pb+Pb collisions at $\sqrt{s_{NN}}$ = 2.76 TeV [10]. (Right) The $R_{\rm AA}$ of heavy flavor decay electrons with charm and bottom contribution separated in 0–10% Au+Au collisions at $\sqrt{s_{NN}}$ = 200 GeV [13].

2. *heavy quark hadronization: coalescence vs. fragmentation.* Recent measurements on D_s and Λ_c production in heavy-ion collisions suggest coalescence mechanism plays an important role for charm quark hadronization particularly for low to intermediate p_T regions. Lots of theoretical developments are ongoing to understand the measured enhancement and its momentum dependence. The transition from coalescence to fragmentation hadronization as a function of parton momentum is still not well controlled and this imposes large uncertainties for theoretical calculations to be able to interpret experimental data on heavy quark hadrons.

The MVTX upgrade is specially designed to address these open questions through precision measurements of B-mesons and b-jets, as well as heavy quark baryons and heavy flavor correlations. We will discuss in detail its physics potentials in the following sub-sections.

2.3 Primary physics goals for the MVTX

The primary goals of the MVTX are to provide precision measurements of open bottom hadrons and b-jets in heavy ion collisions at RHIC energies. These measurements will provide critical insights into:

1. the mass dependence of parton energy loss in the QGP medium
2. heavy flavor quark hadronization in the QGP medium
3. heavy quark diffusion transport parameter in the QGP medium and its temperature dependence

The MVTX detector and the predicted luminosities delivered to sPHENIX will allow B-meson and b-jet measurements covering a wide transverse momentum range from ∼2-40 GeV/c. The maximum p_T corresponds to 20% of the beam collision energy. For comparison, the maximum p_T reached by CMS b-jet measurements corresponds to 10% of the beam collision energy.

Precise B-meson nuclear modification measurements will cover p_T <∼15 GeV/c, where bottom and lighter quark's nuclear modifications are expected to be different, through to the high-p_T region, where the

energy lost by the quark probe in the medium does not depend on the mass. The experimental results do not yet clarify the detailed physics behind this transition.

Elliptic flow v_2 measurements made with unprecedented precision offer unique insights into the coupling of the bottom quark to the medium. Theoretical modeling using the "Brownian" motion methodology requires that momentum transfer for each interaction is much smaller than the heavy particle mass [16]. It is much better controlled for bottom quarks compared to charm quarks [17]. Therefore, precision bottom measurements over a wide momentum range, particularly in the low-p_T region, can offer significant constraints on the heavy quark diffusion transport parameter of the QGP medium along with its temperature dependence.

One point we would like to emphasize is that simultaneous measurements of B-hadrons and b-jets by the MVTX will offer new insights not only on the parton energy loss dynamics, but also on the bottom quark hadronization which has not been studied yet. The MVTX detector should also allow significantly improved measurements of charm hadrons, particularly charm baryons and charm-strange hadrons, on top of the current STAR HFT program. Detailed investigation of both charm and bottom quark hadronization should pave the way towards precision extraction of heavy quark diffusion coefficient parameters of the QGP medium.

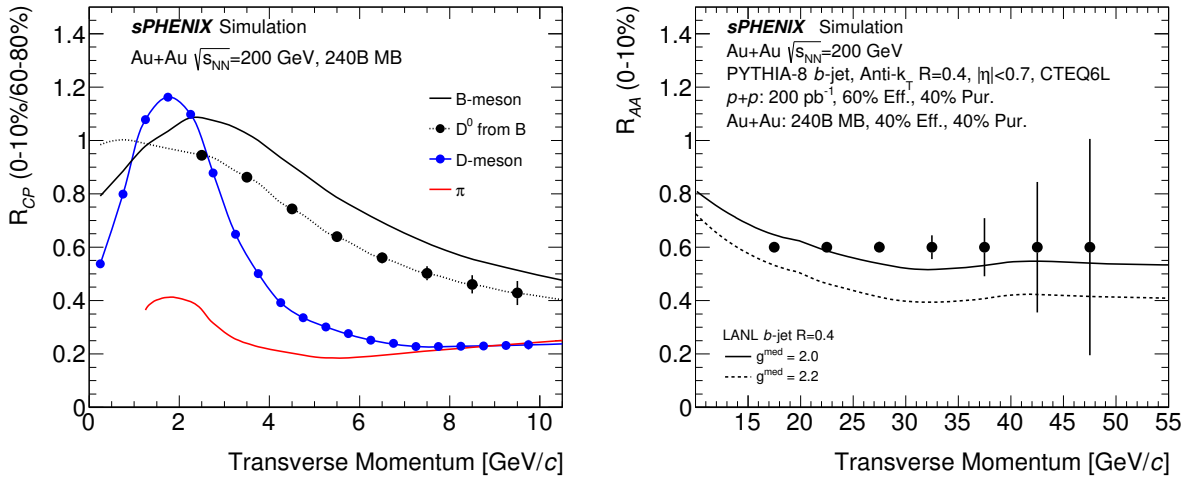

Figure 6: Projected statistical uncertainties of nuclear modification factor $R_{\rm CP}$ and $R_{\rm AA}$ measurements of non-prompt/prompt D^0 mesons (left) and b-jet (right) as a function of p_T in 0–10% central Au+Au collisions at $\sqrt{s_{NN}}$ = 200 GeV from a dataset of 240 billion minimum bias Au+Au collisions expected from the multi-year sPHENIX operation. Left: the solid blue and red lines are best fit to the RHIC data, the solid black line is from a model calculation for B-mesons and the dotted line is the theory calculation for D-mesons coming from B-meson decays. Right: the solid and dashed lines are from model calculations with two different coupling parameters to the QGP medium, $g^{\rm med}$, and the statistical projection is based on the assumption of $R_{\rm AA} = 0.6$. The MVTX will enable these highest precision B-meson measurement and the first heavy flavor jet measurement at RHIC, which will place stringent tests on models describing the coupling between heavy quarks and the QGP [1, 2, 3, 4, 5]. Details on these estimations will be discussed in Section 5.

As the key physics projections that will be enabled by MVTX, Figure 6 shows the projected uncertainties for measurements of the nuclear modification factors of heavy flavor mesons and heavy flavor tagged jets, and Figure 7 shows the projected uncertainties for measurements of the azimuthal anisotropy, v_2, for heavy flavor mesons and b-jets. Both projections show excellent statistical precision in the momentum ranges of interest.

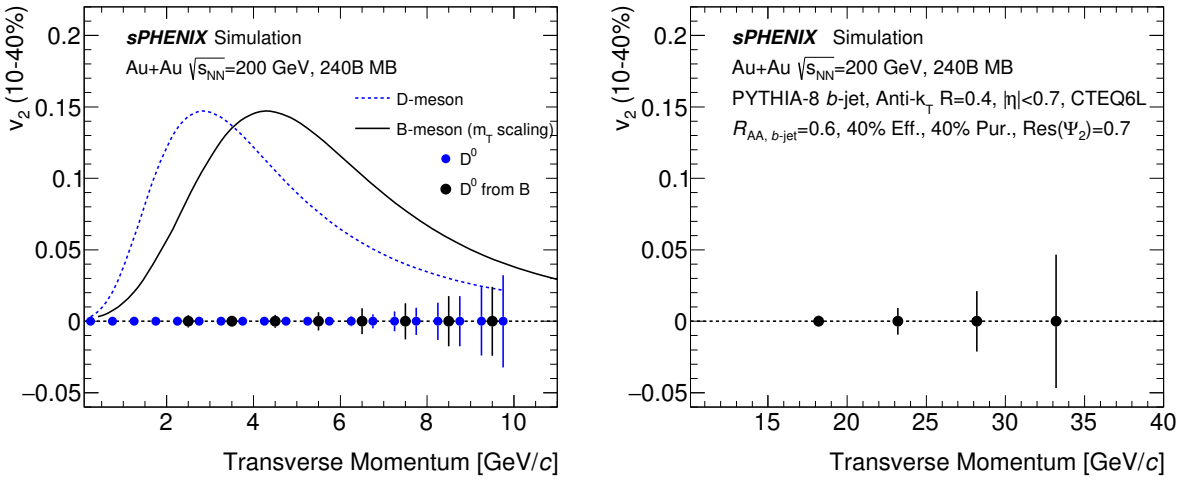

Figure 7: Projected statistical uncertainties of v_2 measurements of non-prompt/prompt D^0 mesons (left) and b-jets (right) as a function of p_T in 10–40% central Au+Au collisions at $\sqrt{s_{NN}}$ = 200 GeV from a dataset of 240 billion minimum bias Au+Au events expected from the multi-year sPHENIX operation. The purity and efficiency used in these projections are based on full event simulation and reconstruction using MVTX in sPHENIX. Left: the blue dotted line is from best fit of RHIC data, and the black line is for B-meson assuming m_T scaling in v_2 [2, 3, 4, 6]. Details on these estimations will be discussed in Section 5.

2.3.1 B-meson physics at low p_{T} (p_{T} <15 GeV/c)

As first revealed by the single-electron R_{AA} measurements at RHIC, heavy quarks lose energy when traversing the QGP medium through both radiative and elastic collisional mechanisms [18, 19]. Recent data from RHIC and the LHC show that the charm-hadron R_{AA} is quite similar to that of light flavor hadrons at high p_T [9, 20]. Theoretical calculations predict that B-hadrons should be much less suppressed compared to charm and light flavor hadrons due to the much larger bottom quark mass in the p_T region of 5–20 GeV/c at RHIC [5]. In order to systematically study the flavor/mass dependence of parton energy loss mechanisms, the next physics goal would be to measure and understand the bottom hadron production in heavy ion collisions.

Another unique feature of heavy quarks is that their propagation inside the QGP medium can be treated in analogy to "Brownian motion", because their masses are much larger than every momentum kick they suffer in the QGP [16]. Therefore, one can simplify their dynamics in the QGP with a Langevin simulation and then access the heavy quark spatial diffusion coefficient (D_s), the relevant QGP medium transport parameter, by comparing data and model calculations. Recent STAR HFT measurements reveal that the charm-hadron v_2 follows the same empirical ($m_{\mathrm{T}} - m_0$) scaling as light hadrons at $p_T < 4$ GeV/c [6] as seen in the right panel of Fig. 3. This suggests charm quarks have gained significant azimuthal collective flow. On the other hand, theoretical calculations also shows that Langevin simulation for charm quarks may have sizable corrections compared to the full Boltzmann transport [21]. To precisely determine the intrinsic QGP transport parameter, D_s, measurements of bottom hadron production, particularly at low-p_T, is critical.

Furthermore, precisely measuring the total bottom cross section in heavy ion collisions is crucial to constrain the initial state contribution to the bottom quark production, and to study the suppression of bottomonia production due to the hot medium effect, which is one of the proposed key sPHENIX measurements.

2.3.2 b-jet physics at intermediate p_{T} (15$< p_{\mathrm{T}} <$50 GeV/c)

Compared to single hadrons, measurements of jets provide more information on the initial parton kinematics and the nature of parton interactions with the QGP medium. The evolution of parton showers probes the coupling with the medium over a range of scales, providing sensitivity to its scale-dependent microscopic structure. Jets containing bottom quarks (b-jets) are of particular interest, as bottom quarks produce unique energy loss signatures due to their large mass (4.2 GeV/c^2). At momenta comparable to this scale, bottom quarks will preferentially lose energy via collisions with the plasma's quasi-particles and not via gluon radiation, which is predominant for light quarks [22]. b-jets are also distinct from light-quark jets in their hard fragmentation, where the leading heavy particle typically carries 70–80% of the jet energy [23].

So far, b-jets are measured at momenta larger than 80 GeV/c in Pb+Pb collisions at the LHC. Given relatively large uncertainty of b-jets data, these measurements indicate a nuclear modification factor (R_{AA}) not significantly different from that of the inclusive jets [24]. One possible explanation for the similarity of b-jets R_{AA} at LHC is that the mass effect of the bottom quark is small for a 80 GeV/c jet. Another hypothesis is that given that most of the high p_T b-jets at the LHC are from gluon splitting processes, the jet containing a bottom quark still behaves as a massive color octet object when crossing the medium, resembling a massive gluon [1]. These ambiguities can be resolved at intermediate p_T at RHIC energies where most b-jets are produced directly from b-quarks created in hard scatterings. Fig. 6 shows the experimental sensitivity of b-jet nuclear modification at RHIC as provided by the MVTX program:

1. b-jets can be measured with momentum as low as 15 GeV/c, one can maximally differentiate the relative contributions from various collisional and radiative energy loss mechanisms thanks to the large b-quark mass [22].

2. the main processes producing b-jets at RHIC are the leading order gluon fusion ($g+g \rightarrow b+\bar{b}$) and excitation of formerly produced b-quarks ($b+g \rightarrow b+g$). The b-quark produced in these processes crosses the medium as a massive quark (color triplet state).

Beyond the jet suppression type measurements, another new physics possibility enabled by MVTX is the measurement of b-jet azimuthal anisotropy, v_2, which is sensitive to the path-length dependent bottom quark's energy loss in QGP. When comparing to the B-meson v_2 measurement as discussed in the last subsection, jet v_2 reaches higher transverse momentum, and is less sensitive to bottom quark coalescence in the medium. Therefore, v_2 of reconstructed b-jets would provide an additional handle on probing how the heavy quark couples to the medium. The MVTX detector will allow the first measurement of b-jet v_2 at RHIC, covering a transverse momentum range of 15–35 GeV/c as highlighted on the right panel of Fig. 7.

2.4 Broad heavy flavor physics program with the MVTX

Beyond the inclusive b-jet and B-meson nuclear modification and v_2 measurements, the MVTX detector will enable a broad heavy flavor physics program, including heavy flavor baryon production, heavy flavor tagged correlations, heavy flavor jet sub-structures, etc.

2.4.1 Heavy flavor baryons

Heavy quark hadronization remains one critical factor in theory calculations in the low to intermediate p_{T} region. Recently, there have been a few observations from RHIC and LHC showing that the production of charm baryons and charm-strange mesons in heavy-ion collisions is enhanced compared to the fragmentation baseline constrained by $ee/ep/pp$ collisions [25, 26]. This suggests that coalescence mechanism plays an important role for charm quark hadronization in heavy ion collisions, similar to the light and strange hadrons. However, the current STAR HFT measurements are limited in momentum and centrality coverage

due to statistic. The MVTX detector with sPHENIX will extend this coverage, and enable precision investigation of charm baryon production in heavy-ion collisions, which has a strong connection to charm-medium interaction dynamics in non-perturbative QGP. In addition, in the case of charm baryon enhancement due to coalescence hadronization, the charm baryon contribution to the total charm quark yield may become sizable. Precision charm baryon measurements particularly down to low p_{T} will be essential to constrain the total charm yield.

2.4.2 Correlation studies for b-jets

Inclusive b-jets can originate from a high-energy bottom quark (a true bottom quark jet) or from a gluon that splits into a bottom quark and anti-bottom quark ($g \to b\bar{b}$-jet). These two categories of b-jets could potentially have very different interactions with the QGP. In the latter case the correlated bottom quark and anti-bottom quark traverse coherently through the QGP in a color octet state with twice the b-quark mass [1]. Although inclusive b-jets at RHIC are expected to be dominated by bottom quark jets [27], the remaining $g \to b\bar{b}$-jet component could complicate the interpretation of the inclusive b-jet results. The MVTX detector will allow us to better control the gluon splitting contribution to the b-jet productions and provide cleaner access to the dynamics of high energy bottom quark interactions with the QGP.

The fraction of true b-quark jets can be enhanced by selecting b-quark partonic production channels. This is achieved by requiring the b-jet candidate to be correlated with another b-jet, B-hadron, or photon in the same event [28], as illustrated in Figure 18. In particular, correlations between two b-jets can be measured with high statistics using the MVTX and sPHENIX baseline detectors, taking advantage of their high collision rate capability and their large instrumented acceptance (covering nearly 80% of produced di-jets).

2.4.3 Heavy flavor jet substructures

In recent years, the field of high-energy physics has developed a set of new techniques to inspect the substructure of jets, to tag boosted objects, and to differentiate between gluon and quark jets. These techniques have recently been adopted to study the interplay between light-jet probes with the QGP medium at the LHC [29] and at RHIC [30]. These techniques can also be utilized in identifying true bottom quark jets for sPHENIX. Specifically, so-called "jet grooming" algorithms can be used to remove soft radiation from the jet, and to identify two leading subjet structures that correspond to the earliest splitting of the initiating parton [31]. In the leading order picture, the transverse momentum of the two subjets would be similar like a $g \to b\bar{b}$-jet, while in true bottom quark jets, one subjet would likely dominate. Therefore, a measurement of the transverse momentum ratio of the two subjets can be used to identify and quantify the purity of the true bottom quark jets. A secondary vertex associated with the subjets, that is found by the MVTX, can further confirm the bottom quark origin of the subjets. Furthermore, such observables are sensitive to the fundamental QCD parton splitting functions. The modification of the bottom quark splitting functions in heavy ion collisions reveals the dynamics and coupling of the bottom quark with the QGP medium interactions [32, 33]. Figure 8 shows the expected modification of b-jet and gluon splitting functions vs the momentum ratio, Z_g, for charm and beauty jets in Au+Au collisions at RHIC top energy.

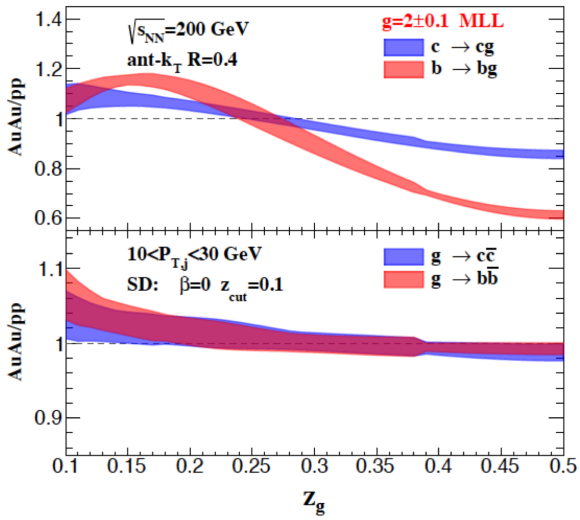

Figure 8: Modifications of bottom quark and gluon jet splitting functions for charm and beauty jets at RHIC top energy [33].

3 Detector Requirements

The planned sPHENIX detector [7, 34] is designed to perform measurements of jets and quarkonia in p+p and A+A collisions at RHIC. The baseline sPHENIX detector consists of tracking and calorimeter system, both having full 2π acceptance in azimuth, a pseudorapidity coverage of $|\eta| < 1$. Both are assembled around a 1.4 Tesla superconducting magnet coil. The full-scope sPHENIX calorimeter system includes an electromagnetic calorimeter, an inner hadronic calorimeter which sits inside the magnet solenoid coil, and an outer hadronic calorimeter located outside of the coil. The baseline tracking system includes an intermediate silicon strip tracker (INTT) and an outer time projection chamber (TPC) with space reserved for an inner vertex tracker.

The sPHENIX baseline detector allows calorimetry based triggering and measurement of jets with an energy resolution of $\Delta E/E < 120\%/\sqrt{E}$ in the p+p collisions and $\Delta E/E < 150\%/\sqrt{E}$ in the Au+Au collisions [8]. The large acceptance of the calorimetry system provides the containment of 80% of back-to-back di-jet pairs from the same hard collision. High-energy electrons can be measured by the electromagnetic calorimeter with an energy resolution better than $\Delta E/E = 15\%/\sqrt{E}$. The tracking momentum resolution is 1-2% in the transverse momentum range of 0–10 GeV/c, which provides the capability to reconstruct Υ decays from di-electrons with invariant mass resolution better than 100 MeV/c^2. The DAQ system is designed to provide a calorimetry-based trigger on jet and Υ signals, and to record full detector events at 15 kHz, which matches the collision rate delivered by RHIC within a vertex range of $|z| < 10$ cm.

3.1 Physics-driven detector requirements for the MVTX

In order to deliver the desired physics goals with b-jets and B-mesons, the following requirements are placed on the detector design:

- **Acceptance**: both b-jet and B-meson physics programs are statistics-limited. Therefore, the inner tracking detector should match the acceptance for the planned sPHENIX detector in order to provide a precision vertex displacement measurement for all tracks detected by sPHENIX. The detector should have full coverage of $|\eta| < 1$ for charged tracks with hits in at least two MVTX layers for events within $|z| < 10$ cm.

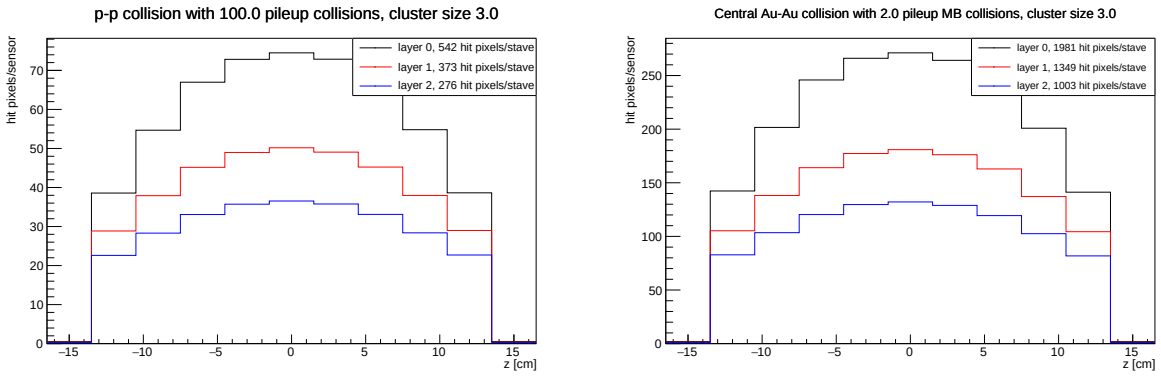

Figure 9: Average hit occupancy per event. Conservative assumptions are made regarding integration time (10 μs) and cluster size (3 pixels/cluster). In addition, the pileup collisions are assumed to occur inside the MVTX acceptance ($|Z_{Vertex}| < 10$ cm) when in fact they will be widely distributed along the beam axis.

- **Readout speed**: the b-jet physics program requires sampling a large number of events with inclusive jets and the B-meson physics program requires high statistics minimum biased Au+Au collision events. Since both programs are statistics-limited, the inner tracker should deliver an event readout rate not lower than the sPHENIX trigger rate of 15 kHz, for both p+p and Au+Au collisions.

- **Distance of Closest Approach (Distance of Closest Approach (DCA)) resolution**: The $c\tau$ for D^0 and B^0 decays are 123 μm and 456 μm, respectively, The DCA with respect to the primary vertex of these heavy-flavor mesons is larger than for prompt particles. Therefore it is crucial to achieve a DCA resolution < 50 μm at $p_T > 1$ GeV/c in order to distinguish tracks from heavy flavor hadron decays for those originating from primary charged particles. In order to achieve the required DCA resolution down to $p_T > 1$ GeV/c, the material budget of the inner tracking detector should be on the order of a few percent of a radiation length to minimize resolution degradation from multiple scattering.

- **Efficiency**: The b-jet physics program requires simultaneous detection of several displaced vertex tracks from B-meson decays within the jet; the B-meson physics program requires detection of both of the decay particle tracks from the $B \to D \to \pi^{\pm}K^{\mp}$ decay chain. A minimal tracking efficiency of 80% at p_T =1 GeV/c in the 10% most central Au+Au collisions is necessary in order to deliver the needed purity and efficiency for b-jet tagging.

These requirements are summarized in Table 1.

Item	Requirement
Acceptance	Vertex $\|z\|$ <10 cm, $\|\eta\| < 1$, full azimuthal coverage
Readout speed	Matching the sPHENIX DAQ 15 kHz event trigger rate
DCA resolution	< 50 μm for charged pions at p_T =1 GeV/c
Tracking efficiency	> 80% efficiency for charged pions at p_T =1 GeV/c in the 10% most central Au+Au collisions

Table 1: Summary for the vertex detector requirements

3.2 Hit rates and event pileup effects

With the projected RHIC beam luminosity, a collision rate up to 13 MHz (200 kHz) is expected for p+p (Au+Au) collisions in sPHENIX. Since the integration time of the ALPIDE sensor used by the MVTX (Sec. 6.2.1) is about 6–10 μs (corresponding to 57–94 beam crossings), each triggered event is expected to contain the pileup of hits from multiple collisions occurring during this detector electronics integration time window. Based on the above numbers, and assuming 10 μs integration time, an average of 130 (2.0) pileup events in p+p (Au+Au) collisions are expected per triggered event. However, less than 50% of the pileup events will be located inside the Z-vertex range of the MVTX acceptance, $|Z_{Vertex}| < 10$ cm, because the collisions are widely distributed along the z-axis ($\sigma_z \sim 40$ cm).

A preliminary study shows that these pileup events in p+p collisions can be distinguished and rejected from the hard scattering physics event of interest within the MVTX acceptance over $|Z_{Vertex}| < 10$ cm, where the primary vertex can be reconstructed and well separated from others with a resolution of ~ 20 μm. In the case of Au+Au collisions, the pileup events will increase the overall detector hit occupancy. The STAR PXL [35] detector, with 186 μs integration time, observed that the background hit density (from pileup MB hadronic collisions as well as ultra-peripheral collisions) to MB signal hit density ratio is about 6:1 at 50 kHz Au+Au collision rate. With 10 μs MVTX integration time at 200 kHz collision rate, we expect the ratio of the background hit density to MB signal to be about 1.3:1. The MVTX will also provide excellent space point resolution for matching to the INTT tracklet (which has time resolution better than the beam crossing time of 106 ns and helps to remove out-of-time MVTX hits in a triggered event), and to the inner TPC (which has a much longer integration time (~ 36 μs)) to further reduce the combinatorial fake tracks. A GEANT analysis framework is under development to fully simulate the effects of event pileup on offline track reconstruction. Detailed study with a more realistic detector response and physics event simulation is underway.

The highest occupancies are expected in layer 0, at $\eta = 0$, with central Au+Au collisions. Figure 9 shows that MVTX sensors average 271 hit pixels/event, for an occupancy of 0.052%. Lab tests (further described in Section A) have demonstrated successful MVTX readout at larger hit occupancies.

	10^{-4} noise	Hit occupancy only		Hit + noise occupancy	
	occupancy	p+p [MB/s]	Au+Au [MB/s]	p+p [MB/s]	Au+Au [MB/s]
L0 FEM	26	29	107	55	133
DAM	219	173	630	392	848
MVTX	1305	1041	3781	2346	5089

Table 2: Raw (uncompressed) data rates based on a worst-case noise occupancy of 10^{-4}, the hit occupancies of Fig. 9 at 15 kHz trigger rates, and the sum of the hit and noise.

The data rates are estimated at three points in the readout chain based on the identical ALICE ITS/IB configuration under RHIC environment. As described in Section 6.5, each Front End Module (FEM) reads out a single stave (described in 4.2), and each Data Aggregation Module (DAM) reads out eight FEMs. The data rates for a layer 0 FEM, for a DAM, and for the full MVTX are estimated in Table 2. These rates are small compared to the maximum rate capabilities of the MVTX readout: 1.2 GB/s per FEM and 16 GB/s per DAM. The total MVTX data rate is compatible with the 80 Gbps (10 GB/s) capability of the sPHENIX DAQ.

4 Technology Choices and Detector Layout

We propose to adopt the ALICE ITS Upgrade 3-layer MAPS-based Inner Barrel (IB) detector design, with minimal modifications to both electrical and mechanical systems, for use in the sPHENIX experiment. ALPIDE is a version of the Monolithic Active Pixel Sensor (MAPS) developed for particular application in ALICE. In the text of this proposal both names, MAPS and ALPIDE, are used interchangeably. A full description of the ITS Upgrade can be found in the Technical Design Report [36].

Figure 10 and 11 show the side and cross-section views of the sPHENIX MVTX detector mounted on the sPHENIX beam pipe. Sitting outside of the MVTX is the silicon strip sensor based intermediate tracker (INTT) planned to be funded by the RIKEN research institute in Japan. INTT will cover roughly from 6 cm (INTT layer-0) to 12 cm (INTT layer-3) in radius and $|\eta| \leq 1.1$ in pseudorapidty. With single-event response and spatial resolution between that of the MVTX detector and that of the TPC, the INTT is intended to support pattern recognition and data-driven calibrations in p+p and A+A collisions. The precise geometry and configuration of the INTT is being optimized, and that effort is not part of this proposal. The TPC is part of the sPHENIX baseline detector and covers radius from 20 cm to 78 cm (active volume in $30 \leq R \leq 78$ cm) and pseudorapidity $|\eta| \leq 1.1$.

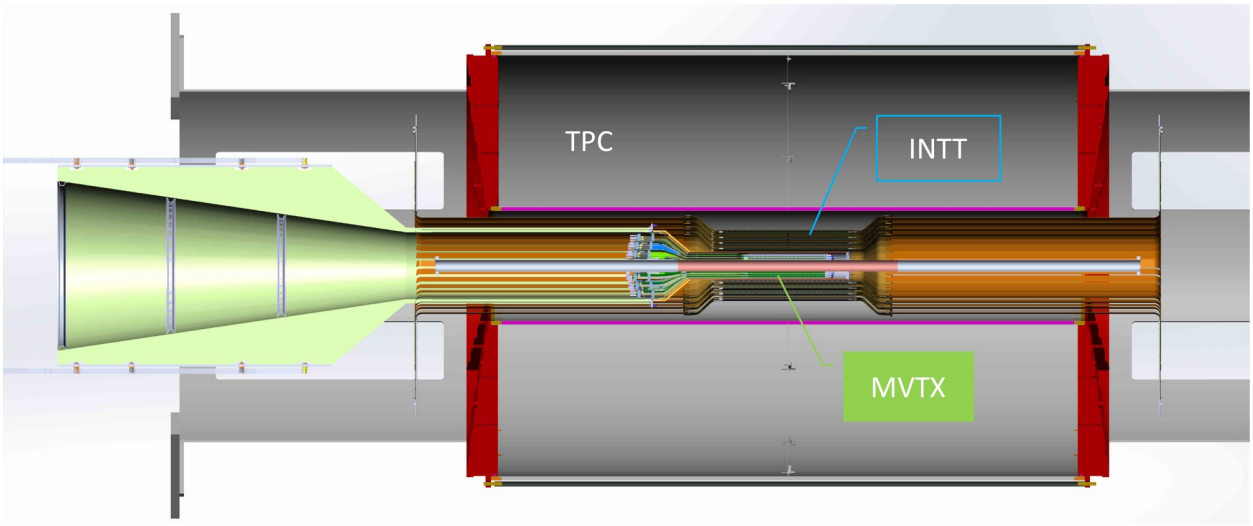

Figure 10: Side view of the sPHENIX tracking system, showing the MVTX's location relative to the sPHENIX beam pipe, intermediate silicon strip tracker (INTT) and time projection chamber (TPC). All services come from one end (left side), including analog and digital power, cooling lines and high-speed Firefly data cables.

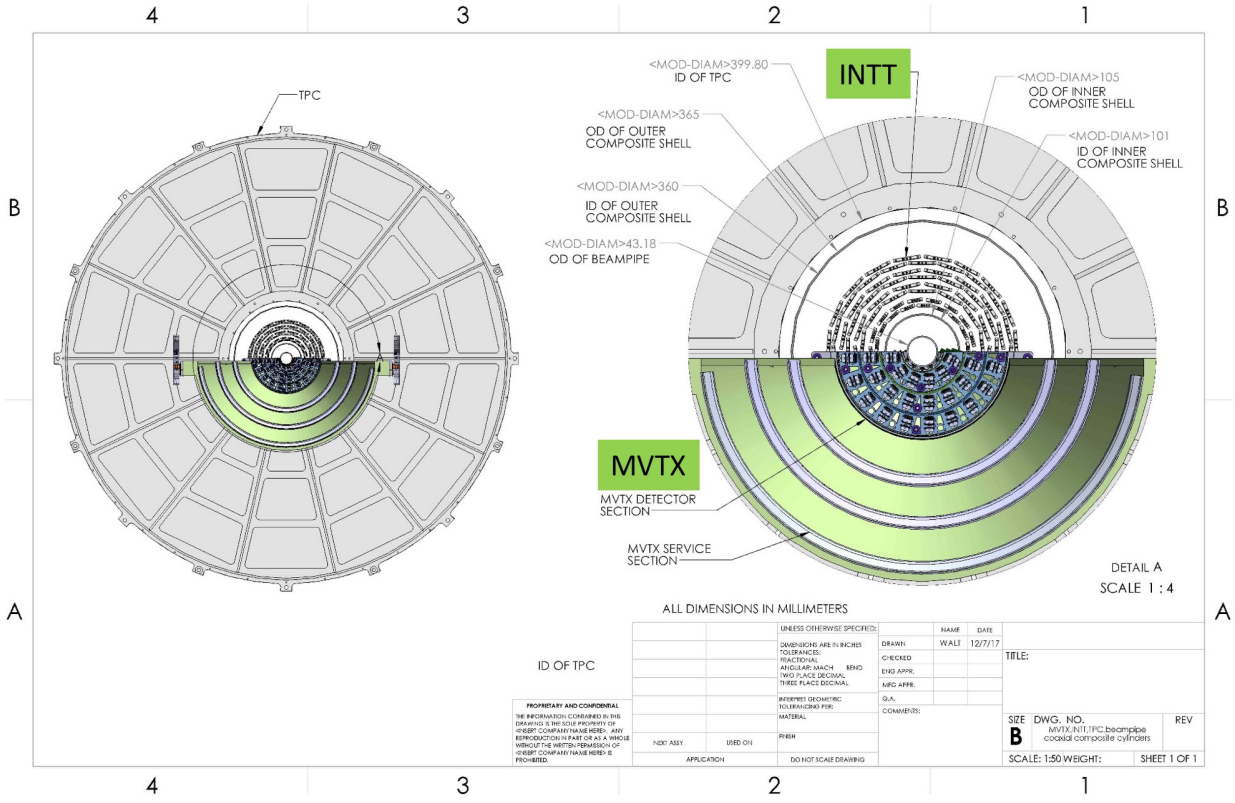

Figure 11: Cross-section view from CAD model of the sPHENIX tracking system, showing the MVTX's location relative to the sPHENIX beam pipe, intermediate silicon strip tracker and time projection chamber.

4.1 Design goals and technology choice

Recent developments in the technology of MAPS have made it possible to have sensor designs with high speed readout, fine granularity, minimal radiation length and low power, all at relatively low cost. The ALPIDE sensor [37, 38] developed for the ALICE ITS Upgrade has attributes that meet the sPHENIX requirements. We have focused our design on leveraging the extensive R&D work already done for the ALICE ITS. We intend to use the design of the inner three layers of the ALICE ITS as the primary baseline design for the sPHENIX MVTX, providing the basis for the designs and work plans in this proposal. On the basis of the requirements and considerations of Section 3, the proposed solution for the layout of the MVTX is a 3-layer silicon barrel based on the technology of MAPS. The main design considerations to meet the necessary capabilities in terms of displaced vertex resolution, tracking efficiency and readout rate, are summarized here:

- The track pointing resolution is mainly determined by the two innermost measurements of the track position. This requires the first detection layer be as close to the beam line as possible. Three layers provide redundancy against failure of detector modules. The radial distance between the three layers

should be comparable to the distance between first layer and the vertex to preserve the precision of vertex projection from the two innermost measurements of the track position with a redundancy of one measurement point. attached to it.

- Reduction of the material budget to minimize multiple-scattering track distortion. Reducing the material budget of the first detection layer is particularly important for improving the impact parameter resolution.

- The segmentation of the detector determines the intrinsic spatial resolution of the reconstructed track points. Excellent spatial resolution of the first layer is key for the resolution of the impact parameter at high particle momentum where the effect of the multiple scattering becomes negligible. Fine segmentation is also important to keep the occupancy low.

- Short integration time window to minimize the event pile-up and keep the occupancy at a low value when reading out the detector at the expected top collision rate of $\sim$200 kHz in the Au+Au collisions and $\sim$ 13 MHz in the p+p collisions.

These design goals lead to a vertex detector configuration consisting of three concentric layers of pixel detectors. The Monolithic Active Pixel Sensor (MAPS) are implemented using the 0.18 μm CMOS TowerJazz technology and developed by the ALICE collaboration at CERN are an ideal technology for the three layers. The basic active MVTX element is the Pixel Chip. It consists of a single silicon die of about 15 mm x 30 mm, which incorporates a high-resistivity silicon epitaxial layer (sensor active volume), a matrix of charge collection diodes (pixels) with a pitch of about 30 μm, and the electronics that perform signal amplification, digitization and zero-suppression. Only the information on whether or not a particle crossed a pixel is read out. The main functional elements of the sPHENIX MVTX detector are introduced in the following section.

4.2 Detector layout

The proposed sPHENIX MVTX detector is designed to leverage the extensive research and development behind the design of the ALICE ITS Upgrade Inner Barrel. In the ALICE design, the layers are azimuthally segmented in units called staves, which are mechanically independent. Staves are fixed to a support structure, half-wheel shaped, to form half-layers. The stave and the half-layer are shown in Figure 12).

The term *stave* will be used to refer to the complete detector element. It consists of the following main components:

- Space Frame: a truss-like lightweight mechanical support structure for the single stave based on composite material (carbon fiber).

- Cold Plate: carbon ply that embeds the cooling pipes.

- Hybrid Integrated Circuit (HIC): assembly consisting of the polyimide flexible printed circuit (FPC) on which nine Pixel Chips and some passive components are bonded.

Each stave will be instrumented with one HIC, which consists of a row of nine Pixel Chips glued and connected to the FPC, hence covering a total active area of 15 mm x 271.2 mm including the 150 μm gap between adjacent chips along z. The interconnection between Pixel Chips and FPC is achieved via wire bonding. The HIC is glued to the Cold Plate with the Pixel Chips facing it in order to maximize cooling efficiency. An extension of the FPC connects the stave to a patch panel that is served by the electrical services entering the detector from one side only. A mechanical connector at each end of the stave allows

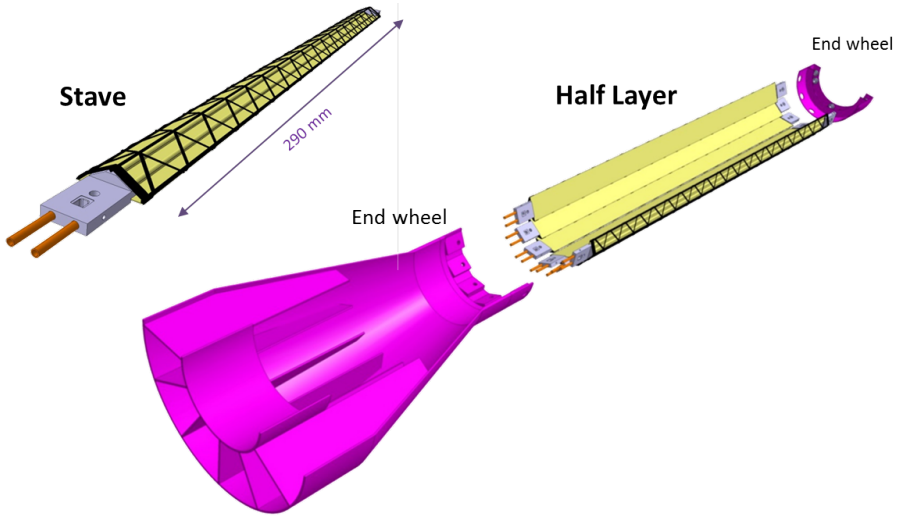

Figure 12: MVTX Stave and Half-Layer: each half-layer is composed of a set of staves fixed to wheel-shaped support structures. The layout shown here is from the ALICE ITS IB design. For MVTX, the barrel part of the left-hand side End-Wheel will be extended by about 230mm.

the fixation and alignment of the stave itself on the end-wheels, as described in Section 6.7. The inlet and outlet of the closed-loop cooling circuitry are located at the same end of the stave because the cooling is also served from the same side as all other services. The prototyping of the stave is well advanced. The design of the stave accounts for the tight requirement on the material budget, which is limited to 0.3% X_0.

Similar to the ALICE ITS IB design, the staves will be assembled in three cylindrical layers with the main geometrical parameters are listed in Table 3. The radius of each layer is increased by 1.3mm from the baseline ALICE ITS IB design to fit the existing sPHENIX beam pipe, which leads to minimal change in both tracker coverage and DCA resolution according to GEANT4 simulations. The three layers of the MVTX are then integrated together with an outer cylindrical structural shell (CYSS) to form two detector half barrels, as shown in Figure 13. Figure 14 shows the detail side view of the MVTX with INTT.

	Layer 0	Layer 1	Layer 2
Radial position (min.) (mm)	23.7	31.4	39.1
Radial position (max.) (mm)	28.0	35.9	43.4
Length (sensitive area) (mm)	271	271	271
Active area (cm^2)	421	562	702
Number of pixel chips	108	144	180
Number of staves	12	16	20

Table 3: Parameters of the sPHENIX MVTX design.

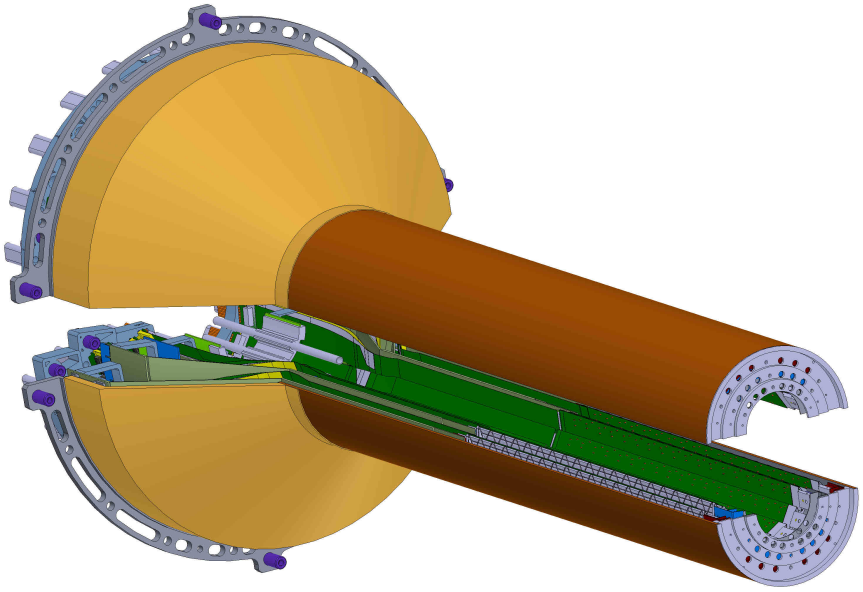

Figure 13: MVTX 3-layer Detector Barrel: each half-barrel is composed of a detector section and a services section. Note the cylindrical section is extended in Z-direction to free up space for INTT outside of the MVTX barrel.

5 Detector Performance and Projected Physics Sensitivity

In this section, we discuss the detector performance and physics capabilities of the MVTX incorporated into the baseline sPHENIX detectors. As shown in Sec. 4, the baseline sPHENIX tracking system consists of the INTT and the TPC detectors, which provide excellent pattern recognition and momentum measurement. The sPHENIX tracking is further augmented by MVTX, which provides high precision vertex reconstruction and is critical for the open heavy flavor physics program. The performance of this detector system is studied using the GEANT4-based [39] sPHENIX simulation package which contains a detailed detector description of MVTX. The digitized signal in the tracking detectors are analyzed using the sPHENIX offline reconstruction chain, which features a Kalman-filter-based generic tracking module and a RAVE-based [40] vertexing module. A reconstruction event display is shown in Fig. 15.

Following the sPHENIX five-year (2022-2026) running scenario and luminosity projections [41], and with the 15kHz high rate trigger capability, we expect the MVTX program will have the following data samples:

- Sampling 200 pb^{-1} p+p collisions at $\sqrt{s} = 200$ GeV via a jet patch trigger. We expect the jet patch trigger is fully efficient in the p+p collisions above a threshold of around 7 GeV/c [8], and therefore provides a complete coverage for the b-jet program which requires $p_T > 15$ GeV/c.
- Recording 240 billion minimum bias Au+Au collisions at $\sqrt{s_{NN}} = 200$ GeV. No trigger addition to the minimum bias collision trigger is assumed.

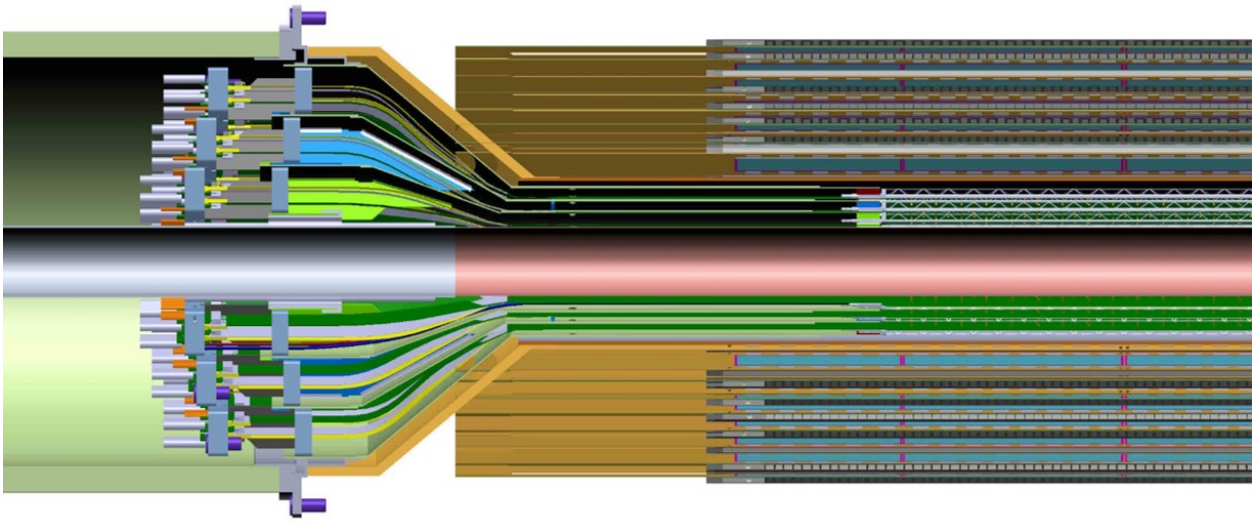

Figure 14: Detail view of MVTX and INTT: The conical region of the MVTX detector barrel is extended in Z by about 230mm from the ALICE baseline design to clear space for INTT services.

The sPHENIX physics program also include a large data set of p+A collisions too which will further enrich the MVTX physics program. In this section, We will begin the discussion with the tracking performance, which is followed with capabilities and projections for the physics measurements as outlined in Sec. 2.

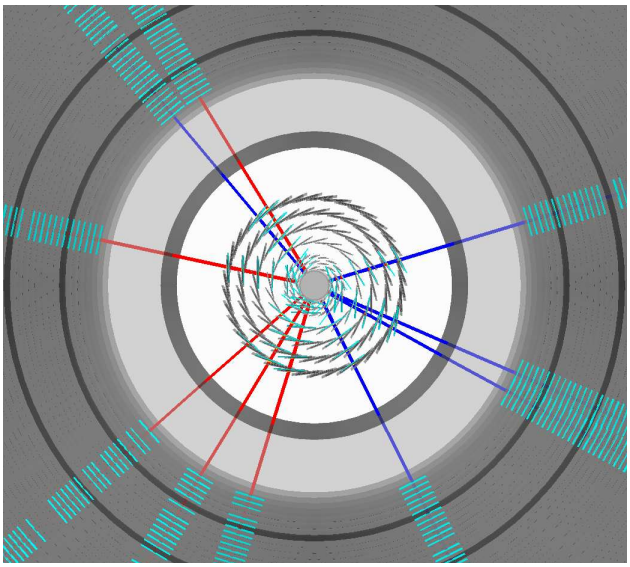

Figure 15: An event display of reconstructed tracks (red and dark blue lines) with the active component of MVTX, INTT and the inner layers of TPC shown in gray. Detailed geometry information is used by a Kalman-filter-based algorithm [42] to assemble tracking detector hits (cyan lines mark hit planes) and reconstruct tracks.

5.1 Tracking performance

The MVTX allows us to precisely reconstruct the primary vertex and the displaced secondary tracks, which is required for detecting heavy flavor hadron via its decay topologies. Key tracking performance parameters: the DCA pointing resolutions, the single track efficiency and the transverse momentum resolution are shown as a function of the tracks transverse momentum, p_T, in Fig. 16. The results are based on pion tracks embedded in the central Au+Au collisions, simulated in a full GEANT4 detector simulation, and analyzed using the offline tracking software reconstruction (see Section 6.11 for details on offline software). The primary vertex resolution is better than 5 μm for collision vertexes with 50 charged tracks or more produced in the MVTX acceptance and contributes only a minor factor to the DCA pointing resolutions in the heavy ion collisions. Both the sPHENIX baseline detector (INTT + TPC) and the sPHENIX + MVTX upgrade (MVTX + INTT + TPC) are studied. With the addition of MVTX, the DCA pointing resolutions are improved by a factor of 3–10, as MVTX adds high precision track space-point measurement ($\sigma \sim$5 μm) very close the collision vertexes (R =2–4 cm). Minor improvements are also observed in the transverse momentum resolution for the high momentum tracks. This mainly stems from the extended the inner radial tracking level arm from $R \sim$6 cm (first layer of INTT) to $R \sim$2 cm (first layer of MVTX). If further assuming the tracks originate from the primary collision vertex and including collision vertex in track fit, the momentum resolutions in both configurations improve and the difference becomes negligible. The tracking efficiency with and without MVTX are similar and therefore we choose plot one tracking configuration in the left bottom panel in Fig. 16.

With the MVTX detector, the single track efficiency is above 90% at p_T =1 GeV/c and the DCA pointing resolutions in both $r\phi$ and z dimensions are about 40 μm for 0.5–1 GeV/c tracks. These performance parameters exceed the detector requirements as described in Sec. 3, allowing for the precision heavy flavor measurements described in the following sections which would be otherwise impossible without MVTX.

5.2 Heavy flavor tagged jets

At RHIC, the detection of heavy flavor tagged jets (HF-jets), in particular of b-jets, is complicated by their comparative rarity ($<$ 1% of the inclusive jet yield) as shown in Fig. 17, and also by the significant background of the underlying event in heavy ion collisions. Taking advantage of the high precision tracking provided by the MVTX detector, multiple exploratory HF-jet tagging methods have been developed to demonstrate that the proposed MVTX detector allows the first b-jet measurement at RHIC, which would lead to stringent tests of the theories describing the interactions of high energy parton with the QGP.

The b-jet measurement is also built upon the full calorimetric jet measurement at sPHENIX, that includes the triggering of jets in the p+p collisions (fully efficient $p_T > 7$ GeV/c), the large data bandwidth of 15 kHz and the determination of the jet energy with combined information from the trackers, the electromagnetic calorimeter and the hadronic calorimeters [7, 8]. Despite the rarity of b-jets, the high statistics inclusive jet data sample will allow us to measure b-jets with a transverse momentum reach higher than 30 GeV$/c$. Meanwhile, the lower transverse momentum reach of the b-jet is limited by the systematical uncertainty from the fake jets in the central Au+Au collisions. As discussed in Ref. [7], by performing iterative background subtractions and then correlating the calorimetric jet candidates with tracking information, the inclusive jet purity and fake jet suppression is significantly improved, and the track-tagged light jet measurement is feasible down to the p_T =10–20 GeV/c region. Considering b-jet tagging usually requires jets contain multiple high momentum displaced tracks, in this proposal we assume the single b-jet measurement can reach to a lower-p_T limit of 15 GeV$/c$, and the sub-leading b-jet in the di-b-jet event can reach to a lower-p_T limit of 10 GeV$/c$. The collaboration is actively evaluating these assumptions for b-jets and improving its fake jet rejection.

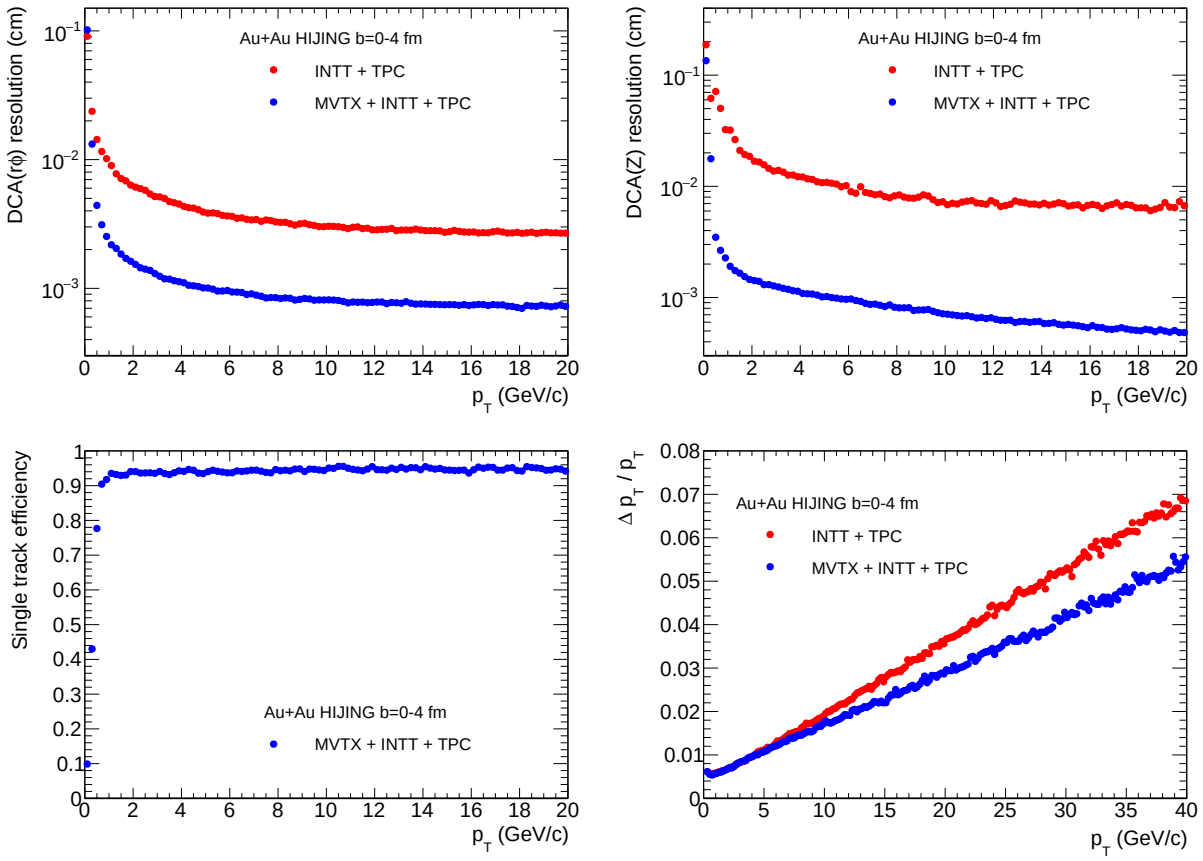

Figure 16: Top: DCA pointing resolution in the bending plane (left) and along z-axis (right). Bottom: single track reconstruction efficiency (left) and transverse momentum resolution (right). These parameters are simulated with pions embedded in central Au+Au collisions using sPHENIX simulation and reconstruction chain, and they are plotted against the truth transverse momenta of the pions. Two detector configurations are compared: that is the sPHENIX baseline detector with (blue) and without MVTX (red) installed which shows critical improvement over pointing resolution with the addition of MVTX (see text for details).

5.2.1 HF-jet tagging performance

As shown in Fig. 18, the *b*-jet-tagging methods are based on the unique features of B-hadron decays, including the finite decay length and leptonic decay products. Specifically, the tagging methods explored with MVTX include:

- Identification using track displacements:
  Identify *b*-jets by requiring multiple tracks within the jet cone that do not originate from the primary collision vertex. These are likely to be the long-lived B-hadron decay products. A full sPHENIX and MVTX simulation is used to demonstrate such capability in p+p and central Au+Au collisions as shown in the left side panels of Fig. 19 and 20. Each plot includes the *b*-jet tagging performance with different requirements on the number of tracks showing a large DCA significance along the jet-axis direction. The performance with a requirement of two (three) tracks shows a better efficiency (purity). Additional techniques will be deployed in the final software package to further optimize performance, including likelihood analyses and particle flow algorithms.

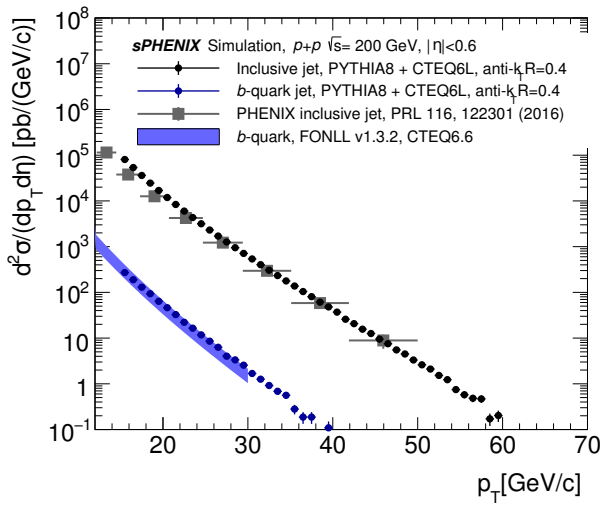

Figure 17: Comparison of the cross section for b-jets (blue) and all jets (black).

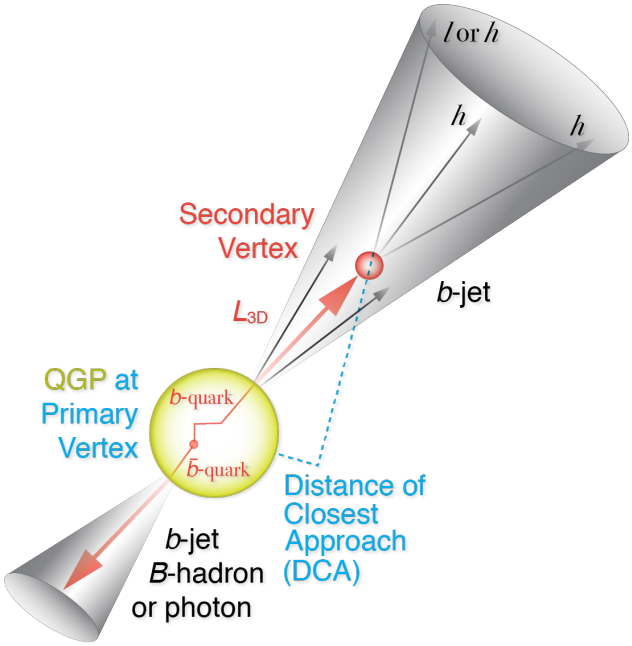

Figure 18: A bottom quark traverses the QGP and fragments into a b-jet. The principles of tagging the rare b-jets are based on unique features of B-hadrons: long lifetime and finite decay length of B-hadron (L_{3D} ~few mm), decay tracks from secondary vertices and leptonic decay products.

- Identification using secondary vertices:
  Identify b-jets by requiring that multiple tracks within the jet cone come from the same displaced secondary vertex distinct from the primary vertex. The most deviated secondary vertex among multiple candidates within the jet cone is used to identify b-jets. This method is related to the previous one;

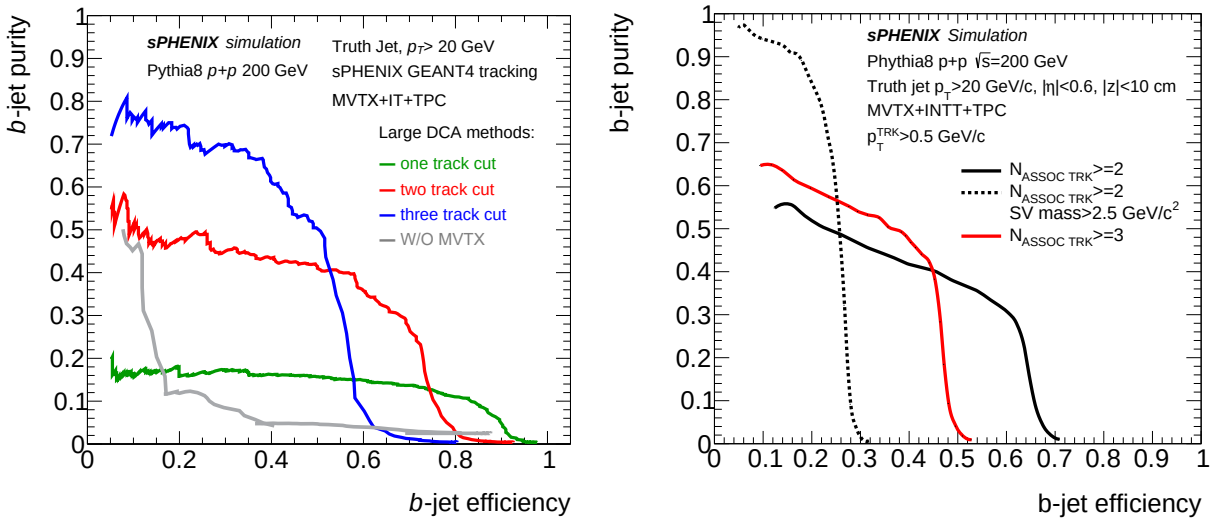

Figure 19: Projected b-jet tagging performances in p+p collisions using the multiple large DCA track method (left panel) and secondary vertex method (right panel), which is estimated in full sPHENIX GEANT4 and reconstruction chain. If without MVTX, b-jet tagging capability in the p+p collisions would be severely limited, as shown by the gray curve on the left panel.

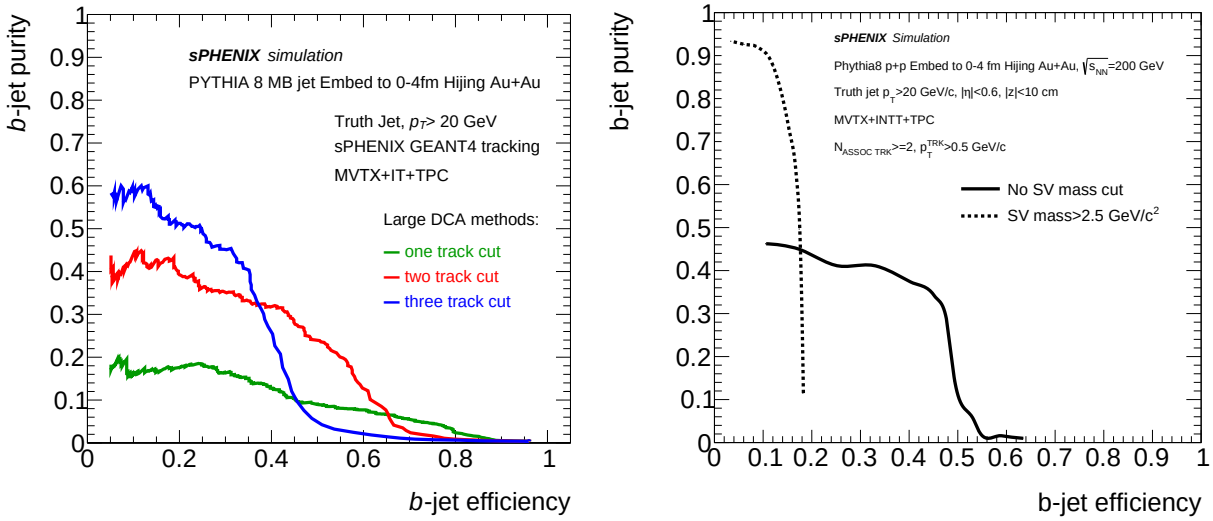

Figure 20: Projection of b-jet tagging performances in central Au+Au collisions in sPHENIX + MVTX, using the multiple large DCA track method (left panel) and secondary vertex method (right panel). This result is estimated suing the full sPHENIX GEANT4 and reconstruction chain. The performance curves allow the aimed analysis working point of 30-40% purity at 30-40% b-jet efficiency, which is also used in the existing analysis performed at LHC energy for higher energy jets [24]. If without MVTX, tagging of b-jet would be unfeasible in sPHENIX in the central Au+Au collisions.

however it also uses the knowledge that a B-hadron is likely to decay into multiple daughter particles. This provides additional power in selecting and cross checking b-jet candidates identified via the first method. We also demonstrated this method in full simulations of p+p and central Au+Au collisions as shown in the right panels of Figs. 19 and 20. This method also provide data driven quantification of b-jet purity via secondary vertex kinematics fitting.

- Identification using leptons from B-hadron decays:
  Identify b-jets by requiring that electron or positron tracks are detected within the originally identified jet cones. Utilizing the fact that B-hadrons have a considerable chance ($\sim 10\%$ [43]) to decay to a leptonic final state, this is a nearly orthogonal method that could provide an independent systematic cross check of both methods above. We will explore its feasibility in the sPHENIX environment and performance projections for such cross checks.

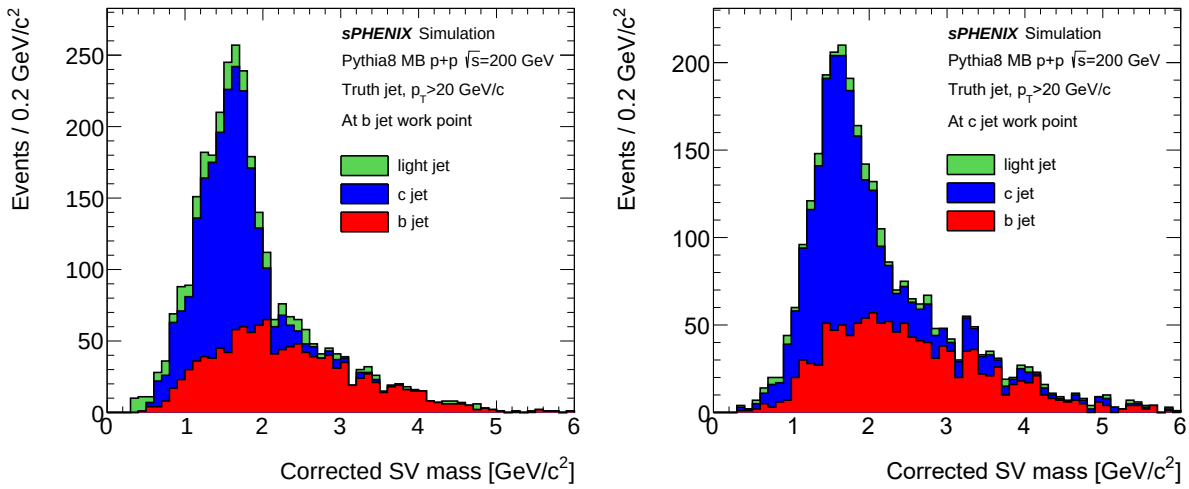

Figure 21: Distribution of corrected secondary vertex mass of light-jet, c-jet, and b-jet in p+p collisions at selected working points for b-jet (left) and c-jet (right) measurements. The correction takes into account possible missing energy due to neutral particles or tracking inefficiency, which enhanced the differentiation power between the jet flavors.

Supported by both tagging methods of track displacements and secondary vertices, the b-jet tagging working points are selected as 60% efficiency, 40% purity in the p+p collisions (Figs. 19) and 40% efficiency, 40% purity in the 10%-most central Au+Au collisions (Figs. 20). The b-tagging performance approaches that seen by CMS in their b-jet analysis for higher transverse momenta jets at the LHC collision energies [24, 44]. These work points are used in the next subsection (Sec. 5.2.2) for the projections of the b-jet observables.

After the initial identification of b-jet candidates, the purity of b-jets in the candidate sample will be quantified in a data-driven way using the invariant mass and transverse momentum of the secondary vertex, which has proven to be critically important in the LHC environment [24, 44]. Figure 21 shows distributions of corrected secondary vertex mass for different flavor jets in p+p collisions. The correction takes into account possible missing energy due to neutral particles or tracking inefficiency. These distributions are at the selected working points for b-jet measurements (left) with moderate efficiency ($\sim 40\%$) and good purity ($\sim 60\%$) or c-jet measurement (right) with low efficiency ($\sim 10\%$) but good purity ($\sim 60\%$). The contribution from light quark jets is highly suppressed at the selected working points, and it shows clearly distinguishable shapes between b-jets and c-jets.

5.2.2 Projections for b-jet

The projected statistical uncertainty of the nuclear modification of inclusive b-jets is shown in Fig. 22, which covers the transverse momentum region of 15–40 GeV/c. The data samples assumed in this estimation are listed in the beginning of this section, which including 200 pb^{-1} p+p collisions and the most-central-10% of 240 billion minimum bias Au+Au collisions at $\sqrt{s_{NN}} = 200$ GeV. In the p+p collisions, a

jet patch trigger is assumed to sample the full luminosity delivered to the vertex acceptance of the silicon tracker. The relative statistical uncertainty of b-jet yield is estimated as $\delta y/y = 1/\sqrt{Pur \times Eff \times N_{b\text{-jet}}}$, where b-jet's purity (Pur) and efficiency (Eff) are concluded from the last subsection. $N_{b\text{-jet}}$ is the expected count of the truth b-jet within the sPHENIX acceptance, which is the product of the b-jet differential cross section (Fig 17), phase space per bin, $R_{\rm AA}$ (in central Au+Au collisions, assuming $R_{\rm AA}$ = 0.6) and the projected p+p equivalent luminosity [41]. We note this formula for statistical uncertainty estimation assumed that the yield of the background after the b-jet tagging is well determined, which is a non-trivial task. Nevertheless, the collaboration is establishing methods of background determination and studying the associated systematic uncertainties. The relative statistical uncertainty from both the data samples of p+p and Au+Au collisions are then quadratically summed as the relative statistical projection of $R_{\rm AA}$. They contribute compatibly to the final $R_{\rm AA}$ uncertainty, which underscore the importance of high statistics data from both collision systems. The sPHENIX and MVTX b-jet projection as shown in Fig. 22 will be the first heavy flavor jet $R_{\rm AA}$ data at RHIC and will place stringent constraints on models describing the coupling between heavy quarks and the QGP [1]. We are also in close collaboration with theory groups to update the model predictions of inclusive b-jet nuclear modification at RHIC energies in the sPHENIX kinematic region.

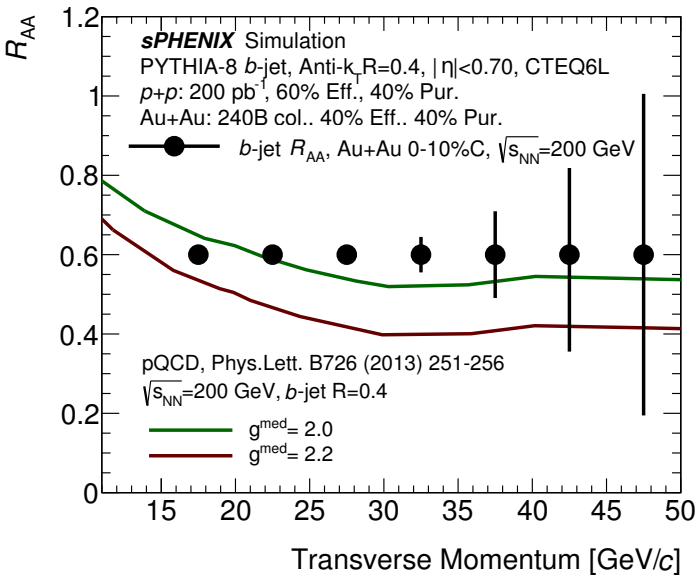

Figure 22: Statistical projection of sPHENIX + MVTX inclusive b-jet data in terms of the nuclear suppression factor, which is compared with QGP transport models for bottom quark jets evaluated at the RHIC energy (curves) [1]. Given the large theoretical uncertainty of b-jet $R_{\rm AA}$, this study assumed a constant $R_{\rm AA} = 0.6$ when evaluating the statistics. MVTX enables the b-jet tagging in sPHENIX in the Au+Au collisions. And it will bring the first b-jet suppression data to RHIC energy and to the 15–40 GeV/c transverse momentum region in which b-quarks move slowly and are predicted to show strong deviations from light quark jets. These data will place stringent constraints on models describing the coupling between heavy quarks and the QGP, such as constraining the bottom quark's coupling parameters to the QGP medium, $g^{\rm med}$ in [1].

Although the b-jet is not expected to flow with medium, the path-length dependent energy loss of the b-jet can leads to an event-plane dependent azimuthal modulation on the jet yields, e.g. v_2. By correlating b-jets with the event plane, the b-jet v_2 can also be measured with the MVTX, covering a transverse momentum range of 15–30 GeV/c. The statistical uncertainty for v_2 is estimated as $\delta v_2 = 1/(\sqrt{2}\sqrt{Pur \times Eff \times N_{b\text{-jet}}} \times$

$Res(\Psi_2)$). Two event plane resolutions, $Res(\Psi_2)$, are assumed in this projection. One case shown in the left panel of Fig. 23 is based on a reconfiguration of the PHENIX beam-beam counters in which $Res(\Psi_2) \approx 0.4$. Another case shown in the right panel of Fig. 23 is with a dedicated event plane detector upgrade to sPHENIX with which $Res(\Psi_2)$ can reach ≈ 0.7. This data will extend the B-meson v_2 measurement to higher b-quark transverse momentum, and provide a strong constraint on the path-length dependence of bottom quark's energy loss, and possible interplay between collisional vs radiative energy loss in QGP.

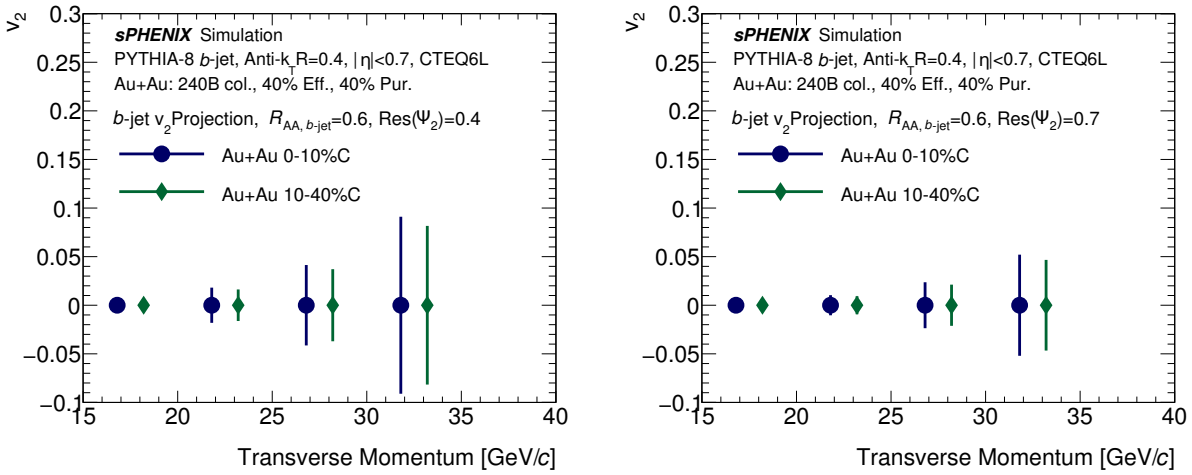

Figure 23: Statistical projection of sPHENIX inclusive b-jet elliptical flow under the assumptions that the event plane resolution is 0.4 (left) and 0.7 (right). See text for discussions.

The large acceptance for di-jets enables the MVTX to simultaneously detect b-jet pairs produced in the same collision and to perform bottom dijet asymmetry measurements. A preliminary projection of the transverse momentum balance of b-jet pairs is shown in Fig. 24. When selecting dijet pairs, we require the leading jet to have $p_T^1 > 20$ GeV/c and the sub-leading jet to have $p_T^2 > 10$ GeV/c. The $x_j = p_T^2/p_T^1$ distribution under these requirements is extracted from PYTHIA, the shape of which is assumed to be unmodified in Au+Au collisions for this projection. Figure 24 shows the projected statistical uncertainties on the measurement, which approach the precision of a recent result from Pb+Pb collisions at $\sqrt{s_{NN}} = 5.02$ TeV measured by the CMS collaboration [44]. Note that while we expect the efficiency and purity for di-b-jets to be larger than that of inclusive b-jets, for this preliminary projection we have used the same efficiency and purity working points, as detailed di-b-jet studies are ongoing. We are also working with theory community to obtain models on the modification of x_j so that the projection can be adjusted with a centrality dependence. By comparing with the inclusive single b-jet modifications, this measurement will further provide insights on energy loss of the b-quark jets and that of the $g \to b\bar{b}$-jets.

We further note that in Fig. 22 to 24, only the statistical uncertainty is shown. The systematic uncertainty will be very important for the b-jet measurements too, in particular for the lower transverse momentum bins where statistical uncertainty is small. The collaboration is actively working on various approaches to reduce the systematic uncertainty via data driven methods, such as a template fitting on the secondary vertex mass spectrum as shown in Fig. 21.

5.3 B-meson tagging performance

B-meson production can be studied through either inclusive decay daughters, e.g. D-mesons, J/ψ or $e^{\pm}$ via the impact parameter method or exclusive reconstruction, e.g. $\overline{D}+\pi$ or $J/\psi+K$ etc via the reconstruc-

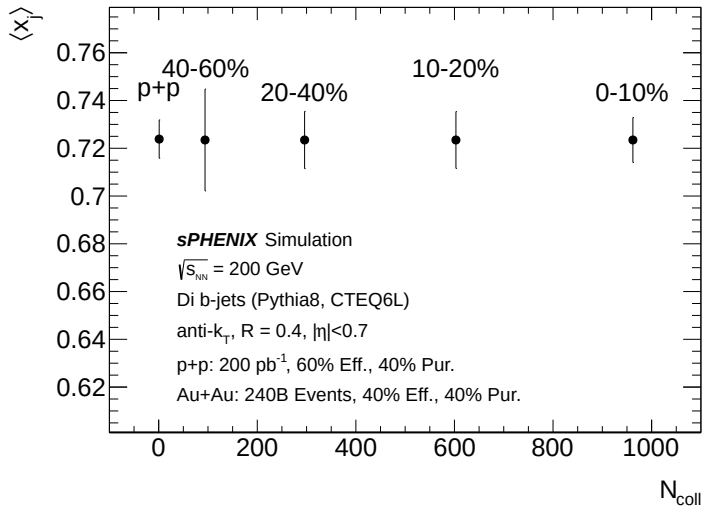

Figure 24: Projections for the mean di-b-jet transverse momentum balance, $\langle x_j \rangle$ as a function of $N_{\rm coll}$ in p+p and Au+Au collisions at $\sqrt{s_{NN}}$ = 200 GeV.

Hadron	Decay Channel	B.R.
b-hadron admixture	D^0 + anything	(59.5 ± 2.9) %
	J/ψ + anything	(1.16 ± 0.10) %
	e^- + anything	(10.86 ± 0.35) %
B^+	$\overline{D}^0 + \pi^+$	(0.480 ± 0.015) %
	$J/\psi + K^+$	(0.103 ± 0.003) %

Table 4: Selected bottom hadron decay channels and their branching ratios from PDG [43].

tion the decay vertices. These channels can access the low-p_T B-mesons which are sensitive to collisional energy loss mechanism in the QGP medium and b-quark hadronization. Table 4 lists branching ratios (B.R.) of these inclusive and exclusive decay channels. The MVTX can efficiently separate the B-meson decay signals from the background dominantly coming from the primary interaction vertex in heavy-ion collisions. It will become impossible to perform the following measurements at sPHENIX without MVTX.

In the following, we will discuss the B-meson signal significance in the non-prompt D^0 channel using the full GEANT4/tracking simulation + a fast Monte Carlo (MC) method. The simulation based on GEANT4 includes a proper description of the tracking reconstruction performances of sPHENIX with the MVTX plus the full DCA distributions of the charged tracks pointing to the primary vertex. These are fed into a fast MC simulation that can be conducted with sufficient statistics for both signal and background evaluations.

D^0 mesons are reconstructed through $K^-\pi^+$ decay channel with a branching ratio of 3.89%. The D^0 decay vertices are reconstructed topologically with kinematical variable selection to suppress the background contribution. In the following two sub-sections, we will present the physics performance from both inclusive non-prompt D^0 measurement as well as the exclusive D^0+π decay channel. Figure 25 illustrates their decay topology.

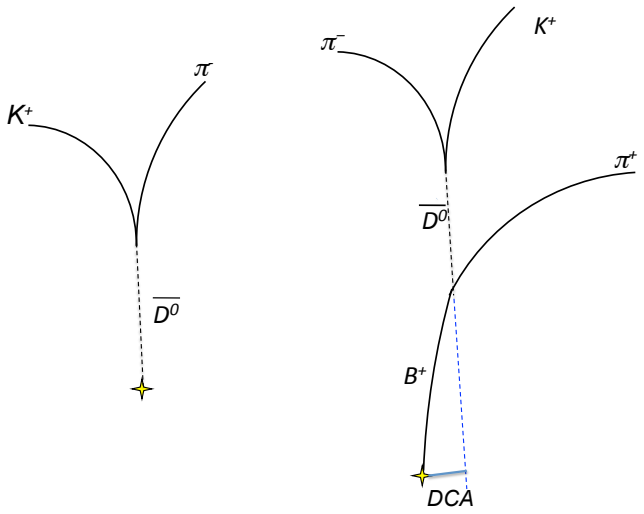

Figure 25: Topological sketch for several typical decay channels of charm (left) and bottom (right) hadrons. Yellow stars indicate primary collision vertices.

5.3.1 Inclusive non-prompt D^0

With the reconstructed D^0 decay position and its momentum, one can calculate the DCA distribution with respect to the reconstructed collision vertex. Non-prompt D^0 mesons from bottom hadron decays are expected to have a broader distribution compared to that of prompt D^0 mesons due to the boost of bottom decays. The left plot of Fig. 26 shows the D^0 3-D DCA distributions in the p_T range of 4–5 GeV/c for 24 billion 0–10% central Au+Au events. The narrow peak close to zero indicates the prompt D^0 signal from the primary collisions. The red distribution presents the signals from B-meson decays. The estimated background contribution is also shown in the same plot as the blue histograms.

The input prompt D^0 signal spectra are based on the existing RHIC measurement from STAR, while for non-prompt D^0 signals, we take the Fixed Order Next-to-Leading-Log (FONLL) calculation for open bottom hadron p_T spectra and fold in with a predicted $R_{\rm AA}$ based on theory model calculations. The combinatorial background in this simulation uses input from the HIJING generator. We also consider, to first order, the correlated background contribution underneath the D^0 mass peak by parameterizing the $p_{\rm T}$ dependence of the correlated background to D^0 signal ratio from the STAR HFT data. The full background underneath the D^0 mass peak with no $\rm DCA_{D^0}$ selection cut is considered as the background in both prompt D^0 and non-prompt D^0 reconstruction for a conservative estimate.

The prompt and non-prompt D^0 reconstruction have been fine tuned using the Toolkit for Multivariate Variable Analysis (TMVA) package. The Boosted-Decision-Tree (BDT) training method is used for selecting the best signal significance. The signal significance is calculated as $S/\sqrt{S+B}$ while S and B are the estimated signal and background counts.

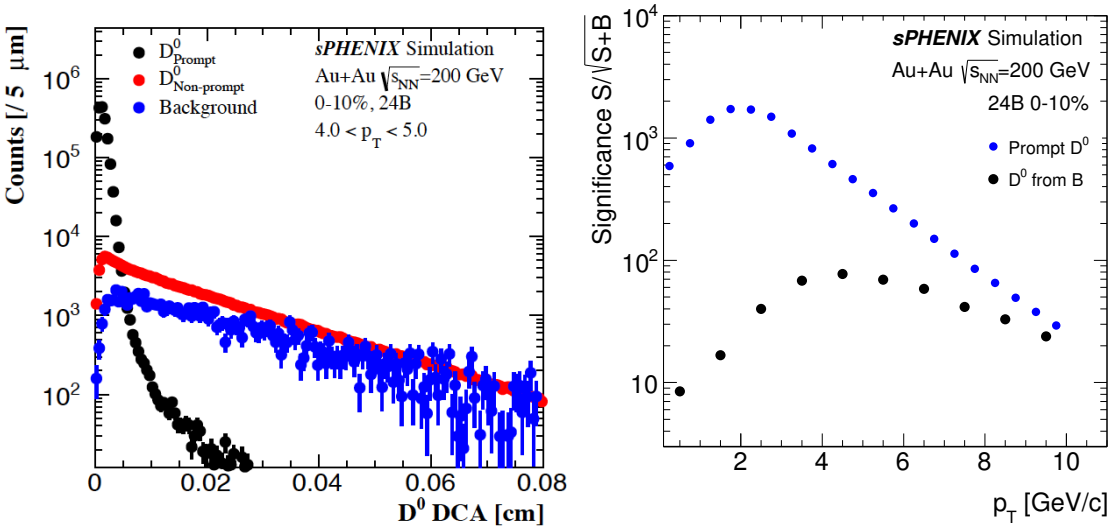

Figure 26: (Left) Simulated D^0 3-D DCA distributions for prompt (black), non-prompt (red) as well as background (blue) contributions for 24 billion 0-10% central Au+Au events. (Right) Estimated prompt and non-prompt D^0 significance as a function of p_T for 24 billion 0-10% central Au+Au collisions at $\sqrt{s_{NN}}$ = 200 GeV with the sPHENIX MVTX detector.

The right plot of Fig. 26 shows the estimated prompt and non-prompt D^0 significance as a function of p_T for 24 billion 0-10% central Au+Au collisions at $\sqrt{s_{NN}}$ = 200 GeV taken with the sPHENIX and MVTX detectors. The prompt D^0 production rate is taken from existing STAR measurements[6] and the B-meson production rate is based on the FONLL pQCD calculation in p+p collisions and scaled by the number of binary collisions, $N_{\rm coll}$, to central Au+Au collisions. The additional nuclear modification factor, $R_{\rm AA}$, for the input B-mesons is included by taking the input from the average values of several model predictions. The estimation shows good performance for B-meson tagging using the non-prompt D^0 over a wide p_T region. Please note that we don't include the projections below 2 GeV/c where the S/B is less than 100 and systematic uncertainties may be dominant.

We take the above significance estimation and convert it to the statistical uncertainties on the physics observables - nuclear modification factor $R_{\rm CP}$ and v_2. Figure 27 shows the statistical uncertainty estimation for $R_{\rm CP}$ (0–10%/60–80%) of prompt (blue dots) non-prompt (black dots) D^0 mesons for 240 billion Au+Au 200 GeV events. The center positions of the projected data points are placed on the average value of theory predictions from several models [2, 3, 5]. The plot clearly shows that one can separate the non-prompt D^0 $R_{\rm CP}$ from the prompt D^0 provided the suppression hierarchy predicted by theory calculations [2, 3, 4, 5] holds. In the right panel, the estimated data points with uncertainties are compared with these model predictions. sPHENIX MVTX detector with the requested datasets will provide strong constraints on various model predictions, and the projected data points will have sufficient precision to be able to differentiate between them.

Figure 28 left plot shows that statistical uncertainty projection for v_2 of prompt (blue dots) and non-prompt (black dots) D^0 mesons for 240 billion Au+Au 200 GeV events. One can clearly answer the question of whether bottom quarks flow with the medium or not. Such precision should allow further joint efforts between theorists to further constrain the heavy quark diffusion coefficient, the intrinsic transport parameter of the QGP. On the right plot, the projection is compared to a few theory model predictions [2, 4].

The performance described above has been focused on the inclusive non-prompt D^0 channel. Simulations have been pursued to continue exploring the B-meson tagging using non-prompt J/ψ's or further

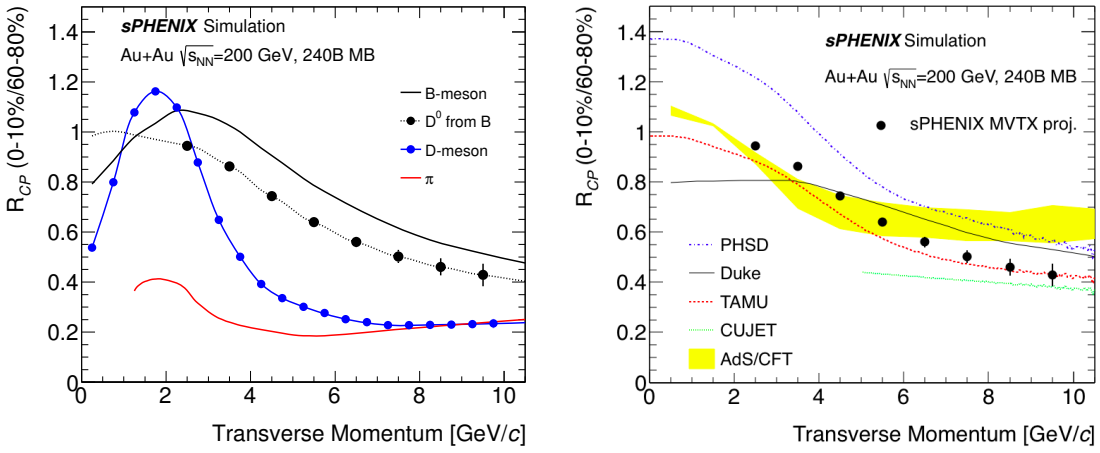

Figure 27: Statistical uncertainty estimation for $R_{\rm CP}$ of non-prompt D^0 measurements from 240 billion Au+Au 200 GeV events. In the left plot, the D-meson and B-meson curves are based on calculations from Duke, TAMU, PHSD, CUJET and Ads/CFT models for 0-10% $R_{\rm CP}$ [2, 3, 4, 5, 45, 46], and the dashed curve represents the non-prompt D^0 from B-meson decays. In the right plot, several model calculations shown for non-prompt D^0 (B decays).

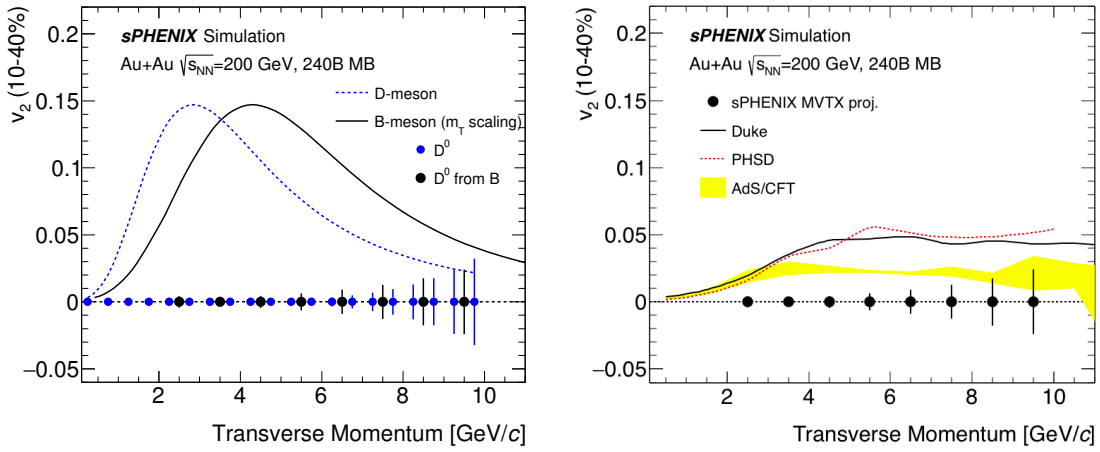

Figure 28: Statistical uncertainty estimation for v_2 (10–40%) of non-prompt D^0 measurements from 240 billion minimum bias Au+Au 200 GeV events. The D-meson curve is a fit to STAR recent D^0 v_2 data points [6] and the B-meson curve is calculated from the D-meson assuming m_T scaling. The blue and black data points with the vertical bars indicate the statistical uncertainty projections for both D-meson and non-prompt D^0 (B-meson decays) measurements. In the right plot, the projection is compared to several model calculations shown for non-prompt D^0 from B-meson decays.

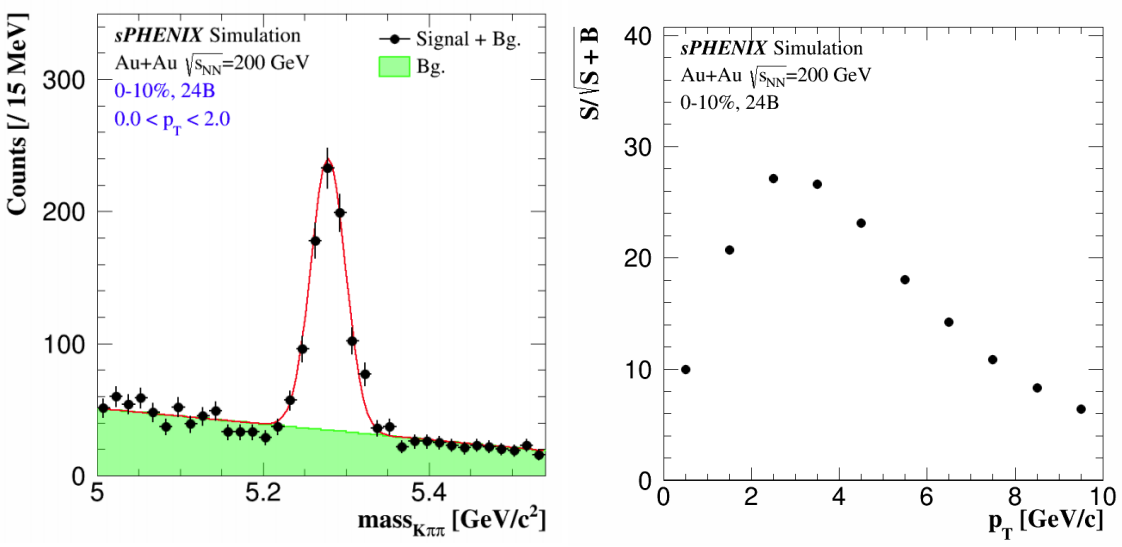

Figure 29: (Left) Estimated B^+ signal and background levels in $0< p_{\rm T} <2$ GeV/c and 24 billion 0–10% central Au+Au events at $\sqrt{s_{NN}} = 200$ GeV. (Right) Estimated B^+ signal significance as a function of p_T in the 0–10% central events from 240 billion minimum bias triggered Au+Au events at $\sqrt{s_{NN}} = 200$ GeV.

exclusive reconstruction of B-meson through hadronic decays.

5.3.2 Performance of full B-meson reconstruction through $B^+ \to \overline{D}^0 + \pi^+$

With the reconstructed D^0 mesons, by associating with another secondary charged pion track, one can try to reconstruct the B^+ meson decay vertices and their full decay kinematics. The topological requirement of cascading decay vertices places a strong rejecting power in removing random combinations.

We utilize the hybrid simulation, as described above for inclusive non-prompt D^0, and feed the the signal and HIJING background tracks into the fast MC simulation. The topological cuts have been fine tuned using the TMVA BDT method. Typical topological variables used in the tuning are single track DCA to primary vertex, D^0 candidate DCA to primary vertex, decay length of D^0 and B^+ candidates, D^0 and B^+ momentum pointing angle w.r.t their flight path etc.

The left panel of Fig. 29 shows the reconstructed B^+ signal based on the estimation of the signal and background through the topological reconstruction in $0< p_T <2$ GeV/c from 24 billion 0–10% central Au+Au events at $\sqrt{s_{NN}} = 200$ GeV. Partial reconstruction from B^+ multi-prong decay is not included in this simulation, but it has little impact on the background level underneath the B^+ mass peak. The right panel shows the estimated B^+ signal significance as a function of p_T in the 0–10% central events from 240 billion minimum bias triggered Au+Au events. The MVTX detector together with other tracking detectors in sPHENIX should be able to make this measurement over a broad momentum region in central Au+Au collisions.

With the estimated significance numbers, we plot the estimated uncertainties on the B^+ yield or cross section measurement as a function of p_T in central Au+Au collisions. The statistical uncertainty of p_T integrated B^+ total cross section can be better than 5%. Note that the fraction of the B^+ total cross section for $p_T > 1$ GeV/c and 2 GeV/c is about 90% and 67% respectively. The central value of the B^+ yield included here is the $N_{\rm coll}$ scaled FONLL calculation folded with predicted $R_{\rm AA}$ based on model calculations.

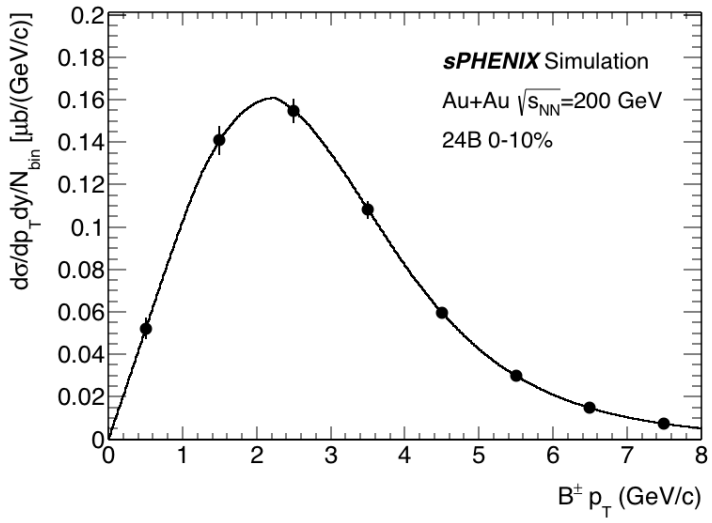

Figure 30: B^+ cross section measurement with estimated statistical uncertainties in 24 billion 0–10% central Au+Au events at $\sqrt{s_{NN}}$ = 200 GeV. The blue arrows indicate the fraction of integrated B^+ cross section with different p_T low end cuts.

6 Technical Scope and Deliverables

In this section, we summarize the technical scope and deliverables of the proposed MVTX project. The project scope comprises designing, building and assembly the three layer ALICE Pixel Detector (ALPIDE) MAPS-based pixel detectors.

6.1 High-level summary of key performance parameters and deliverables

MVTX key performance parameters and deliverables are summarized in the following tables:

High-level key performance parameters: instrument must be capable of:

Key Parameter	**Specs**
Pointing resolution of MVTX system (1GeV hadrons)	$\leq 50\mu m$
Single-track efficiency for MVTX system	$\geq 80\%$
Compatible with sPHENIX DAQ	15kHz average trigger rate

Table 5: MVTX high-level performance parameters

Low-level key performance parameters: experimentally demonstrated at project completion:

The MVTX project will be complete when all deliverables listed in Table 7 have been tested and installed in the sPHENIX detector at RHIC.

The offline software is not a project deliverable, but integrated with the project through sPHENIX collaboration.

Key Parameter	Specs
Thickness of stave layer	$\leq 0.5\% X_0$
MVTX chip internal alignment and stability	$\leq 30 \mu m$
Internal alignment MVTX and INTT	$\leq 500 \mu m$
MVTX integration time	$\leq 20 \mu S$
Live channels	$\geq 80\%$
MVTX readout speed and dead time	$\leq 5\%$ additional dead time @15kHz average trigger rate and simulated occupancy

Table 6: MVTX low-level performance parameters

Key element	Deliverable
1	MVTX mechanical support interface to sPHENIX global rail frame
2	3-layer MVTX detector: R coverage 23 - 40 mm, 270mm in Z 48 staves total, with each stave contains 9 ALPIDE sensor chips layer-0: 12 staves layer-1: 16 staves layer-2: 20 staves one FEM per stave, total 48 FEMs; 10 spare FEMs
3	6 backend PC, hosting 6 DAM boards; 2 spare DAM boards
4	Two clam shells, with 3 MVTX layers integrated and aligned on each clam shell
5	36 tested staves to serve as spares and replacement components to allow for any needed repairs to the existing sectors of the MVTX detector, including complete replacement of the two inner most layers (28 staves)
6	Low voltage, Bias Voltage, Cabling and Cooling
7	A PC-based control and monitoring system

Table 7: Summary of MVTX key deliverables.

6.2 MAPS chip and stave description

The proposed MVTX detector consists of 432 ALICE ALPIDE pixel sensors distributed in 3 layers. The basic detector readout unit is named a "stave", each stave contains 9 ALPIDE sensor chips. The MVTX requires a total of 48 staves.

The stave is the basic readout unit of the MVTX and is shown in Fig. 31. It utilizes the same design as the ALICE ITS IB upgrade, and consists of the following main components from bottom to top:

Hybrid Integrated Circuit (HIC): assembly consisting of the polyimide flexible printed circuit (FPC) on which the Pixel Chips and some passive components are bonded.

ALPIDE chip: a total of 9 chips per stave. Area covered by the chips: 15×271.2 mm^2, including a gap of 150 μm between adjacent chips.

Cold Plate: high-thermal conductivity carbon fiber sheet with embedded polyimide cooling pipes and carbon ply that embeds the cooling pipes.

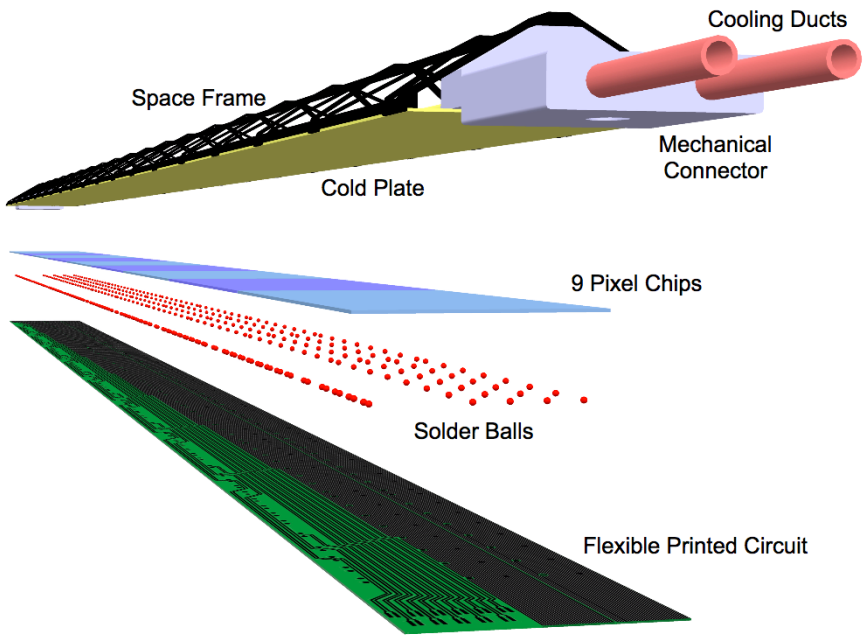

Figure 31: Schematic view of the MVTX Stave from ALICE ITS/IB design. In the final design change, the "Solder Balls" are replaced by "Wire Bondings".

Space Frame: truss-like lightweight mechanical support structure for the single stave based on composite material.

6.2.1 ALPIDE description

Each Stave consists of 9 ALPIDE chips. The ALPIDE chip is based on Monolithic Active Pixel Sensor technology and implemented in a 180 nm CMOS sensor [38, 47]. It has been designed for the ALICE ITS upgrade and will be used without modification for the sPHENIX MVTX detector. The active pixel region for the ALPIDE chip is 30mm (X direction) by 15mm (Y direction) which contains 1024×512 (X×Y) sensitive pixels (see Fig. 32). The dimension of each pixel is 29.24μm × 26.88 μm (X×Y). The pixel columns are counted from 0 to 1023 from left to right along the X axis, and the pixel rows are counted from 0 to 511 from the top to the bottom. The periphery circuit is located at the bottom of the chip within the 1.2×30 mm^2 region.

The readout block diagram is shown in Fig. 33 and the schematic is shown in Fig. 34. The collection n-well has an octagonal shape with 2 μm diameter and n-well to p-well spacing of 3 μm. In Fig. 34, diode D1 is the sensor p-n junction. The input node is continuously reset by diode D0. VRESETD establishes the reset voltage of the charge collecting node (pix_in). A particle hit will lower the potential at the pixel input pix_in by a few tens of mV. This will cause the source follower formed by M1 and the current source M0 to force the source node to follow this voltage excursion and dump charge associated with the voltage change and the capacitance of the source node onto the analog output node pix_out[47]. The charge threshold of the pixel is defined by ITHR, VCASN and IDB. The effective charge threshold is increased by increasing ITHR or IDB. It is decreased by augmenting VCASN. Voltage bias VCLIP controls the gate of the clipping

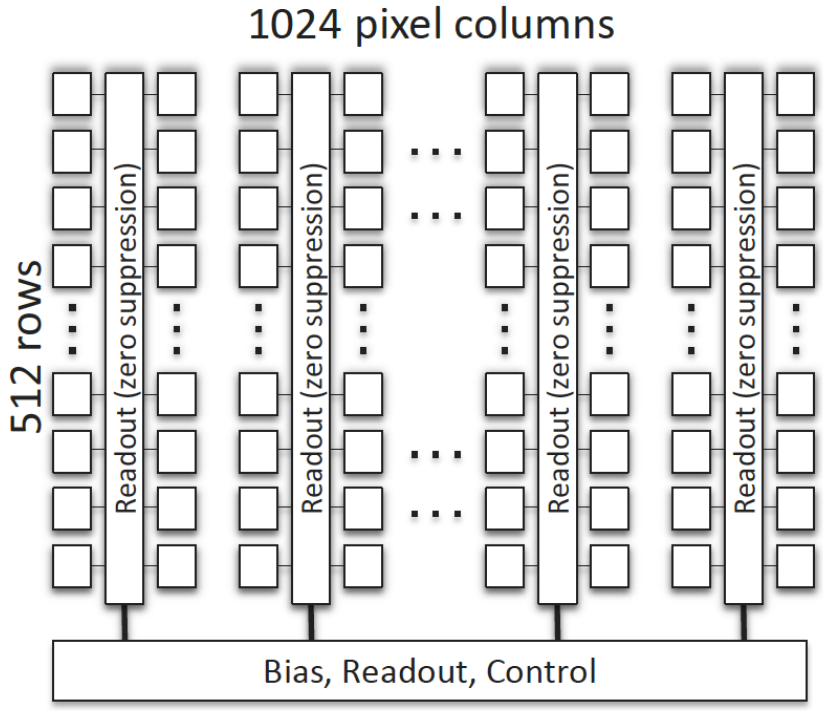

Figure 32: The ALPIDE chip architecture.

transistor M6. The lower VCLIP, the sooner the clipping will set in.

The front-end also acts as an analogue delay line. The output of the ALPIDE front-end has a peaking time of around 2 μs within the typical 5 μs duration. This allows operation of the chip in triggered mode when the latency of the incoming trigger is comparable with the front-end peaking time. A common threshold is applied to all pixels. The latching of the discriminated hit is controlled by global STROBE pulse. The STROBE pulse can be generated from either an external trigger or internal trigger, the duration of the STROBE is programmable. Each pixel contains a pulse injection capacitor for the test charge injection in the input of the front-end. A digital-only pulsing mode can be selected to write the logical signal in the pixel memory cells. The pulsing pattern is programmable. The readout of the pixel matrix is based a Priority Encoder. The transfer of the matrix data to the periphery circuit is zero-suppressed. The operation voltages are summarized in Table 8.

The data from the 32 region readout blocks are assembled and formatted by a Top Readout Unit module. There are two readout modes: one is for the "Triggered" mode, the other is for the "Continuous" mode. The "Triggered" mode allows the strobe generation and readout to be triggered externally. The "Continuous" mode allows the frames to be continuously integrated and readout with programmable strobe duration.

The core functionality is to store the internal state of the front-end discriminators within each pixel and transmit this information off chip. Each pixel in the ALPIDE matrix has 3 in-pixel data storage elements (buffer). The Multi Event Buffer (MEB) enables the storage of 3 complete frames without the completion of a matrix readout or any data loss.

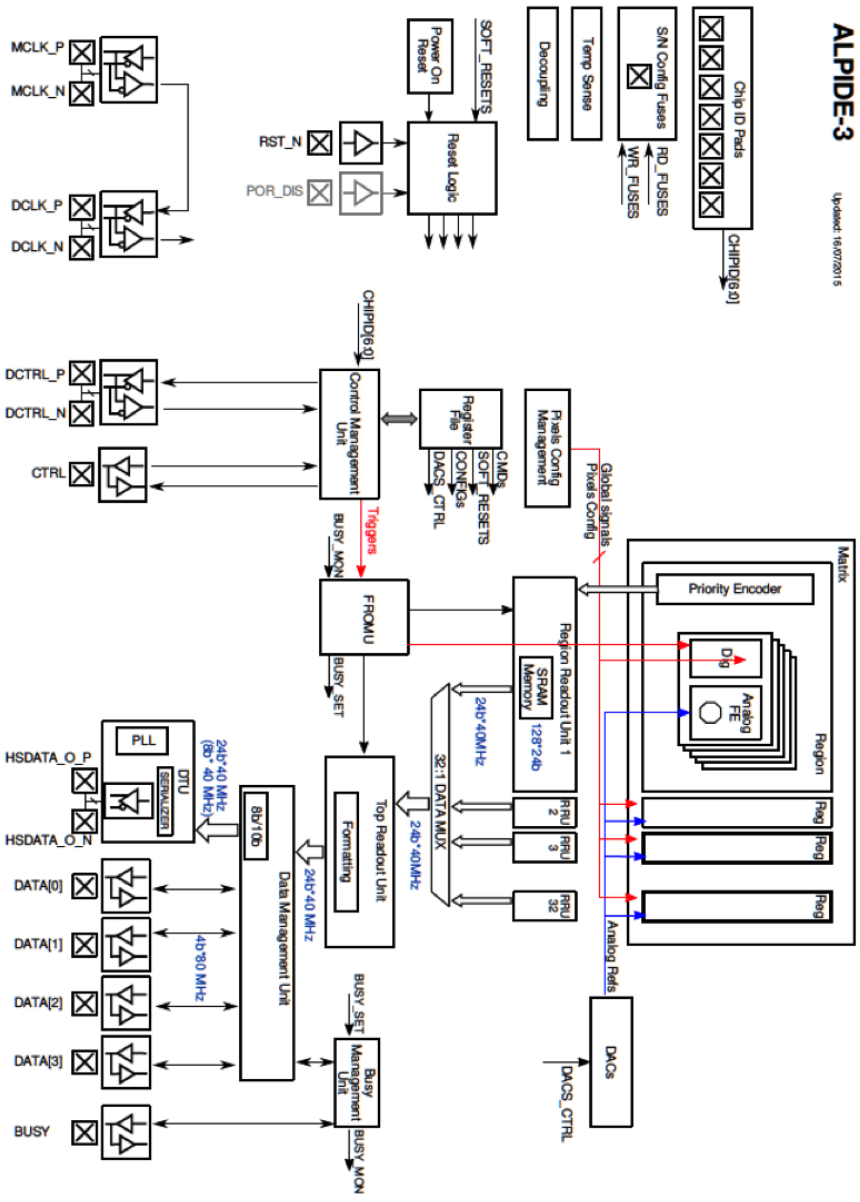

Figure 33: The ALPIDE chip readout block diagram.

6.2.2 Interfaces

The ALPIDE chip has custom control interfaces for configuration and trigger. The control interfaces used in MVTX are the same as are used in the IB of the ALICE ITS upgrade. The interface supports the interconnection of multiple chips on a multi-point control bus. The nine chips on the stave are directly connected to a shared differential bidirectional 40 Mbps control line using the DCTRL port, and a shared differential 40 MHz clock line using the DCLK port. The DCTRL and DCLK differential ports are implemented with a custom designed differential transceiver cell, which implements the M-LVDS standard as

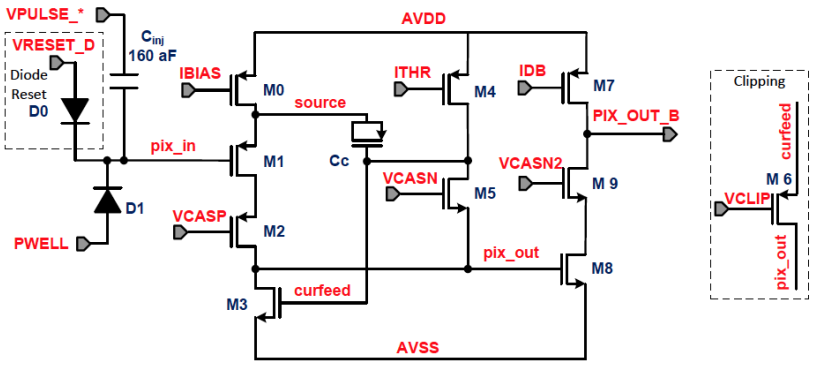

Figure 34: The ALPIDE front end schematics.

	Minimum value	Default value	Maximum value
AVSS (Analog ground)	0 (V)	0 (V)	0 (V)
AVDD (Analog supply)	1.62 (V)	1.8 (V)	1.98 (V)
DVSS (Analog ground)	0 (V)	0 (V)	0 (V)
DVDD (Analog supply)	1.62 (V)	1.8 (V)	1.98 (V)
PWELL (Bias Voltage)	-6 (V)	TBD	0 (V)
SUB (Bias Voltage)	-6 (V)	TBD	0 (V)

Table 8: The operation voltage for the MVTX chip/stave.

defined in TIA/EIA-899. The Control Management Unit block implements the control layer and provides full access to the control and status registers of the chip. The supported transaction types are shown in Fig. 35.

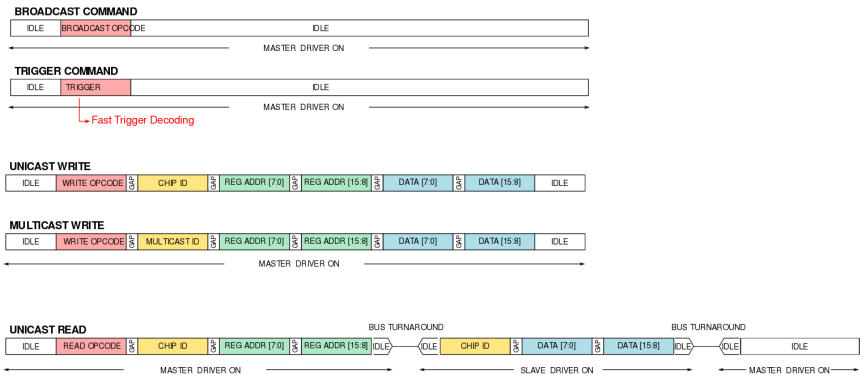

Figure 35: Format of control transactions on the ALPIDE control bus.

All the analog signals are generated by a set of on-chip 8 bit DACs. The analog section of the periphery also contains an ADC with 10-bit dynamic range, a band gap voltage reference and a temperature sensing circuit. The ADC can used to monitor the outputs of the DACs, the analog and digital supply voltages, the

band gap voltage, and the temperature.

The Data Transmission Unit (DTU) provides a fast serial link for the transmission of the data from the ALPIDE. The data is transmitted over a differential serial line to the off-detector electronics. The data stream is transmitted over an aluminum over kapton FPC with a maximum length of 300 mm and then to a micro-twinaxial cable over a length of 5 m. Each ALPIDE chip has a single dedicated serial line. The baseline option for the data transmission speed is 1.2 Gbps, but reduced readout speeds of 600 Mbps or 400 Mbps can be used if the cable attenuation at high frequencies prevents 1.2 Gbps readout.

6.3 MAPS chips/stave production

We have reached an agreement with the ALICE ITS Upgrade Project management to produce the necessary ∼1000 ALPIDE MAPS chips for the sPHENIX MVTX. These chips will be produced by Tower Jazz as part of the ALICE ITS upgrade project. The complete QA of the produced MAPS chips will be carried out by the Korean collaborators led by Yonsei University. sPHENIX stave mechanical carbon frames and connectors, which are identical to the ALICE ITS Upgrade IB detectors, will be fabricated and tested using the ALICE ITS Upgrade facilities at CERN. The sPHENIX collaboration will provide additional manpower, including students, postdocs and technicians, to help with the stave assembly, mechanical survey and full stave readout testing in the CERN ITS/IB upgrade labs. The sPHENIX project will eventually obtain 84 fully tested staves from ALICE (which includes 36 spares) and assemble the final detector in the U.S., using the existing facilities at LBNL used for the ALICE ITS mid-layer upgrade project.

6.4 MAPS stave assembly and testing

Following the completion of the ALICE ITS IB assembly, experienced CERN techs will continue working on stave assembly for the sPHENIX MVTX project, using the same automated chip mounting machines at ALICE ITS IB assembly labs. Students and postdocs from the sPHENIX collaboration will work with CERN techs to perform the QA of the assembled staves, including visual inspection, test the stave readout at full speed on the test bench, analyze test data to quantify the quality and performance of the staves and produce QA traveler for each stave. Fully tested staves will be sent to LBNL to make half barrel detectors.

6.5 Readout integration and testing

As shown in Fig. 36. The DAQ electronics take the data from the stave assemblies to the sPHENIX DAQ System. The data flow goes from the stave assembly through a copper cable to the Front end Module FEM which is based on the ALICE Readout Unit (from ALICE) (RU) hardware. The FEM will be located inside the experimental hall and just outside the magnet approximately 5 meters from the staves. The FEM will send the data using CERN Versatile Link which consists of radiation tolerant Gigabit Transceiver chips GBT that drive radiation tolerant fiber optic links to the Data Aggregation Module (DAM). The Data Aggregation Module (DAM) is based on the ATLAS Front End Link eXchange (from ATLAS) (FELIX) hardware [48] and is housed in the Event Buffering Data Compressor (EBDC) server chassis (standard LINUX PC) located in the sPHENIX rack room. The DAM will readout eight FEMs, aggregate the data and perform sub-event packaging. The data is transmitted to the EBDC over Peripheral Component Interconnect Express bus (PCIe).

The control flow will be handled by the FEM and DAM. The FEM will receive trigger, timing, control logic, and calibration commands from the DAM and distributes them to the sensor stave. The FEM will also control and monitor the power unit which provides power to the stave assemblies. The monitored data will be sent to the DAM.

6.5.1 Front End Module

As shown in Fig. 37 and Fig. 38, the Front End Module (FEM) is an FPGA-based data processing system designed to exploit the CERN Versatile Link hardware with three (GBT)-based fiber optic transmitters for

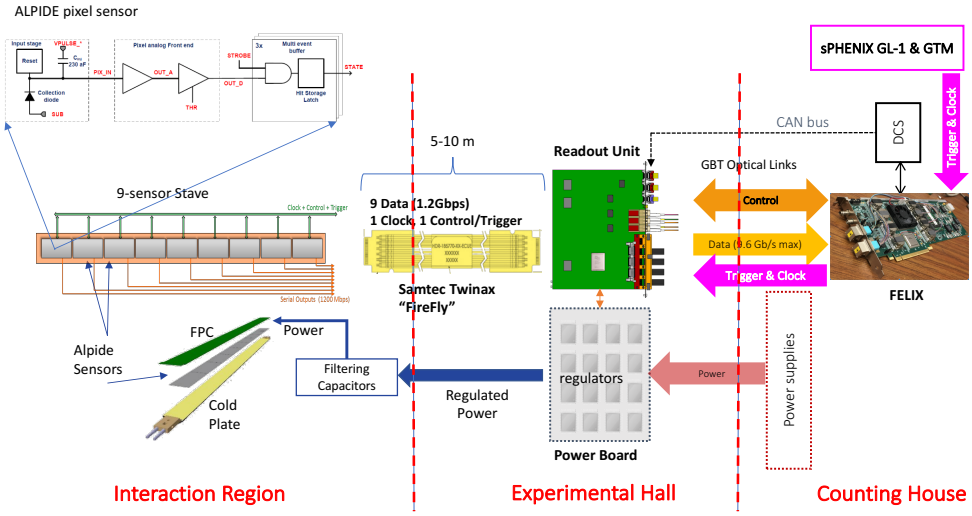

Figure 36: MVTX readout chain in sPHENIX. FEMs are located about 5m from the MVTX, ALPIDE data are sent from FEMs to DAMs in the Counting House through high-speed fiber optic links.

data/status transmission and two GBT-based fiber receivers for timing/trigger and control input. There is one FEM necessary for reading data from each stave. Control data and trigger for the stave is transmitted over one of the copper twinax pairs in the stave "firefly" cable. The clock for the sensor stave is also transmitted over one of the copper twinax pairs. The FEM input consists of 9 independent 1.2 Gbit/sec data streams, one from each of the ALPIDE chips on the stave. The FEM combines the 9 independent Gigabit data streams, appends a header and trailer for each trigger event, and transmits the data to the DAM via GBT-based fiber links. The GBT-based data links on the FEM use radiation hardened integrated circuits. In addition, the FEM hardware is designed to detect and mitigate radiation upsets. The main logic is triplicated and verified with an auxiliary FPGA, in the event there is a mismatch in the triplication output the auxiliary FPGA re-programs the main FPGA. Trigger and timing data for the FEM comes from the DAM via one of the radiation hardened GBT-based fiber receivers. The FEM slow control information is received on another GBT-based fiber receiver. The FEM also has a control interface to the power board. The MVTX system will consist of 48 FEM boards.

As shown in Fig. 38, the Versatile Link optical link system designed to carry data, triggering and slow control signal in radiation environments over a single, bi-directional optical link driven by the GBT ASIC. The electronic component hosted in the FEM of the link has been designed by CERN to operate in high-radiation environment, ensuring resistance to both total dose and single event effects. The counting room side electronic relies instead on commercial optical transceiver and FPGA hardware implementing the GBT protocol necessary to communicate through the link. The FEM connects directly to the GBTx chip [GBTx] through its e-link interfaces, a programmable set of bi-directional data and clock lines. Each e-link comprises three links: a transmit line, a receive line, and a dedicated clock line. A single GBTx chip handles up to 40 e-links on the front-end side and a bidirectional optical link toward the counting room.

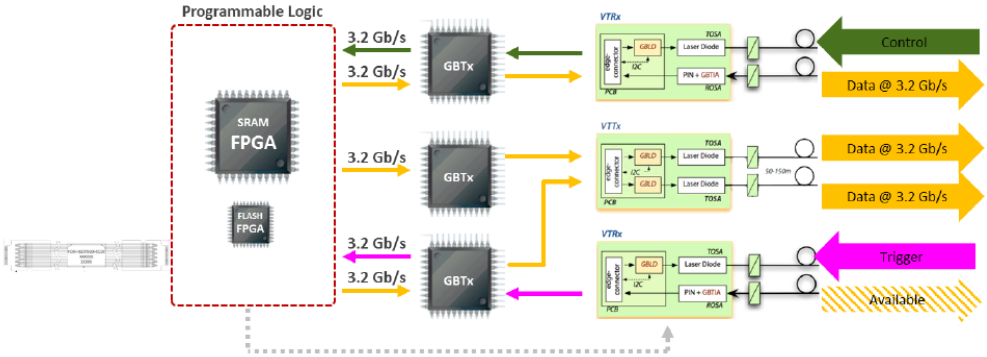

Figure 37: FEMs Block Diagram

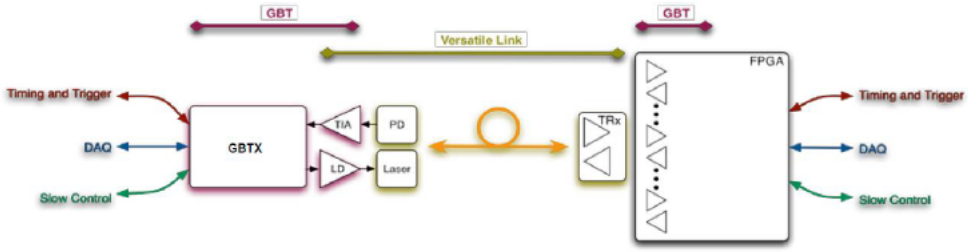

Figure 38: FEMs Versatile Link GBT Block Diagram, FEM in the hall on the left, DAMs in counting room on the right.

6.5.2 Data Aggregation Module

As shown in Fig. 39, the DAM is an FPGA-based data processing system with 48 fiber receive channels, 48 fiber transmit channels, 16 lane Gen3 PCIe and a timing/triggering FMC site to interface to the sPHENIX timing system. The timing and triggering information will come through the sPHENIX timing interface card on the FMC site. Slow controls interface will come through the PCIe interface from the Ethernet interface of the EBDC. The data processing related FPGA functionality includes data aggregation, data formatting and DAQ infrastructure generation for creating sub-event packages for transmission through PCIe interface to the EBDC. Busy signal generation is also determined in the DAM firmware. FEM timing and triggering data is formatted in the DAM FPGA and transmitted to the FEM via the DAM fiber control links. Slow controls status data is separated from the FEM data within the DAM and formatted for transmission back to the control system. Control data is formatted and distributed to associated FEMs via the DAM fiber control links. The MVTX system will consist of six DAM boards.

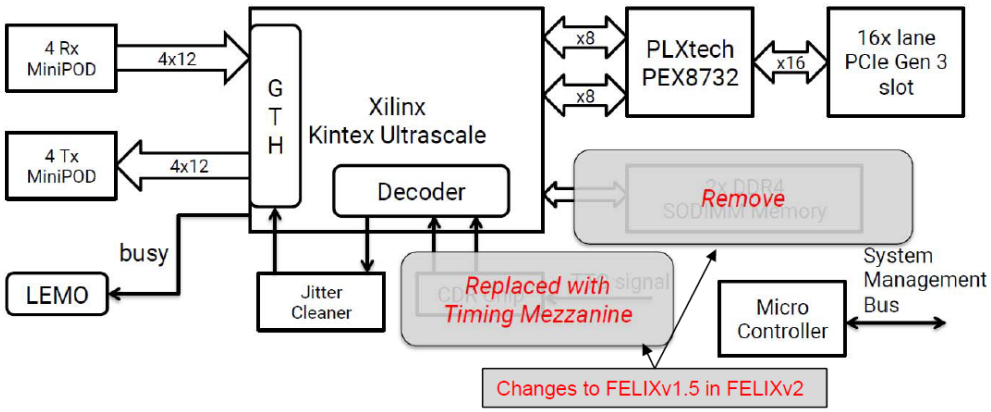

Figure 39: DAMs Block Diagram. Red boxes highlights the change in the coming version of DAMs v2 pre-production card: adding a Timing Mezzanine card, which will be used for interfacing to the sPHENIX timing system, and removing a memory interface which is not used by MVTX.

6.6 Power System

The design and production of power unit for the sPHENIX MVTX full readout chain will be delivered by LBNL. LBNL is currently developing the power system for the ALICE ITS Upgrade. The same power unit and distribution boards will be used by the MVTX. The prototypes are currently being tested at both LBNL and LANL. Figure 40 shows the current status of the power unit and the ALPIDE a single ALPIDE chip communication test at LANL. The communication is carried out by the MOSAIC readout board which has similar communication functionality as the FEMs. The power unit and its distribution boards meets the requirements of the MVTX detector and its flexible design can be easily adapted to further needs. A brief description of requirements, architecture and main components is shown in this section.

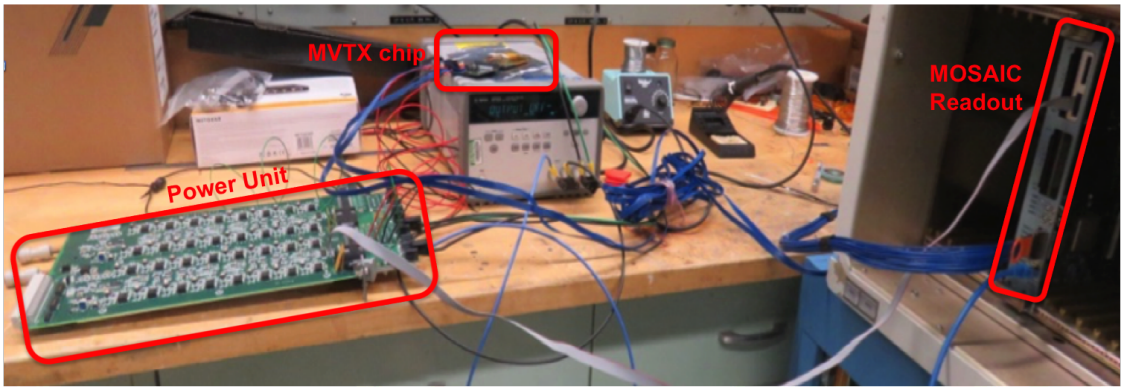

Figure 40: Communication test between the Power Unit and the MAPS ALPIDE chip through the MOSAIC readout module.

6.6.1 Power system requirements

The power system (PS) is closely inter-dependent with the sensor and module requirements, and with the detector environmental and operating conditions. These are most succinctly expressed as:

- Supply power (sensor supply and bias) to the staves.
- Meet the power requirements of the stave and FEM electronics.
- Tolerate the radiation environment at the power board location.
- Interface to the FEM board for control of PS functions and readout of parameters.
- Fit into the space allocated in the vertex detector integration envelopes.

This design will be tested in the development of the staves for the ALICE ITS Upgrade and optimized for sPHENIX. The desirable functional attributes for system include:

- Overcurrent protection for each power channel
- Remote current readout for each power channel

- Remote voltage readout for each power channel
- Remote voltage setting capability for each channel

6.6.2 Power system architecture

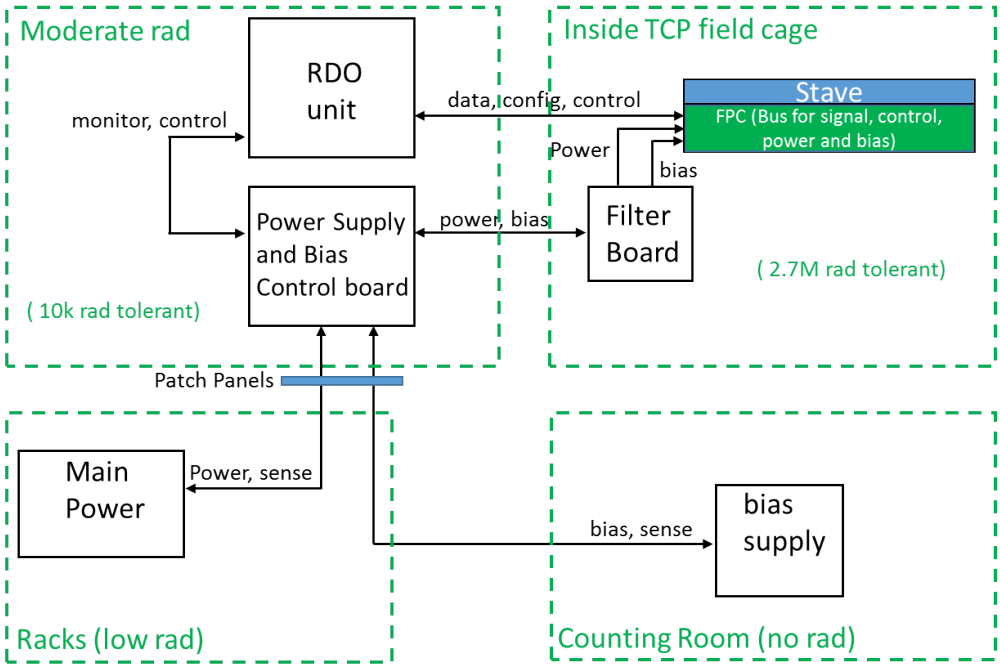

Figure 41: Basic Structure of the sPHENIX MVTX power system. Note the expected radiation load for each architecture block

A block diagram of the power system is shown in Fig. 41. The main power supplies are CAEN mainframes populated with A3009/A3009HPB radiation tolerant CAEN power modules located in the racks in the hall. The back bias power supplies are CAEN mainframes populated with A2518 CAEN power modules located in the sPHENIX Counting House (or in the low radiation area in the experimental hall).

The power supply and control board (PSCB) are being developed for the ALICE ITS Upgrade. They will contain power regulators, shunt resistors, over-current protection circuitry, current and voltage measuring circuitry and remote voltage setting circuitry which will be controlled by the FEM. The PSCB boards will be located adjacent to the FEM crates at a larger radial distance and in a lower radiation. The PSCB boards will provide capacitive filtering and regulated supply voltage to the power bus of the sensor modules. This architecture is shown in Fig. 42).

A ground plan is being developed in coordination with sPHENIX. The ground plan will electrically isolates the individual subsystems from each other except for the connection to the sPHENIX ground. The MVTX will use a star grounding plan, with a single point connection to the sPHENIX ground to minimize the possibility of introducing noise due to ground loops. Power returns will be isolated from each other and referenced to the sPHENIX ground. The mechanical structure will be electrically isolated from the electronics, and referenced to the sPHENIX ground.

6.7 Mechanical carbon structures

A description of the carbon fiber mechanical structures for the sPHENIX MVTX detector is provided in this section. The mechanical structures developed for the ALICE ITS IB are compatible with the gen-

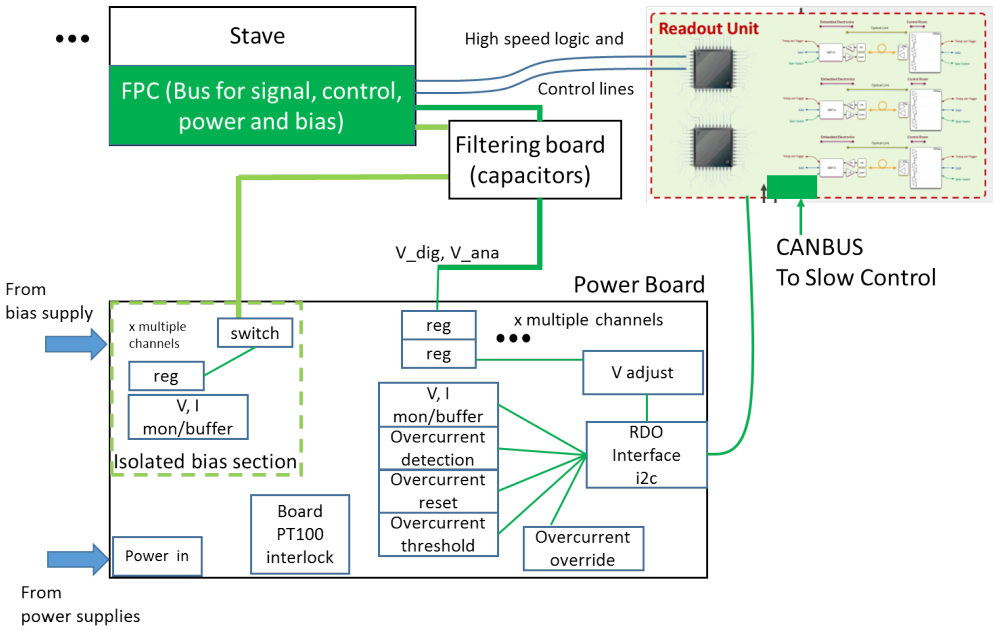

Figure 42: Basic architecture of the power board

eral sPHENIX detector infrastructure and constraints with small modifications. In this proposal, the ITS Upgrade mechanics design will be used as the baseline for the MVTX detector mechanics. The design will be reviewed and adapted at LANL, with the detector and service support carbon fiber structures will be fabricated at LBNL.

After discussing the requirements in Sec. 6.7.1, the mechanical structure that supports the staves in layers is illustrated in Sec. 6.7.2, while Sec. 6.7.3 describes the cable routing to the staves through the service barrels.

6.7.1 General requirements

The layout of the MVTX detector mechanical structure has been developed to fulfill the following design criteria:

- minimize material in the sensitive region;
- ensure high accuracy in the relative position of the detector sensors;
- provide an accurate position of the detector with respect to the TPC, INTT and the beam pipe;
- locate the first detector layer at a minimum distance to the beam pipe wall;
- ensure structure thermo-mechanical stability in time;
- facilitate accessibility for maintenance and inspection;
- facilitate assembly and disassembly of the detector layers and staves.

The main mechanical support structure of the MVTX detector has the shape of a barrel that flares out via a conical section to a service and support section. It holds in position the three detector layers. The

barrel is divided into two halves, top and bottom, which are mounted separately around the beam pipe. The barrel is composed of a detector section and a service support section. The staves are housed in the detector barrel-section and are connected via electrical signal connections, power cables and cooling lines to patch panels. The patch panels in the conical regions are located immediately outside of the TPC acceptance. The service and supporting sections integrate to these patch panels and support the signal and power cables through their routes from the detector staves to a second set of patch panels. Pipes that connect the vertex on-detector cooling system to the cooling plant in the sPHENIX hall are also routed through the service and support section.

6.7.2 Detector support structure

The main structural components of the detector barrels are the end-wheels and the Cylindrical and Conical Structural Shells (CCSS).

The end-wheels, which are light composite end-rings, ensure the precise positioning of the staves in a layer using precision ruby spheres and ruby pads. They provide the reference plane for fixing the two extremities of each stave. Staves are positioned on the reference plane by two connectors that engage with these locating ruby spheres fixed in the end-wheels. The stave position is then frozen by a bolt that passes through the end-wheels and is screwed inside the connectors. This system ensures accurate positioning, within 10 microns, during the assembly and provides the possibility to dismount and reposition the stave with the same accuracy in case of maintenance. The end-wheels on the front side allow for the services to interconnect with a patch panel in the conical region of the detector section. The different layers are connected together to form the half-barrel assembly. An outer cylindrical structural shell (CYSS) connects the opposite end-wheels of the three detector barrels and avoids possible external loads being transferred directly to the staves (see Fig. 43).

In order to minimize the material budget in the detection area and to facilitate installation and removal, the barrel is conceived as a cantilever structure supported off the conical end. A full scale prototype is being developed to verify the production process and the assembly procedure.

6.7.3 Service support structure

The service support structure design will be adapted from the ITS Upgrade Conical Support Shell (COSS) (see Fig. 44) to integrate with the sPHENIX TPC, INTT and general detector dimensions. The services attached to the detector barrel must be inserted or retracted together with the detectors.

All services, including cooling pipes, power, and signal cables, will be integrated into the service, support barrel, which is an extension of the detector barrel. Power cables will be grouped with the cooling tubes in the service barrel in order to remove the heat generated in the detector section. The services layout will follow the detector modularity. The services will be grouped per detector half-barrel and routed from the detector to a patch panel located in an accessible area at the end of service support section.

The assembly composed of half detector barrel and half service barrel is inserted or extracted from the TPC bore by means of two sets of lateral rollers fixed on the two half-detector assemblies and sliding on their corresponding rails provided by the cage assembly.

The service, support section itself is a light composite structure that has to provide both structural stiffness and dimensional stability, to guarantee a precise installation of the MVTX detector inside the TPC.

MIT and LANL will be working on the integration of the MVTX into the current sPHENIX detector design at BNL. This work will be in collaboration with the other sPHENIX detector groups including the INTT, TPC, and Minimum Bias Detector (MBD) groups, to ensure that choices made early in the design cycles will integrate smoothly with their detectors and other systems in the spectrometer. The support system designed in the ALICE version of this detector is cantilevered in a support cage, a similar yet smaller version

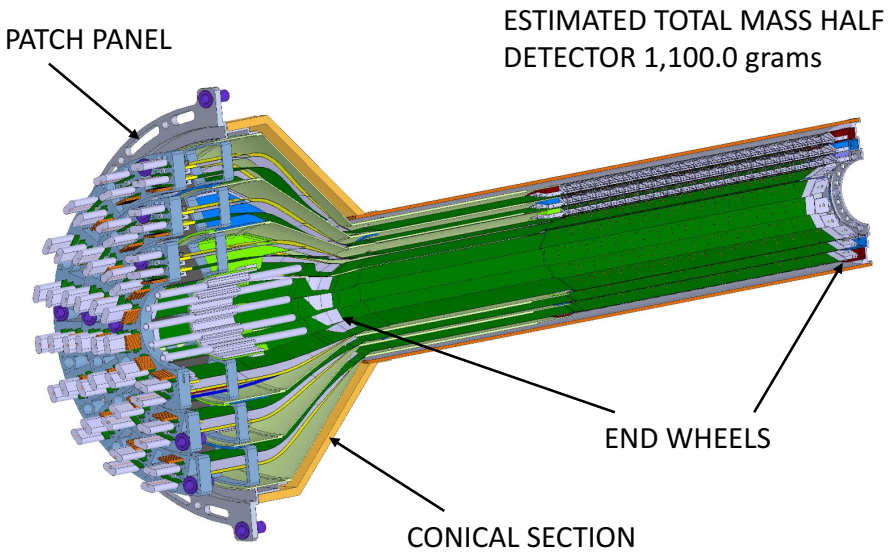

Figure 43: MVTX Half-Barrel, with the three half-layers fixed to the end-wheels. The layout shown here is based on the ALICE ITS IB design, but with extended cylindrical section for the INTT integration outside of the MVTX barrel.

of this will be a part of the MVTX integration proposal. This will allow more flexibility in a cage support design for the MVTX. The service and support section for each half detector assembly will require a new design for the services patch panels to allow for the interface of cables, cooling lines as well as dry air supply to the detector. These will also have to make accommodations for positioning and alignment of the detector as well as adequate fiducials to allow for final survey.

MIT and LANL will work with the carbon composite group at LBNL, as well as the group at CERN producing the stave assemblies and CCSS components for the ALICE ITS, in order to accomplish all of these goals. An extensive testing plan will need to be put in place to ensure that the final assembly will function as required. MIT will lead the design of the cooling system for the detector section stave assemblies. The current plan is to use a negative pressure water cooling system. This will be similar to the system being designed for the ALICE ITS, adapted for the MVTX configuration. This design is being considered so that if any unforeseen leak develops in the system, water will not drip on to other detector components and possibly damage them. MIT will use CFD analysis to ensure that the cooling system will be adequate to remove the small heat load produced for the stave assemblies. Figure 44 shows the proposed integrated mechanical support system for the ALICE ITS inner tracking system that will be adopted for the MVTX detector.

6.8 Mechanical integration

MIT will be leading the design and integration of the MVTX detector into the sPHENIX assembly. As a part of the MVTX system there are multiple cables, water and air cooling tubes that will need to be run from the detector barrel out to electronics and cooling plants external to the sPHENIX magnet. The type and

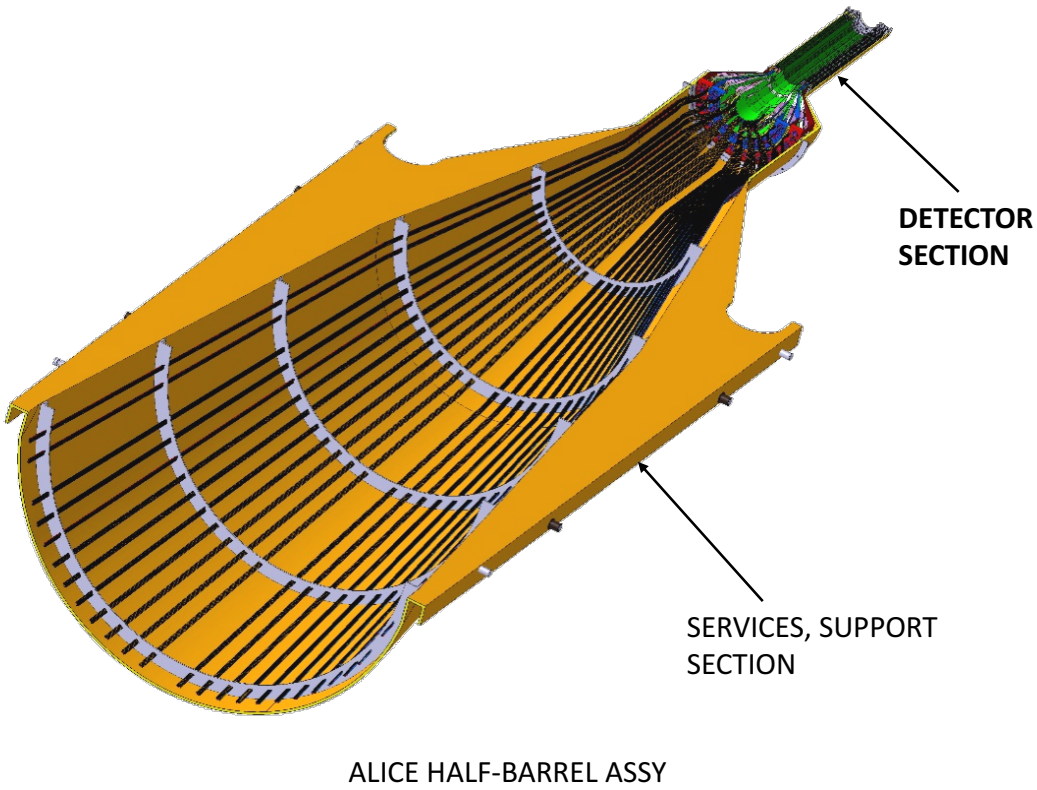

Figure 44: The service barrel is an extension of the detector barrel and integrates all services, including cooling pipes, power, and signal cables. The layout shown here is based on the ALICE ITS Upgrade IB design. It will be adapted to match the sPHENIX TPC and general detector dimensions.

number of these services has already been decided for the inner tracker of the ALICE ITS upgrade detector and will be duplicated for the MVTX. MIT will be responsible for verifying that these services meet safety and design needs compatible with BNL requirements. Coordination of fabrication at the composite shop at LBNL, for the fabrication of carbon, as well as electronics development at LANL and overall sPHENIX system engineering at BNL will be incorporated in the overall design for the MVTX integration by the MIT group.

It is required that the MVTX detector assembly be constructed in two halves in order for it to be translated into the inner bore of the TPC detector, as well as allowing it to pass over a flange on the beryllium beam-pipe assembly prior to reaching its final run location about the interaction point. This is achieved by using a similar engineered design for the installation of the inner tracker for ALICE by means of a cage that incorporates slotted rails that each half of the detector ride in towards their final position when they close together just prior to reaching its operating location. The cage and service section will be part of the MIT groups responsibility, a view of this design for ALICE is shown in Fig. 45.

Survey of the detector will require adequate fiducials and survey targets that can be used both during the MVTX half barrel assemblies as well as the location of the detector inside sPHENIX at its operating

position. Additional survey features will be incorporated on the installation cage to verify its compatibility with the sPHENIX assembly. This will be coordinated by the MIT group.

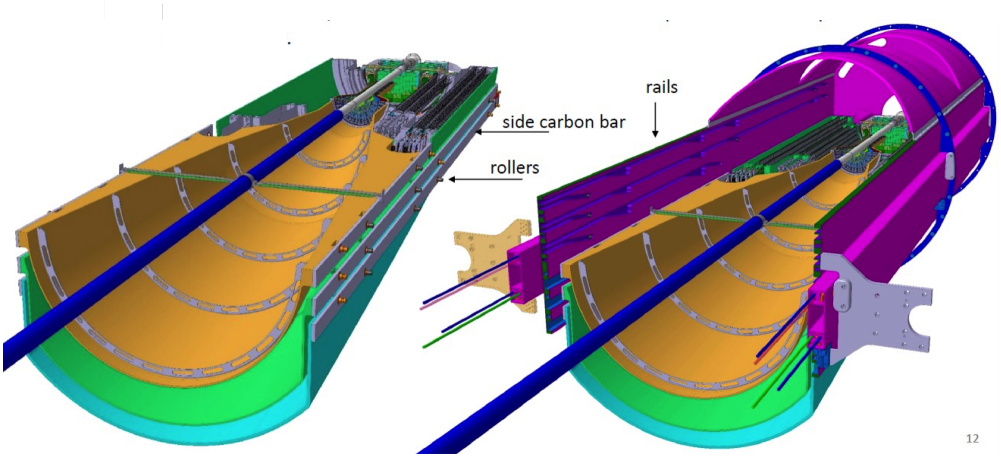

Figure 45: Basic structure of the ALICE ITS Vertex Detector mechanical supporting system.

6.8.1 Mechanical integration issues

As we examine in more detail how the MVTX will be supported, aligned, and serviced, it has become clear that it is critical to coordinate efforts to address these mechanical issues with similar efforts for the INTT. This is because the two detectors will be very close together in the final sPHENIX configuration and it will be a challenge to avoid space conflicts and other related problems. There may in fact be significant advantages (such as precise relative alignment) to viewing the INTT and MVTX as parts of the same detector component, with a common support structure.

Recently, sPHENIX project has created a new Office of System Integration to handle the coordination between all subsystems, including the MVTX with the INTT, TPC and MBD (Minimum Bias Detectors). In any event, it seems critical that the MVTX and INTT mechanical support efforts be closely coordinated and continue through the entire design of the support infrastructure. We understand that it is expected that the TPC, INTT, and MVTX will be supported by different project funds, so it will likely not be trivial to accomplish this coordination. However, it is necessary if the sPHENIX project is to succeed.

6.9 Detector assembly

The scope of participation of LBNL in the MVTX detector includes also the assembly of the staves into the half detector support structure. The three layers, starting from the outermost one, consist of 20, 16 and 12 staves, respectively. The stave assembly will be fabricated and tested at CERN, as described in Sec. 6.4, and shipped to LBNL. The assembly scope of work will consist of:

1. Inspection, functional testing and validation of received staves
2. Metrology survey of the staves
3. Mounting of the staves onto the end-wheels to form the layers
4. Functional testing and validation of the layers
5. Metrology survey on the layers

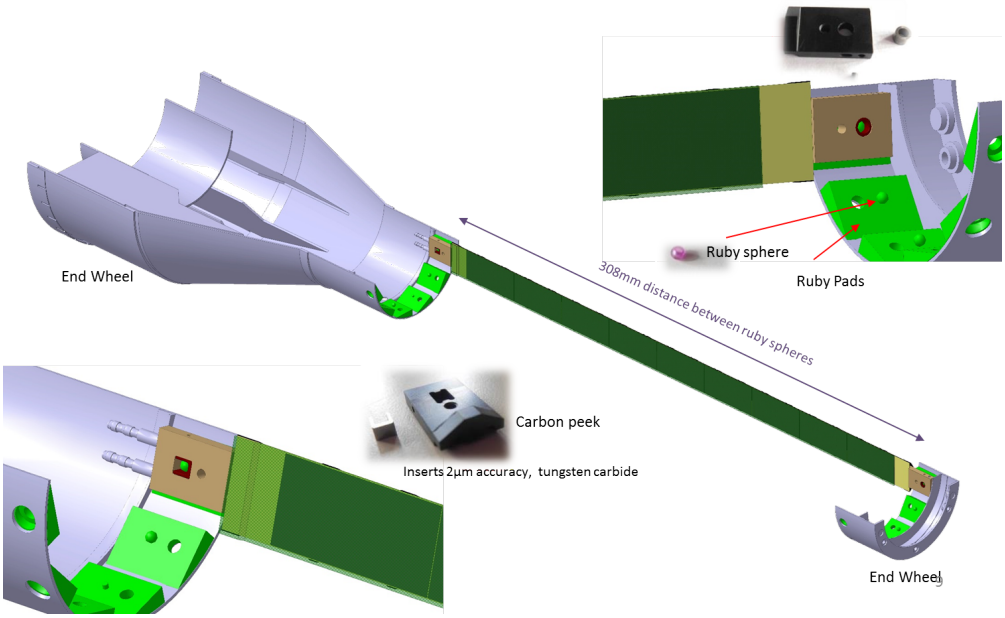

Figure 46: ALICE ITS stave assembly into layer. We will follow the same procedure for the MVTX detectors.

6. Assembly of the three layers together and to the cylindrical support into the half detector
7. Functional testing and validation of the assemblies
8. Metrology survey on the final assemblies
9. Packing and shipment of the final assemblies to BNL.

A testing system is being developed by the ALICE Collaboration and is based on the ALICE MOSAIC system. After the initial test, the stave is positioned on the end wheels reference planes by connectors at both extremities that engage a ruby sphere (part of an alignment system) fixed in the reference plane (see Fig. 46). The stave position is then fixed by a bolt. The front side end-wheel includes the service barrel conical extension to hold and route all services, including cooling pipes, power, and signal cables via a patch panel. The three layers are assembled together and to the half detector CYSS, and the relative position is achieved by reference pins (see Fig. 47).

After each assembly step the half-detector assemblies are tested for validation and reworked if necessary, and a metrology survey is performed. The half detectors are finally ready to be packed and shipped to BNL, where they will be integrated with the large service and support sections that will eventually be mounted into the installation cage for final positioning around the beam pipe in sPHENIX.

6.10 Online software, DAQ and Trigger

The online software for the MVTX will be part of the sPHENIX DAQ. The sPHENIX DAQ closely follows the design of the PHENIX DAQ [49]. The architecture is a fully pipelined design, which allows

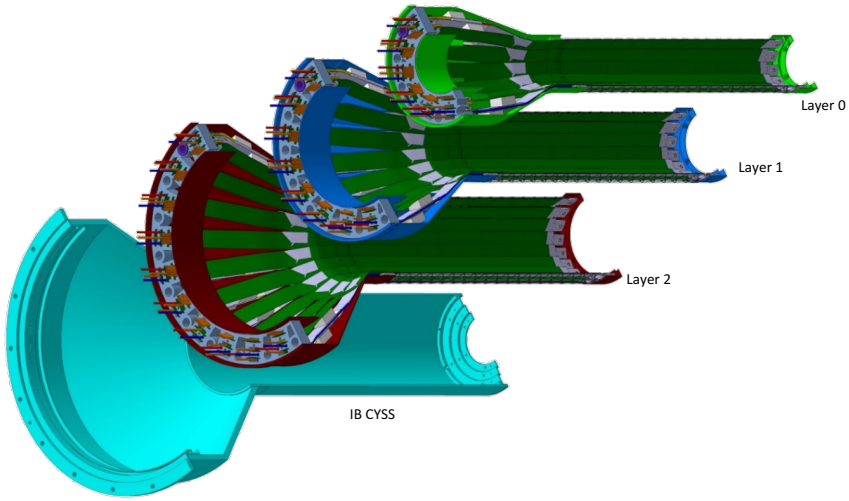

Figure 47: ALICE ITS/IB layer assembly into half detector, very similar assembly for the MVTX.

the next event to be triggered without waiting for the previous event to be fully processed. The existing PHENIX design allows for a depth of 5 such events to be buffered in front end modules before transmission. This multi-event buffering is the key concept to achieve the design event rate of 15 kHz while preserving DAQ livetime.

The MVTX will operate with the sPHENIX trigger, which is planned to have a latency of 4-6 μs and a maximum rate of 15 kHz.

6.10.1 Readout Modes

Two operating modes are possible for the MVTX: triggered readout and continuous readout. These modes correspond to operating modes of the ALPIDE chips used in the stave. Both modes will support the same interface to the sPHENIX trigger and DAQ: the sPHENIX DAMs (see Sec. 6.5.2) receive a trigger from the sPHENIX trigger system, and the DAMs send the appropriate MVTX data to the DAQ via PCIe.

In triggered readout, the sPHENIX DAMs (see Sec. 6.5.2) forward the received trigger to the FEMs (see Sec. 6.5.1). The FEMs forward the trigger to the staves, and the staves respond with hit data for that trigger. This triggered data is read out by the FEMs and DAMs. As shown in Fig. 48, the strobe signal which stores the matrix status is driven by an external trigger from the DAMs, issued whenever a physic event has been deemed worth to save. The trigger always follow the physical event (by the trigger latency), but data event are not lost due to the analogue delay.

In continuous readout, the DAMs issue periodic triggers to the staves at regular intervals of 5–20 μs. The staves respond to each periodic trigger with hit data for that interval, and the FEMs transmit this data to the DAMs. The DAMs buffer the FEM data packets, and respond to an sPHENIX trigger with the data packets corresponding to the trigger time.

As shown in Fig. 48, the continuous readout mode uses the same strobe signal of the triggered acquisition, only keeping it on for the length of a frame, therefore following a fixed time pattern regulated (or

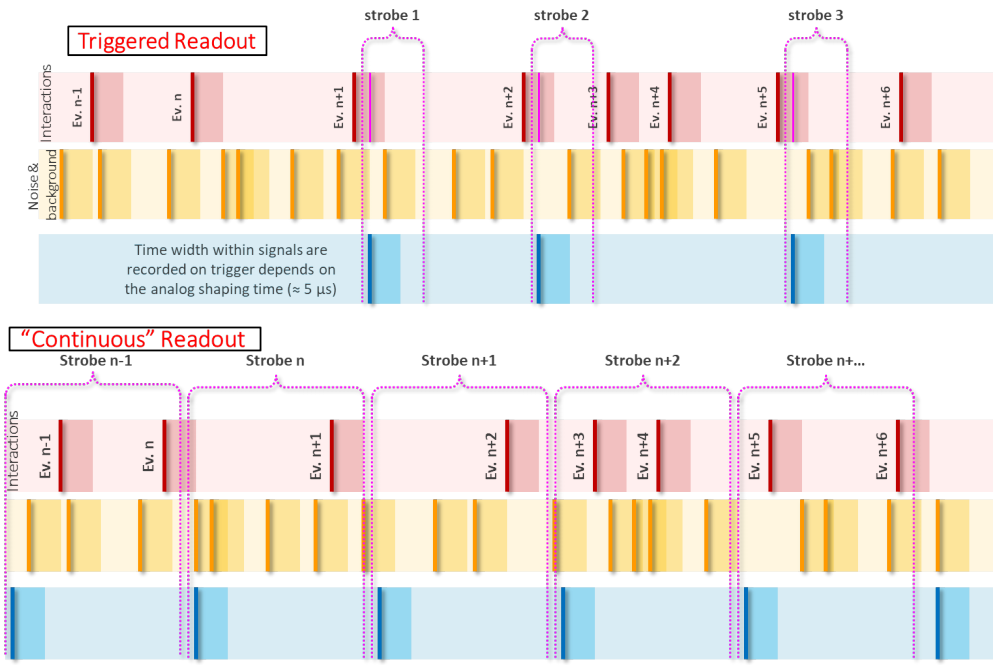

Figure 48: Timing diagrams for the two readout modes. Vertical bars represent pixel firing due to a particle from an interaction (physics event, red), pixel firing due to a background particle (background event, yellow), or pixel firing without being hit (blue, sensor noise). The shadow area after the bar illustrates graphically the period the signal in the pixel remains high (logical 1 at the comparator output) due to the shaping time. The dashed pink trigger lines represent the duration of the strobe signal.

simply synchronized) by some external signal. The external signal could set the actual frame length (hence the readout frequency), or it could be used to keep in synch across the whole bunch of frames generated by internal timing of the sensors themselves.

While the strobe is asserted, whichever event happens is stored into the matrix buffers. At the end of the integration time, the strobe is de-asserted for a minimal time (10s of nanoseconds) and a new frame begins. At the same time the in-pixel buffers from the previous frame are read out. In this configuration the frame rate is essentially limited by the available bandwidth, not by the sensor internal memory.

The choice of readout mode for the MVTX will be based on latency requirements, since the ALPIDE sensor's shaping time is still being optimized for the MVTX. Triggered readout reduces pileup and the overall data rate into the DAQ since the collision rate (up to 13 MHz for p+p and 200 kHz for Au+Au collisions) is much higher than the trigger rate (15 kHz) at RHIC, but continuous readout allows the MVTX to run with a shaping time that is faster than the sPHENIX trigger latency. Both modes produce pileup and data rates that are compatible with the MVTX physics performance and DAQ capacity.

6.10.2 Interface to sPHENIX DAQ

Figure 49 shows a schematic overview of the trigger, the front-end and the back-end systems. The Global Level 1 (GL1) system provides the trigger to the Master Timing Module (MTM), which is then distributed to the Granule Timing Module (GTM). These GTMs provide the subsystem-specific trigger signals and timing to the MVTX DAM. Each DAM is hosted in an off-the-shelf computer called the Event Buffering Data Compressor (EBDC). The DAMs transfer the MVTX data to the EBDCs via PCIe, and the EBDCs transfer the data to the sPHENIX DAQ via Ethernet. Each DAM only holds a fragment of the data for a given collision, which have to be combined together with data fragments from other sPHENIX detectors

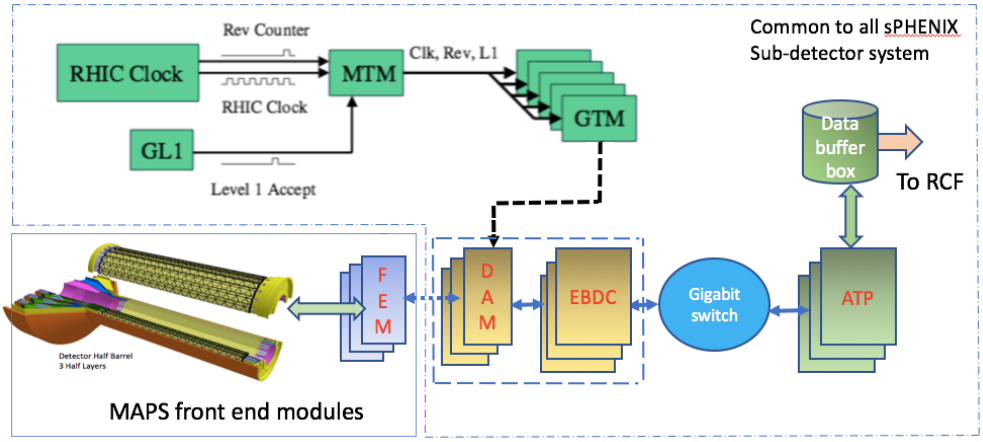

Figure 49: Online readout architecture for the MVTX using PCIe cards.

into a full event. This is accomplished on computers called Assembly and Trigger Processors (ATPs).

6.11 Offline software - detector simulation, geometry, offline tracking

In this session, we discuss the software used to generated all the performance plots shown in this proposal. In sPHENIX, tracking simulation and reconstruction is performed in a global software framework which includes all tracking subsystems, namely the MAPS-based Vertex Detector (MVTX), intermediate silicon strip tracker (INTT) and the outer time projection chamber (TPC). Even at this early stage of project, sophisticated and realistic simulation and reconstruction software have already been developed:

- The sPHENIX software framework provide a custom-designed unified platform for detector simulation, raw data decoding, reconstruction and analysis. It has been successfully used in data analysis and simulation for the PHENIX collaboration over the past decade.
- The GEANT4 simulation toolkit [39] is employed to simulate interactions between collision products and the full sPHENIX detector package along with the MVTX. The MVTX group has provided the detailed geometry description of the sensitive and passive material of the detector system. The hit information from GEANT4 is then digitized into detector hits.
- Adjacent hits in the MVTX are grouped into single clusters.
- A 5-dimensional Hough transform is employed to locate clusters from helical hit patterns in the time projection chamber (TPC) arising from tracks bending through the solenoid field to seed the track reconstruction.
- Track seeds are propagated outside-in from the time projection chamber (TPC) to the intermediate silicon strip tracker (INTT) and to the MAPS-based Vertex Detector (MVTX) by a Kalman filter [42] based pattern recognition algorithm.
- Clusters belong to the same track are fit using a Kalman-filter-based generic track-fitting toolkit [42], to extract track parameters including displacement at the vertex and the momentum vector at vertex.
- All tracks are fed into a generic tracking fitting toolkit, RAVE [40], to determine the locations of the primary and secondary vertices.

The track and vertex information is available for offline analysis through the sPHENIX software framework, which has been used to produce the preliminary performance plots discussed in Sec. 5. This software framework and algorithm chain will be further developed for physics and detector simulations and eventually for physics data analysis using the MVTX detector.

7 Organization and Collaboration

In this section, We summarize the current collaborating institutions and their focus areas. Based on their technical expertise and available resources, LANL, LBNL and MIT/Bates groups are leading the three major technical tasks of the project: 1) readout electronics integration; 2) carbon mechanical support frames production and 3) cooling and mechanical system integration, respectively.

Los Alamos National Laboratory (LANL) : Overall readout electronics and mechanical system integration, project management.

Brookhaven National Laboratory (BNL) : Global system integration and services, safety and monitoring, project management.

Lawrence Berkley National Laboratory (LBNL) : Carbon structure production, LV and HV power system, full detector assembly and test, project management.

Massachusetts Institute of Technology (MIT/Bates) : Global mechanical system integration and cooling.

Massachusetts Institute of Technology (MIT) : Stave assembly and test at CERN.

University of California at Los Angeles (UCLA) : Simulation and readout testing.

University of California at Riverside (UCR) : Detector assembly and test, simulations.

Central China Normal University (CCNU/China): MAPS chip and stave test at CERN and/or CCNU.

Charles University (CU/Czech) : MAPS stave production and QA.

University of Colorado (UCol) : *b*-jet simulations and future hardware.

Czech Technical University (CTU/Czech) : MAPS stave production and QA at CERN.

Florida State University (FSU) : Offline software and simulations.

Georgia State University (GSU) : Online software and trigger development.

Iowa State University (ISU) : Detector assembly and test, simulations.

National Central University (NCU/Taiwan)* : Stave assembly and test, simulations.

University of New Mexico (UNM) : Cabling & connectors.

New Mexico State University (NMSU) : Tracking algorithm and physics simulations.

Purdue University (PU): Detector assembly and test, simulations.

Univ. of Science and Technology of China (USTC/China) : MAPS chip and stave test, simulations.

Sun Yat-Sen University (SYSU/China) : MVTX detector and physics simulations.

University of Texas at Austin (UTA) : MVTX readout electronics integration, Readout Units production and test.

Yonsei University (YSU/Korea) : MAPS chip production QA, readout electronics test and simulations

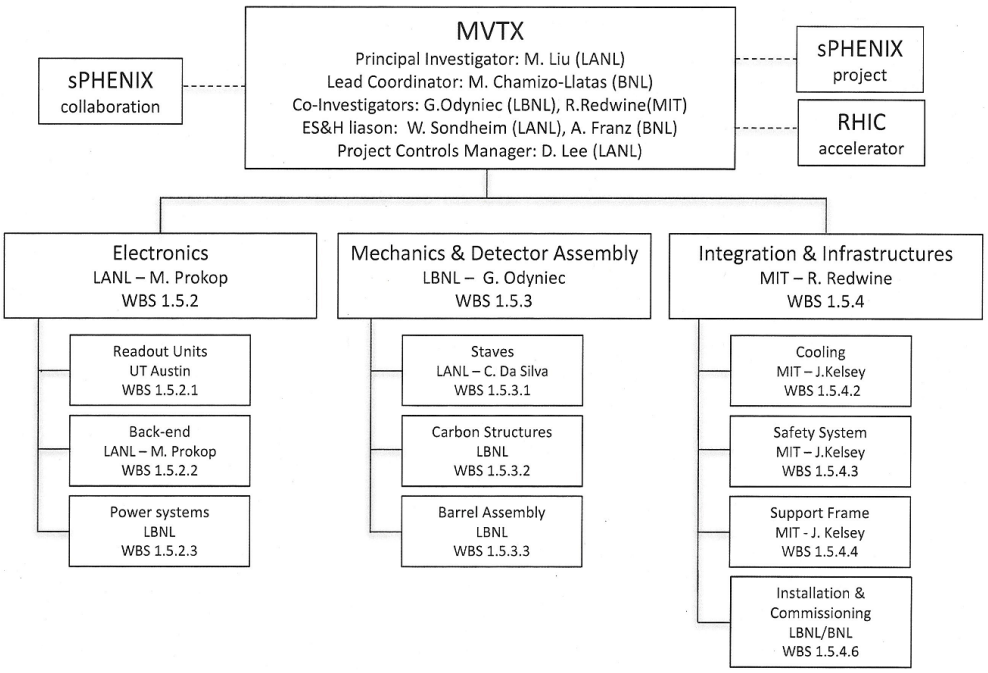

Figure 50: Organization chart of the MVTX project.

RIKEN/RBRC (RIKEN/Japan) : Mechanical integration, cooling, cabling, simulation, patter recognition.

*** Note:** Expressed interest to join the sPHENIX Collaboration.

Figure 50 shows the organization chart and tasks assigned for each Institution.

Detector R&D is underway at LANL utilizing the internal LDRD funding ($5M over 3 years, FY17-19). This R&D aims to develop a prototype telescope detector with four MVTX staves and the full readout electronics chain needed to comply with the sPHENIX DAQ. LANL will work closely with the ALICE ITS Upgrade Group at CERN, UT-Austin, LBNL and BNL groups on the final MVTX readout system design and production. The LANL LDRD project will also carry out the initial design of the MVTX mechanical system to integrate into sPHENIX. MIT Bates Center will lead the final mechanical integration effort and has designated 0.25 FTE for an engineer and 1 FTE for a technician to work on the mechanical system integration. LBNL will lead the effort of carbon structure fabrication, detector assembly and system readout test, and also the production of the LV and HV power distribution boards and control system based on the ALICE design. Other institutions will lead or help on various key tasks according to their available resources and expertise, as shown in Fig. 50.

8 Schedule and Cost Baseline

The MVTX project for sPHENIX relies on the fact that much of the conceptual design, prototype design, and prototyping has/will be done by the ALICE collaboration at CERN and through a Los Alamos National Laboratory (LANL) LDRD development effort. The MVTX detector will use the latest generation MAPS silicon sensors (ALPIDE) developed by the ALICE collaboration. The design of the final MVTX readout and the conceptual mechanical systems will be completed through LANLs LDRD effort. This is not part of the requested project funds, but is crucial to bring the project to a high level of maturity and to reduce the risks.

The estimated cost of the final design effort, procurement, assembly and installation into the sPHENIX experiment is estimated to be $6.6M. The cost includes 35% contingency and assumes production of the staves using the ALICE facility at CERN immediately following the ALICE production, which significantly reduces the cost and technical risks of the MVTX detector. Inflation of 3% per year is included.

The MVTX schedule starts in September 2018 in order to be ready for beam in the 1st quarter of FY23.

MVTX	$M
Project Management	0.98
Electronics	1.30
Mechanics and Detector Assembly	3.23
Integration and Infrastructures	1.02
TOTAL	**6.54**

Figure 51: MVTX High Level Cost.

8.1 Schedule

Figure 51 is a high level view of the Cost for the MVTX effort and Figure 52 is the project timeline. The schedule, cost, and technical risks are optimized by concatenating the MVTX production at CERN following the ALICE production, which gives a window for MVTX stave production starting the last quarter of FY18.

One of the largest risk factors for the project concerns the availability of the ALICE CERN facility for MVTX production. To reduce the MVTX project cost it is important that we are able to take advantage of the production lines at CERN. The Cost and Schedule is designed to use the CERN personnel and production lines at CERN. By doing this, the MVTX project does not have to implement a completely new production facility with the necessary equipment, clean facilities, jigs, infrastructure, and personnel training that would be necessary. Currently, the end of ALICE production is in the 3rd quarter of FY 2018. We expect to begin the MVTX stave production immediately after ALICE production ends so we will need to have funding available to allow CERN to continue the production factory without delay. The beginning of MVTX stave production is then in the beginning of the 4th quarter 2018. The timeline shows that there is a 9 month schedule contingency because the MVTX date for installation is ready approximately 9 months before the end of sPHENIX installation.

8.2 Cost

The stave production cost at CERN is derived from a quote from the ALICE inner tracker project leader based on the actual cost of the ALICE staves, including Manpower costs. Costs for the FEM were based on as built costs for the version 1 prototype at the University of Texas, Austin who are designing the FEM. The production of the FEM will be at CERN and we will piggy-back on that production to produce the 58 units

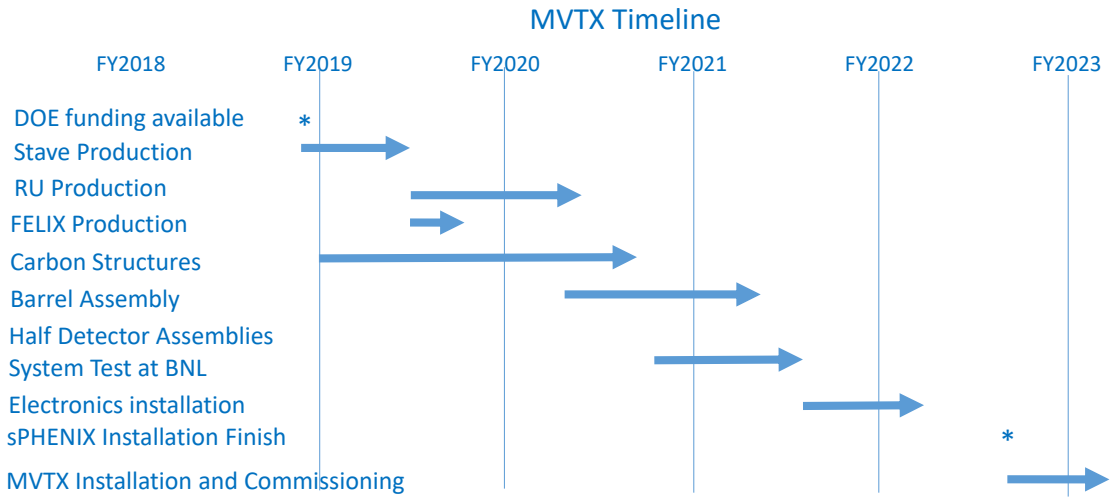

Figure 52: MVTX Timeline

we need. The cost of the DAM board, which was designed at BNL, is based on an as built prototype that has been tested and is on a second version. We will piggy-back on the DAM production at BNL to produce the 8 units that we need. Mechanical procurements costs are based on an analysis done by the carbon composite shop at LBNL who are currently involved with the production of similar composite structures for the ALICE upgrade.

The mechanical design of the MVTX detector will be similar to the ALICE design but with a slightly larger radius because the BNL beam pipe is slightly larger than the ALICE beam pipe and because the MVTX is modifying the carbon structures from the ALICE designs to be able to integrate the MVTX with the sPHENIX sub-detectors. Mechanical Integration into sPHENIX requires a clear definition of the surrounding systems. It further requires close cooperation between the INTT and MVTX groups. MVTX and INTT engineers will work with the newly formed sPHENIX group responsible for overall integration to insure this cooperation. The MVTX has included a cost for the design and fabrication only for the MVTX support structure. Not included is the design and fabrication for the INTT support structure. Contingency is is set at 35%. The funding profile is shown in Fig. 53. The funding profile does not include uncosted physicists and postdocs. FY2018 funding is based on the need for stave production in the last quarter of FY 2018.

8.3 Resources

The level of resources is based on previous experience in other projects such as the FVTX/PHENIX upgrade, ITS/ALICE upgrade, and the recent HFT/STAR upgrade. Resource costs are institution specific with fully costed hourly rates used. The level of resources is shown in Fig. 54. Half of the anticipated resources are uncosted to the project and comprise physicists and postdocs, as they are responsible for much of the testing and QA as well as the installation.

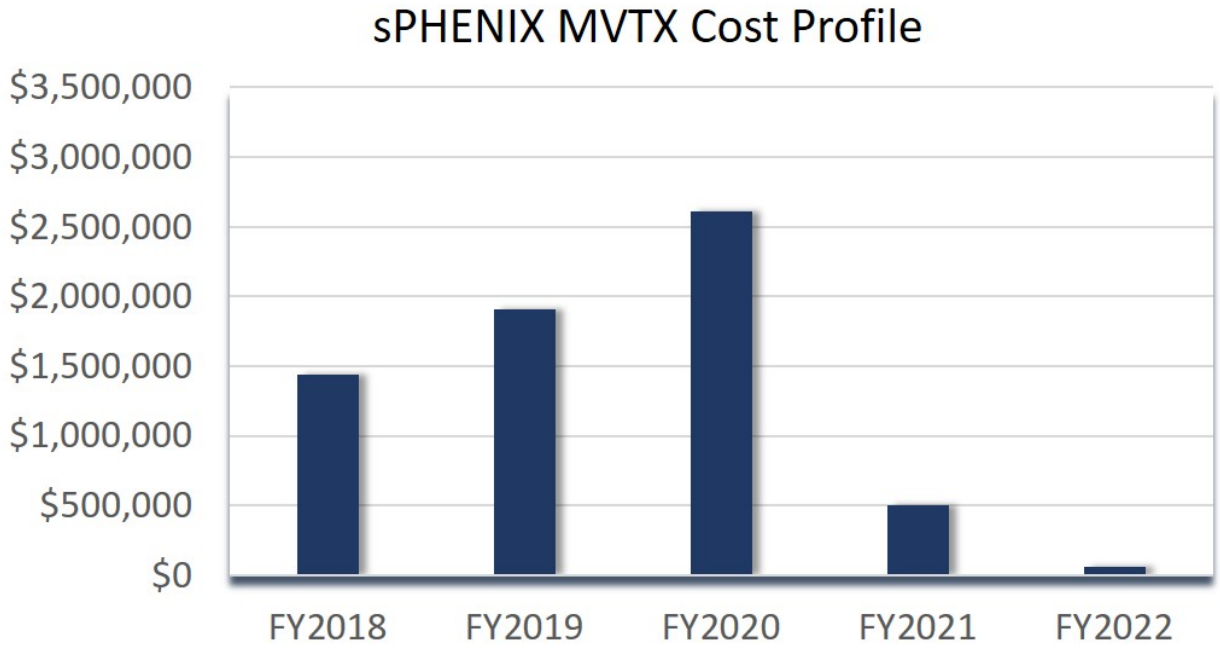

Figure 53: MVTX Funding Profile. Physicists and postdocs are uncosted to the project and therefor are not included in the funding profile.

8.4 Milestones

The milestones of the project are shown in the table below.

Milestones	Time
End of Stave Production	3rd Qtr FY 2019
RU testing complete	1st Qtr FY 2020
1st Half barrel assembly done	3rd Qtr FY 2020
1st half barrel shipped to BNL	1st Qtr FY 2021
2nd half barrel shipped to BNL	2nd Qtr FY 2021
Installation Complete	4th Qtr FY 2022
Ready for Beam	1st Qtr FY 2023

Table 9: Milestones

8.5 Major Cost Items

Here we list the cost of major items for the MVTX project.

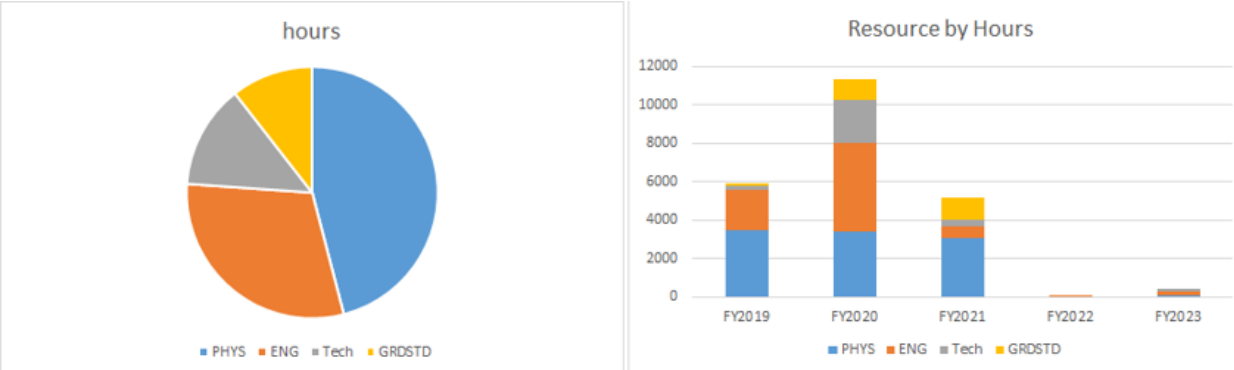

Figure 54: MVTX Resource Levels. Physicists (PHYS) is an uncosted resource to the project.

WBS	Task Name	Cost (K)	Cost with Contingency+ Passthru (K)
1.5.3.1.1	Produce 84 staves	$966	$1337
1.5.2.2	Readout Units(RDO)	$480	$664
1.5.5.3.2.3.2	CYSS Cylindical Structure	$319	$424
1.5.5.3.2.3.3	COSS Conical Half Shell	$329	$438
1.5.4.3	Safety Systems	$139	$191
1.5.4.4	Stave Support+ Global Interface	$308	$465

Table 10: Major Cost Items

End of proposal narrative; supplemental materials to follow.

A LANL LDRD R&D

The Los Alamos National Lab leads the initial R&D work for the proposed MVTX including:

1. To optimize the ALPIDE chip operation point to best fit the sPHENIX requirements on a test bench with cosmic rays and external sources.

2. To develop the full readout chain and control electronics system based on the ALICE ITS ALPIDE sensors and front-end readout electronics that can operate in the sPHENIX environment and to adapt the full readout chain of the MVTX to the sPHENIX trigger and timing scheme.

3. To complete the conceptual mechanical system design for the MVTX integration at sPHENIX.

4. To complete the MVTX prototype telescope that consists of several ALPIDE sensors and/or staves and to operate the telescope with the full readout chain for cosmic ray, source and beam test.

Every component of the full readout and control system has been tested through the LDRD project. Preliminary results verify that the detector performances satisfy the sPHENIX physics requirements. The full readout chain has been successfully demonstrated at LANL with a stave. A brief description of the LANL LDRD R&D recent accomplishments and current development efforts are provided in this section.

A.0.1 MVTX chip and stave performance characterization and optimization

With the MAPS chip and stave production in progress for ALICE at CERN, initial tests to characterize the performance of the ALPIDE chips and full staves have been carried out at LANL with a mock-up readout electronic module of the FEM and DAM named as "MOSAIC" which is developed by INFN in Italy. A range of ALPIDE chip readout speeds, thresholds, trigger configurations trigger delay time latency, and different operation modes ("Continuous" or "Triggered") of the ALPIDE chips have been tested. The following chip performance characteristics have been verified through a scan of all available chips and the single stave at LANL.

1. The average dead/bad channel fraction has been measured to be much less than 1% throughout the digital scan for all chips.

2. The signal over noise ratio has been measured to be larger than 60 with the ALICE default chip parameter settings. Figure 55 presents the test results of threshold and noise for one ALPIDE chip through the charge injection test. No significant change in the threshold to noise ratio is seen for all other chips and also for different readout speeds.

3. The external trigger mode of the ALPIDE chip has been studied with the MOSAIC readout module through the test of both cosmic ray muons and ^{90}Sr beta decayed electrons at LANL with a trigger delay time of 2 μs. Figure 56 presents the hit distribution in the collimated ^{90}Sr source test. Clear collimator structure has been observed in the coincidence triggered events.

4. The cluster size which is correlated with the MAPS pixel hit spatial resolution has been characterized in both with the cosmic ray muons and the ^{90}Sr beta decayed electrons. The average cluster size from the single layer test is consistent with the CERN beam test results. Fig. 57 shows the cluster size distribution (left), and also the cluster profile along either the column (middle) or row direction (right), plotted in several categories based on the cluster size. More precise measurements of tracking resolution and efficiency using a setup with more than two sensor layers is in preparation and will be carried out soon.

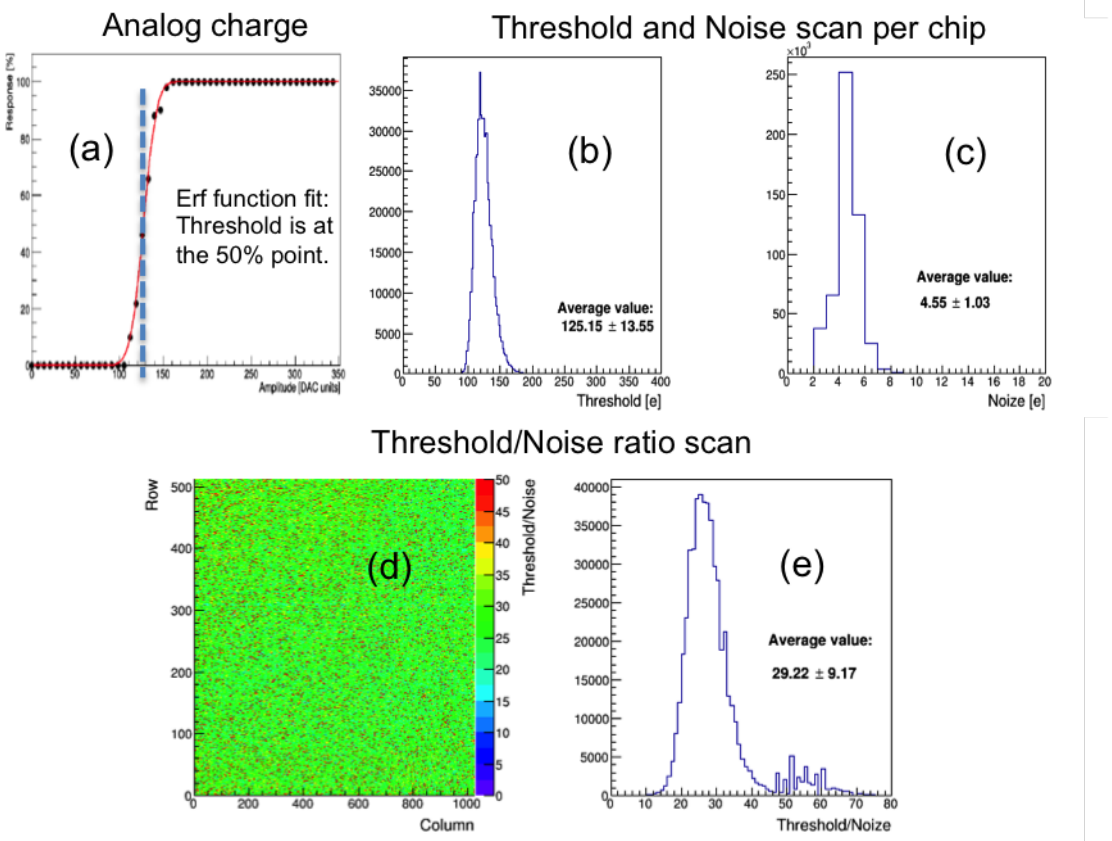

Figure 55: From left to right: (a) The injection charge analog signal, and the threshold is chosen at 50% level of the signal region. (b) The threshold (in unit of electrons) distribution. (c) The noise (in unit of electrons) distribution. (d) The distribution of threshold/noise ratio in column and row 2D plane. (e) The threshold/noise ratio distribution.

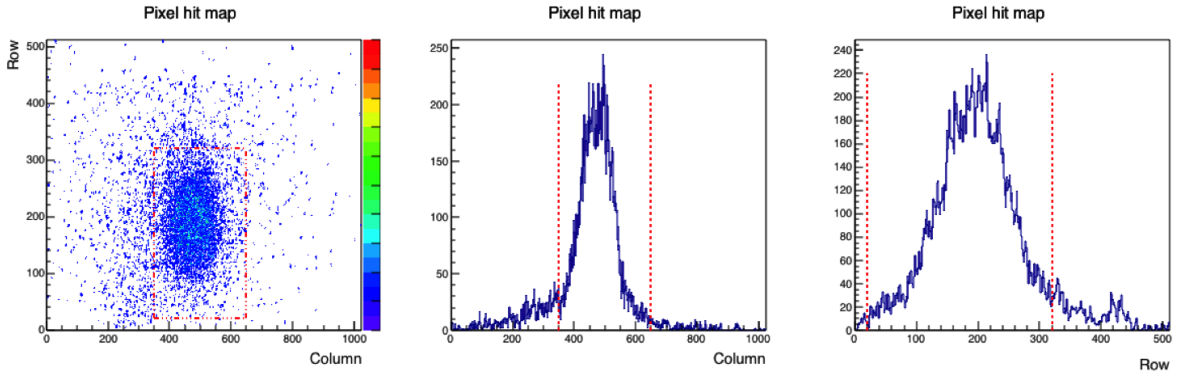

Figure 56: Clear collimator structure has been observed on the ALPIDE chip in the 2D pixel hit map (left), the profile along column (middle) and row (right) in ^{90}Sr source test with a collimator.

5. An initial study of hit efficiency vs the trigger time latency has been performed. By lowering the threshold of the discriminator on the output of the ALPIDE chip, we have extended the trigger time window from around 7 μs to around 10 μs without loosing hit efficiency (within the precision of

limited statistics from cosmic rays). This allows us to operate ALPIDE within the sPHENIX trigger latency. More precision scan for ALPIDE operation parameters optimization for sPHENIX is under the way and will be completed in late 2018.

6. As a proof of principle study, tracking software based on two layers of ALPIDE chips has been developed for a cosmic ray test setup. The event display of one cosmic ray track hits is shown in Fig. 58.

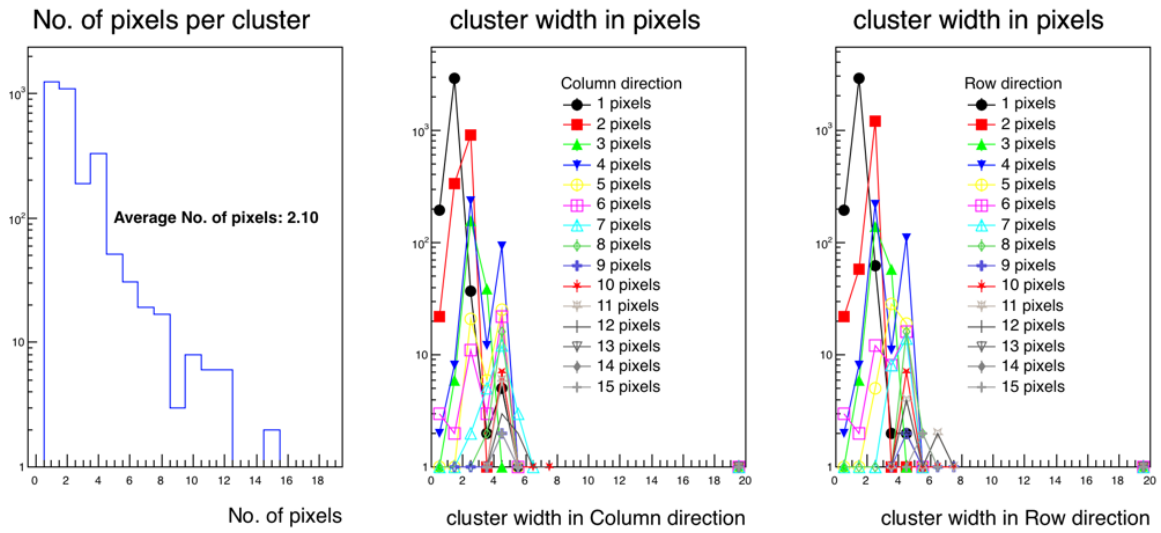

Figure 57: ALPIDE pixel hit distributions from the single chip cosmic ray test setup with scintillator coincidence trigger, the cluster size (in unit of pixels) distribution (left), the cluster profile along the column direction (middle) and along the row direction (right).

A.0.2 LANL LDRD readout R&D accomplishments

We successfully developed firmware and control software to demonstrate a full-speed readout chain running on an external trigger (15 kHz) with one 9-chip stave, one ALICE RU front-end electronics (FEM) and ATLAS FELIX back-end electronics (DAM) and sPHENIX RCDAQ, meeting or exceeding the sPHENIX specifications.

- High-speed readout (1.2Gbps per chip) of a single ALPIDE chip (or a 9-chip stave) on external trigger at 15 kHz using the FEM and DAM.
- Emulated 8 FEMs using 1 fiber per link on the DAM with a loop back test at the sPHENIX trigger rate. This demonstrates that the DAM can transfer the MVTX data at full speed to the DAQ without any loss.
- Successfully integrated DAM DMA (Direct Memory Access) to RCDAQ (sPHENIX Readout) and stored raw data with sPHENIX data format on the local disk.

The readout achievements have helped us to significantly reduce the cost and technical risks of the MVTX project.

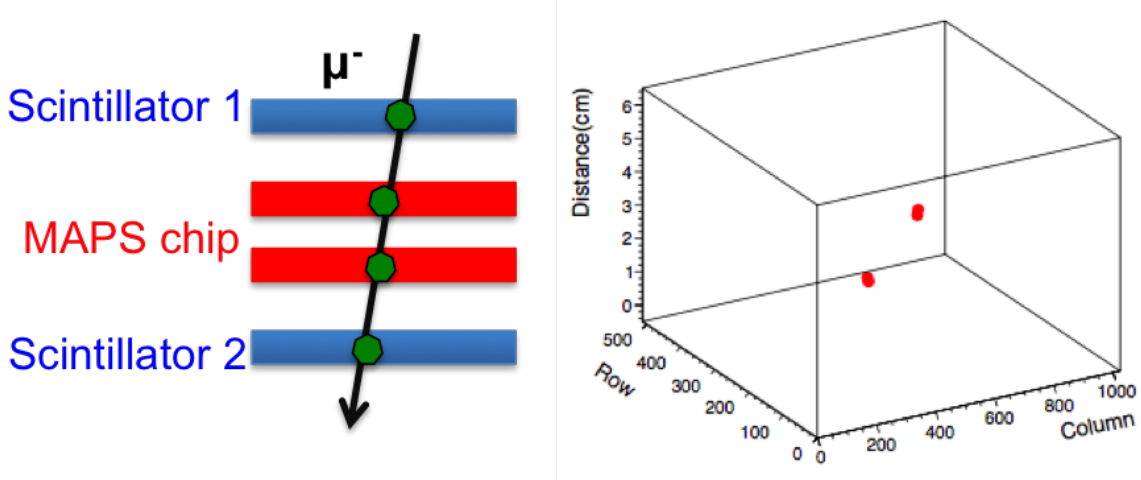

Figure 58: A clean cosmic ray track has been observed in the two ALPIDE sensor layer setup for cosmic rays. The cosmic ray coincidence trigger is formed from scintillator 1 and scintillator 2 above and below the two ALPIDE chips.

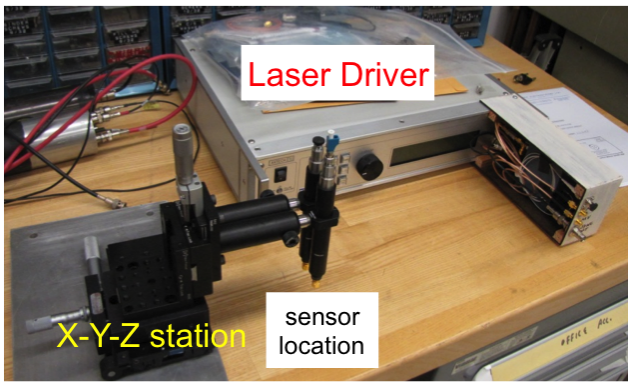

Figure 59: The Laser test stands. The laser driver can generate laser pulses with MIP-level signal to each pixel.

A.0.3 LANL LDRD ongoing R&D efforts

Current LDRD development efforts focus on the multi-chip stave readout with the FEM+DAM+RCDAQ full readout chain, continuing optimization of the ALPIDE chip performance parameters and setting up a telescope with four layers of chips(or staves). The goals include:

- Scan the full ALPIDE parameter space to optimize the operation point for sPHENIX with a laser test-bench as shown in Fig. 59.
- Set up a multi-layer sensor telescope to study the tracking resolution, efficiency, etc. with cosmic rays and test beam.
- Continue evaluating the chip/stave performance with cosmic rays, external sources and beam test with the sPHENIX Trigger and Timing system. Two beam tests are scheduled to take large sample of clean

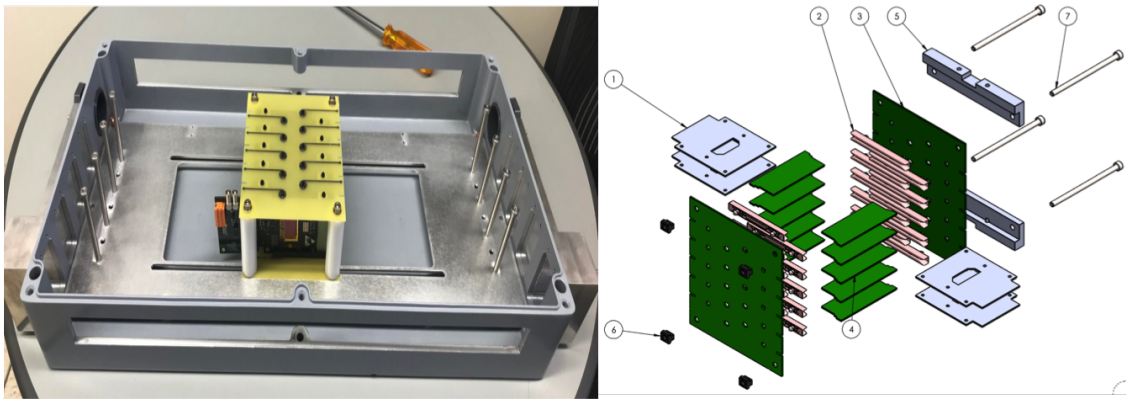

Figure 60: The 4 layer ALPIDE chip (stave) telescope prototype mechanical box (left) and the construction of box.

tracks for the detector alignment study and also momentum dependence of tracking resolution. One is scheduled in March 2018 and the other in spring 2019.

- Evaluate Signal Integrity of the FireFly data cable performance at various lengths for MVTX integration to optimize the overall sPHENIX detector system layout.
- Evaluate and understand Flex Cable effects on the FireFly data cable performance.
- Finalize development of the radiation upset mitigation functionality also known as scrubbing within the FEM.
- Finalize development of remote programming of the FEM via fiber optic interface and remote programming of the DAM over PCIe.

B Impact of sPHENIX baseline rescoping

The physics reach of the MVTX physics program is closely tied to the scope of the baseline sPHENIX detector. Prior to determining the baseline of the sPHENIX project, various detector scopes are being considered. In particular, a reduced scope is discussed in the sPHENIX Conceptual Design Report (CDR) [8]. Comparing to the full sPHENIX scope as described in the sPHENIX scientific proposal [7], the acceptance of the electromagnetic calorimeter has been reduced from $|\eta| < 1.1$ to $|\eta| < 0.85$ and no inner hadronic calorimeter would be built. This section discusses the change in the MVTX physics program assuming with full MVTX detector with the reduced sPHENIX.

Under the reduced sPHENIX scope, the tracking detector acceptance remains the same as the full scope. Therefore, for the B-meson program, which mainly relies on tracking, the impact is minimal and we expect to reach the full projected physics performance as shown in Sec. 5.3.

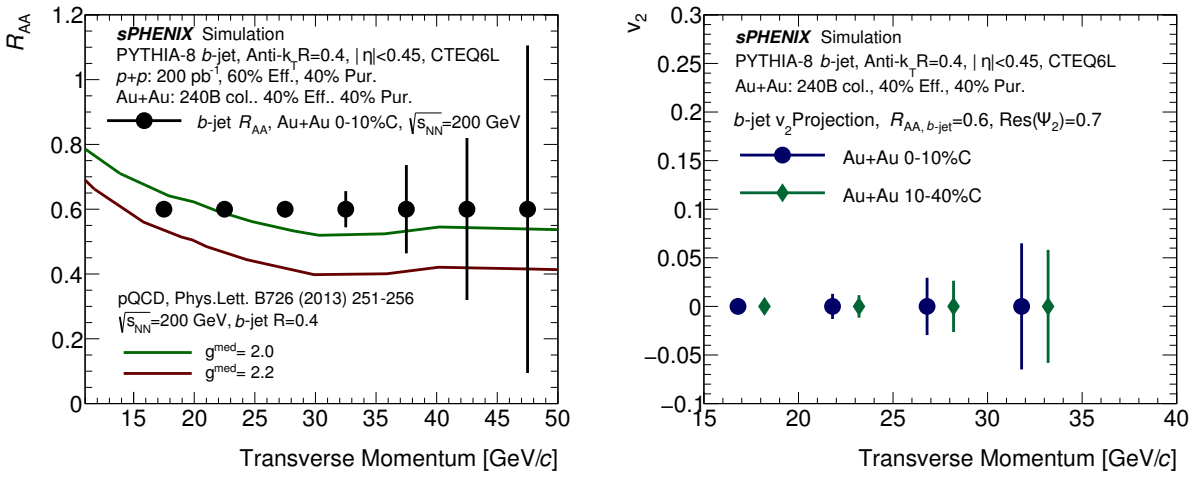

Figure 61: Under the reduced sPHENIX scope [8], the projection of sPHENIX inclusive *b*-jet measurements of the nuclear suppression factor (left) and elliptical flow (right).

However, the reduction of the electromagnetic calorimeter acceptance reduces the calorimetry coverage of $R = 0.4$ jets from $|\eta_{\text{jet}}| < (1.1 - 0.4)$ to $|\eta_{\text{jet}}| < (0.85 - 0.4)$, i.e. $|\eta_{\text{jet}}| < 0.45$. This reduction directly impacted the statistics and coverage for the heavy flavor jet program when compared to the full scope projections as discussed in Sec. 5.2. Specifically, under this reduction the projection for *b*-jet nuclear suppression factor and elliptical flow are shown in Fig. 61. When compared with full-sPHENIX-scope projections as shown in Figs. 22 and 23, there is a 25% increase in the statistical uncertainty, which impact the highest transverse momentum reach. Similar worsening in the uncertainty is expected in the the mean di-*b*-jet transverse momentum balance as shown in Fig. 62. Despite the impact on the highest transverse momentum reach, the uniqueness and main impact of the MVTX heavy flavor jet program remains compelling even with the potential reduction in sPHENIX scope.

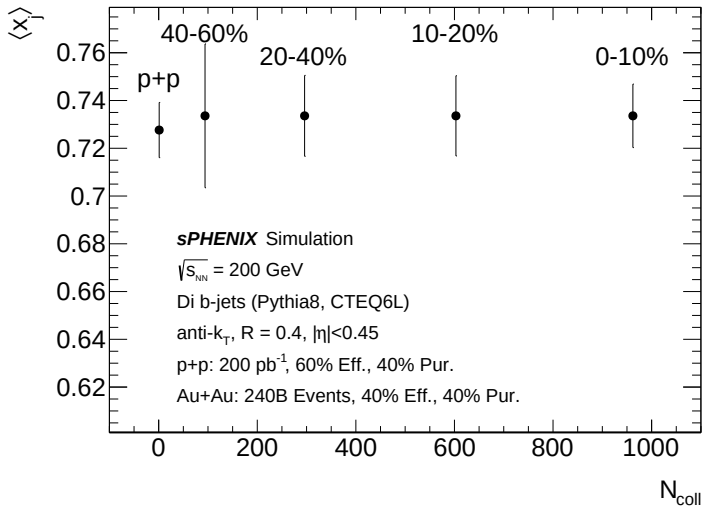

Figure 62: Projections for the mean di-b-jet transverse momentum balance, $\langle x_j \rangle$ as a function of N_{coll} in p+p and Au+Au collisions at $\sqrt{s_{NN}}$ = 200 GeV under the reduced sPHENIX scope.

C Abbreviations and Code Names

Acronyms

ALICE A Large Ion Collider Experiment at CERN. 1, 2, 4–6, 14–18, 20, 34, 35, 37, 39, 43, 44, 46–50, 56–58, 62, 64

ALPIDE ALice PIxel DEtector. 2, 14, 16, 33–40, 43, 51, 52, 57, 62–65

ATP Assembly and Trigger Processor. 53

BDT Boosted-Decision-Tree. 29, 32

BNL Brookhaven National Laboratory. 1, 46, 48, 50, 56, 58

CCSS Cylindrical and Conical Structural Shells. 46

CERN European Organization for Nuclear Research. 1, 2, 17, 39, 47, 49, 55–57, 62

CMS Compact Muon Solonoid. 5–7, 25, 27

COSS Conical Support Shell. 46

CYSS cylindrical structural shell. 18, 50

DAM Data Aggregation Module. 14, 34, 40–42, 51, 52, 58, 62, 64–66

DAQ data acquisition. 2, 12, 14, 39, 41, 50–52, 56, 64

DCA Distance of Closest Approach. 13, 18, 21, 22, 24, 28–30, 32

DOE Department of Energy. 2

DTU Data Transmission Unit. 39

EBDC Event Buffering Data Compressor. 39, 41, 52

FELIX Front End Link eXchange (from ATLAS). 39, 64

FEM Front End Module. 14, 34, 39–41, 43, 44, 51, 57, 62, 64–66

FONLL Fixed Order Next-to-Leading-Log. 29, 30, 32

FPC polyimide flexible printed circuit. 17, 39

FPGA field-programmable gate array. 39, 41

GBT GigaBit Transceiver. 39, 40

GL1 Global Level 1. 52

GTM Granule Timing Module. 52

HFT Heavy Flavor Tracker. 1, 9, 29, 58

HIC Hybrid Integrated Circuit. 17

IB Inner Barrel. 15, 18, 34, 37, 39, 44, 47, 48

INTT intermediate silicon strip tracker. 12, 14, 15, 18–21, 45–47, 49, 58

ITS Inner Tracking System. 1, 15–18, 34, 35, 37, 39, 43–49, 56, 58, 62

LANL Los Alamos National Laboratory. 1, 2, 43, 45–48, 55–57, 62

LBNL Lawrence Berkley National Laboratory. 2, 39, 43, 45, 47–49, 55, 56, 58

LDRD Laboratory Directed Research and Development. 1, 2, 56, 57, 62

LHC Large Hadron Collider. 1, 2, 4, 5, 9–11, 24, 25

LRP Long Range Plan. 1

MAPS Monolithic Active Pixel Sensor. 1, 15, 16, 33, 39, 43, 55, 57, 62

MBD Minimum Bias Detector. 46

MC Monte Carlo. 28, 32

MEB Multi Event Buffer. 36

MIT Massachusetts Institute of Technology. 2, 55, 56

MOSAIC . 43

MTM Master Timing Module. 52

MVTX MAPS-based Vertex Detector. 1–4, 7–22, 24, 26–28, 30, 32–35, 37, 39–59, 62, 64, 66, 67

NSAC National Science Advisory Committee. 1, 4

PHENIX Pioneering High Energy Interaction eXperiment. 4–6, 27

pQCD perturbative Quantum Chromodynamics. 30

QA Quality Assurance. 39, 55, 58

QCD quantum chromodynamics. 4, 6, 11

QGP Quark Gluon Plasma. 1–11, 21, 23, 26, 30

RHIC Relativistic Heavy Ion Collider. 1–12, 14, 26, 29, 33, 52

RU Readout Unit (from ALICE). 39, 64

sPHENIX solenoidal Pioneering High Energy Interaction eXperiment. 1–5, 7, 9, 11–19, 21, 22, 24–27, 30, 32, 33, 35, 39–54, 56–58, 62, 64–68

STAR the STAR experiment at RHIC. 1, 4–6, 8–10, 14, 29–31, 58

TMVA Toolkit for Multivariate Variable Analysis. 29, 32

TPC time projection chamber. 12, 14, 15, 45, 46, 48, 49

D Literature Cited

References

[1] Jinrui Huang, Zhong-Bo Kang, and Ivan Vitev. Inclusive b-jet production in heavy ion collisions at the LHC. *Phys. Lett.*, B726:251–256, 2013.

[2] S. S. Cao, G.Y. Qin, and S. A. Bass. Energy loss, hadronization and hadronic interactions of heavy flavors in relativistic heavy-ion collisions. *Phys. Rev.*, C92:024907, 2015.

[3] Min He, Rainer J. Fries, and Ralf Rapp. Heavy-Quark Diffusion and Hadronization in Quark-Gluon Plasma. *Phys. Rev.*, C86:014903, 2012.

[4] T. Song, H. Berrehrah, J. M. Torres-Rincon, L. Tolos, D. Cabrera, W. Cassing, and E. Bratkovskaya. Single electrons from heavy-flavor mesons in relativistic heavy-ion collisions. *Phys. Rev.*, C96:014905, 2017.

[5] J.C. Xu, J.F. Liao, and M. Gyulassy. Bridging soft-hard transport properties of quark-gluon plasmas with cujet3.0. *JHEP*, 1602:169, 2016.

[6] L. Adamczyk et al. Measurement of D^0 Azimuthal Anisotropy at Midrapidity in Au+Au Collisions at $\sqrt{s_{NN}}$=200GeV. *Phys. Rev. Lett.*, 118(21):212301, 2017.

[7] A. Adare et al. An Upgrade Proposal from the PHENIX Collaboration. 2015.

[8] sPHENIX Conceptual Design Report. 2017.

[9] L. Adamczyk et al. Observation of D^0 Meson Nuclear Modifications in Au+Au Collisions at $\sqrt{s_{NN}}$ = 200 GeV. *Phys. Rev. Lett.*, 113(14):142301, 2014.

[10] Albert M Sirunyan et al. Nuclear modification factor of D^0 mesons in PbPb collisions at $\sqrt{s_{NN}}$ = 5.02 TeV. 2017.

[11] Shreyasi Acharya et al. D-meson azimuthal anisotropy in mid-central Pb-Pb collisions at $\sqrt{\mathbf{s}_{\mathrm{NN}}} = \mathbf{5.02}$ TeV. 2017.

[12] C. Aidala et al. B-meson production at forward and backward rapidity in $p+p$ and Cu + Au collisions at $\sqrt{s_{NN}} = 200$ GeV. *Phys. Rev.*, C96(6):064901, 2017.

[13] A. Adare et al. Single electron yields from semileptonic charm and bottom hadron decays in Au+Au collisions at $\sqrt{s_{NN}} = 200$ GeV. *Phys. Rev.*, C93(3):034904, 2016.

[14] Alexander Schmah. Highlights from the star experiment at rhic. *Nuclear Physics A*, 967(Supplement C):11 – 18, 2017. The 26th International Conference on Ultra-relativistic Nucleus-Nucleus Collisions: Quark Matter 2017.

[15] Yu.L Dokshitzer and D.E Kharzeev. Heavy-quark colorimetry of qcd matter. *Physics Letters B*, 519(3):199 – 206, 2001.

[16] Guy D. Moore and Derek Teaney. How much do heavy quarks thermalize in a heavy ion collision? *Phys. Rev.*, C71:064904, 2005.

[17] Santosh K. Das, Francesco Scardina, Salvatore Plumari, and Vincenzo Greco. Heavy-flavor in-medium momentum evolution: Langevin versus Boltzmann approach. *Phys. Rev.*, C90:044901, 2014.

[18] A. Adare et al. Energy Loss and Flow of Heavy Quarks in Au+Au Collisions at $\sqrt{s_{NN}}$ = 200 GeV. *Phys. Rev. Lett.*, 98:172301, 2007.

[19] B.I. Abelev et al. Transverse Momentum and Centrality Dependence of High-p_T Nonphotonic Electron Suppression in Au+Au Collisions at $\sqrt{s_{NN}}$ = 200 GeV. *Phys. Rev. Lett.*, 98:192301, 2007.

[20] Betty Abelev et al. Suppression of high transverse momentum D mesons in central Pb-Pb collisions at $\sqrt{s_{NN}}$ = 2.76 TeV. *JHEP*, 09:112, 2012.

[21] S.K. Das, F. Scardina, S. Plumari, and V. Greco. Heavy-flavor in-medium momentum evolution: Langevin versus boltzmann approach. *Phys. Rev.*, C90:044901, 2014.

[22] A. Andronic et al. Heavy-flavour and quarkonium production in the LHC era: from protonproton to heavy-ion collisions. *Eur. Phys. J.*, C76(3):107, 2016.

[23] The Review of Particle Physics (2017). 2017.

[24] Serguei Chatrchyan et al. Evidence of b-Jet Quenching in PbPb Collisions at $\sqrt{s_{NN}} = 2.76$TeV. *Phys. Rev. Lett.*, 113(13):132301, 2014. [Erratum: Phys. Rev. Lett.115,no.2,029903(2015)].

[25] Long Zhou. Measurements of Λ_c^+ and D_s^+ production in Au+Au collisions at $\sqrt{s_{\rm NN}}$ = 200 GeV. *Nucl. Phys.*, A967:620–623, 2017.

[26] Anastasia Barbano. D-meson nuclear modification factor and elliptic flow measurements in Pb+Pb collisions at $\sqrt{s_{\rm NN}}$ = 5.02 TeV with ALICE at the LHC. *Nucl. Phys.*, A967:612–615, 2017.

[27] E. Norrbin and T. Sjostrand. Production and hadronization of heavy quarks. *Eur. Phys. J.*, C17:137–161, 2000.

[28] Jinrui Huang, Zhong-Bo Kang, Ivan Vitev, and Hongxi Xing. Photon-tagged and B-meson-tagged b-jet production at the LHC. *Phys. Lett.*, B750:287–293, 2015.

[29] CMS Collaboration. Splitting function in pp and PbPb collisions at 5.02 TeV. 2016.

[30] K Kauder. Measurement of the Shared Momentum Fraction zg using Jet Reconstruction in p+p and Au+Au Collisions with STAR. 2016.

[31] Andrew J. Larkoski, Simone Marzani, Gregory Soyez, and Jesse Thaler. Soft Drop. *JHEP*, 05:146, 2014.

[32] Z.-B. Kang, F. Ringer, and I. Vitev. Effective field theory approach to open heavy flavor production in heavy-ion collisions. *JHEP*, 1703:146, 2017.

[33] H. Li and I. Vitev. Private Communication. 2017.

[34] sPHENIX preConceptual Design Report. 2015.

[35] G. Contin, L. Greiner, J. Schambach, M. Szelezniak, et al. The STAR MAPS-based PiXeL detector. *arXiv:1710.02176*, 2017.

[36] B Abelev et al. Technical Design Report for the Upgrade of the ALICE Inner Tracking System. *J. Phys.*, G41:087002, 2014.

[37] Gianluca Aglieri Rinella. The ALPIDE pixel sensor chip for the upgrade of the ALICE Inner Tracking System. *Nucl. Instrum. Methods Phys. Res., A*, xx:xx, 2016. In Press.

[38] M. Mager. ALPIDE, the Monolithic Active Pixel Sensor for the ALICE ITS upgrade. *Nucl. Instrum. Meth.*, A824:434–438, 2016.

[39] S. Agostinelli et al. GEANT4: A Simulation toolkit. *Nucl. Instrum. Meth.*, A506:250–303, 2003.

[40] Wolfgang Waltenberger. RAVE: A detector-independent toolkit to reconstruct vertices. *IEEE Trans. Nucl. Sci.*, 58:434–444, 2011.

[41] Jamie Nagle and Dennis Perepelitsa. sphenix five-year (2022-2026) running scenario and luminosity projections. 2017.

[42] Johannes Rauch and Tobias Schlter. GENFIT a Generic Track-Fitting Toolkit. *J. Phys. Conf. Ser.*, 608(1):012042, 2015.

[43] C. Patrignani et al. Review of Particle Physics. *Chin. Phys.*, C40(10):100001, 2016.

[44] CMS Collaboration. Transverse momentum balance of b-jet pairs in PbPb collisions at 5 TeV. 2016.

[45] R. Hambrock and W. A. Horowitz. Heavy flavour energy loss from ads/cft: A novel diffusion coefficient. *Eur. Phys. J. Web Conf.*, 171:18002, 2018.

[46] W. A. Horowitz. Fluctuating Heavy Quark Energy Loss in Strongly-Coupled Quark-Gluon Plasma. *Phys. Rev.*, D91:085019, 2015.

[47] ALPIDE development team ALICE ITS. ALPIDE Operations Manual. 2016.

[48] J. Anderson et al. FELIX: a PCIe based high-throughput approach for interfacing front-end and trigger electronics in the ATLAS Upgrade framework. *JINST*, 11(12):C12023, 2016.

[49] S. Adler et al. Phenix on-line systems. *Nucl. Instrum. Meth. A*, 499:560, 2003.